(memo)
~~Copy~~
629

[redacted] NASA TM X-162

NASA TM X-162

GPO PRICE $
CFSTI PRICE(S) $
Hard copy (HC) 3.00
Microfiche (MF) .75
ff 653 July 65

[redacted]

TECHNICAL MEMORANDUM
X-162

THE AERODYNAMIC CHARACTERISTICS OF SEVERAL THICK DELTA WINGS AT MACH NUMBERS TO 6 AND ANGLES OF ATTACK TO 50°

By John B. McDevitt and John V. Rakich

Ames Research Center
Moffett Field, Calif.

DECLASSIFIED- AUTHORITY
US: 1286 DROBKA TO LEBOW
MEMO DATED
6/8/66

Declassified by authority of NASA
Classification Change Notices No. 67
Dated ** 6/22/66

[redacted]

NATIONAL AERONAUTICS AND SPACE ADMINISTRATION
WASHINGTON March 1960

N66 33340
(ACCESSION NUMBER)
111
(PAGES)
(THRU)
1
(CODE)
01
(CATEGORY)
FACILITY FORM 602

[redacted]

DE[redacted]SIFIED

NATIONAL AERONAUTICS AND SPACE ADMINISTRATION

TECHNICAL MEMORANDUM X-162

THE AERODYNAMIC CHARACTERISTICS OF SEVERAL THICK DELTA WINGS AT MACH NUMBERS TO 6 AND ANGLES OF ATTACK TO 50°*

By John B. McDevitt and John V. Rakich

33340

SUMMARY

An experimental investigation of the aerodynamic characteristics of several thick delta wings has been made to provide basic information that may be useful in the design of vehicles employing high angles of attack to produce high lift and high drag during atmosphere entry.

The models tested consisted of a sharp elliptic cone, two blunt elliptic cones, and a flat-sided body having essentially diamond-shaped cross sections. The tests were conducted at Mach numbers from 0.6 to 6, angles of attack up to 50°, and angles of sideslip from -4° to $+4^{\circ}$. In addition to tests of the basic body shapes, various trailing-edge and tip controls were tested on two of the basic shapes.

Convenient relationships for use in the application of impact theory to arbitrary body shapes are presented and these relationships were used to estimate the aerodynamic characteristics of several of the models at hypersonic speeds. The estimated characteristics were found to compare favorably with experiment at a Mach number of 5.

The general problem of longitudinal stability and control of hypersonic gliders at high angles of attack is also discussed.

INTRODUCTION

The motion and heating of various types of atmosphere-entry vehicles have been studied in considerable detail in recent years (see, e.g., refs. 1 to 5). It has been shown that lift is of great advantage in reducing maximum heating rates, thus allowing for substantial radiation cooling, while high drag is useful for slowing down the vehicle at high

---

*Title, Unclassified

[redacted]

altitudes, thus tending to reduce the total heat load. At high speeds it is therefore desired to have high drag coupled with high lift, a condition which results in relatively low lift-drag ratios. If, however, adequate low-speed performance for maneuvering and landing is specified, then fairly large lift-drag ratios will be required at low speeds. In order to meet these contradictory requirements Eggers (ref. 5) suggested the use of the relatively slender configuration which achieves effective bluntness during re-entry by employing high angles of attack.

The present research study was initiated to provide, from experimental tests, basic information of a general nature which would be useful in the design of re-entry glide vehicles. The present report presents the experimental results obtained from tests at low speeds and at high speeds of a series of four thick delta-plan-form wings or bodies. A study of the aerodynamic characteristics of similar configurations at low angles of attack and supersonic speeds has been made by Jorgensen (ref. 6).

A259

Some information is also presented regarding the effectiveness of various control surfaces at high speeds, particularly with regard to trailing-edge controls. The use of Newtonian impact theory for estimating forces, moments, and lateral stability derivatives at hypersonic speeds is also discussed and comparisons between estimated and experimental values are presented. Convenient relationships for use in the application of impact theory to arbitrary body shapes are presented, and the general problem of longitudinal stability and control of hypersonic gliders at large angles of attack is discussed.

NOTATION

The primary symbols used in the main body of this report are defined as follows (see also figs. 1 and 2):

a	thickness of model at base
A	aspect ratio
A_b	base area
b	width of model at base (span)
C_A	axial-force coefficient (includes base drag), $\frac{\text{axial force}}{q_\infty S}$
C_D	drag coefficient (includes base drag), $\frac{\text{drag}}{q_\infty S}$

A259

C_l	rolling-moment coefficient, $\frac{\text{rolling moment}}{q_\infty Sb}$
C_L	lift coefficient, $\frac{\text{lift}}{q_\infty S}$
C_m	pitching-moment coefficient, $\frac{\text{pitching moment}}{q_\infty S l_1}$
C_n	yawing-moment coefficient, $\frac{\text{yawing moment}}{q_\infty Sb}$
C_N	normal-force coefficient, $\frac{\text{normal force}}{q_\infty S}$
C_p	pressure coefficient
C_Y	side-force coefficient, $\frac{\text{side force}}{q_\infty S}$
l_1	body length
l_2	body length before blunting (see figs. 1 and 2)
$\frac{L}{D}$	lift-drag ratio, $\frac{C_L}{C_D}$
M_∞	free-stream Mach number
q_∞	free-stream dynamic pressure
s	surface area
S	plan-form area
x,y,z	Cartesian coordinate system (see fig. 1)
X_N	center of pressure in pitch (eq. (1))
X_Y	center of pressure in sideslip (eq. (2))
α	angle of attack, deg
β	angle of sideslip, deg
δ	trailing-edge control deflection angle (positive when deflected downward, fig. 5(a)), deg
θ	angle of rotation for tip controls (fig. 5(b)), deg

λ	ratio of major to minor axes of elliptic cross sections
$C_{L_\alpha}, C_{m_\alpha}$	derivatives with respect to angle of attack α, per deg (except where noted)
$C_{l_\beta}, C_{n_\beta}, C_{Y_\beta}$	derivatives with respect to sideslip angle β, evaluated at $\beta = 0$, per deg (except where noted)

Subscripts

b	body base
c	control

APPARATUS AND MODELS

Wind Tunnels and Equipment

The tests were conducted in the Ames 2- by 2-foot transonic wind tunnel at Mach numbers from 0.6 to 1.3, and in the Ames 10- by 14-inch supersonic wind tunnel at Mach numbers from 3 to 6. Detailed descriptions of these facilities are presented in references 7 and 8. The aerodynamic forces and moments were measured with a six-component strain-gage balance incorporated in the model support system. A strain-gage pressure cell, connected to a static-pressure orifice within the balance, was used to measure base pressures for each model and, in the case of one of the models, a strain-gage pressure cell was used to measure the static pressure on the upper surface of the model.

Models

Basic body shapes.- Sketches of the four basic models and the pertinent geometric properties of each model are presented in figure 2. The cross sections for models 1, 2, and 3 are elliptical in all planes normal to the longitudinal reference axes. Model 1 is a sharp elliptic cone for which the ratio of major to minor axes (designated by λ) of the elliptic cross sections is equal to 2.

Models 2 and 3 will be referred to as "blunt elliptic cones." The ratio of major to minor axes of the elliptic cross sections for these models is equal to 2 and 3, respectively. In each case the blunt nose sections were obtained by modifying the forward half of sharp elliptic cones. The parabolic nose sections in plan and side views are tangent to the straight-line afterportions at the midpoint of the body length before modification.

Model 4 is essentially a flat-sided, symmetrical body, modified to have rounded leading edges and incorporating a small hemispherical nose section. The cross section shapes vary from circular at the base of the nose section to diamond at the base.

Each model was constructed in two sizes (see tabulated values in fig. 2). The large versions were used for tests at angles of attack up to approximately 20°, and the smaller models were used for angles of attack greater than 20°. The small models were mounted on the balance-sting combination so that the models were at an angle of attack relative to the balance. This type of mounting necessitated, for some cases, the addition of a small protuberance on the aft upper surface of the model (see photographs of fig. 3). In order to evaluate the effects of the protrusions, upper surface pressure coefficients were measured near the aft end of the small version of model 2 (see fig. 2(b)). The results are presented in figure 4 together with curves showing the measured base-pressure coefficient and empirical base-pressure coefficient $-1/M_\infty^2$. It is evident that, for large angles of attack, the upper surface pressures are not only small but actually, in some cases, less than those measured at the model base. Thus, it is believed that the protrusions did not appreciably affect the measured forces and moments at the large angles of attack (greater than about 30°) and high Mach numbers (greater than 3) for which these models were used.

Boundary-layer trips, formed by cementing carborundum grits to the nose portion of each model, were used in the tests at Mach numbers from 0.6 to 1.3 in order to ensure a turbulent boundary layer. No attempt was made to fix transition for the tests at high speeds.

Controls.- A series of three small, flat trailing-edge controls were used in conjunction with model 2 (fig. 5(a)) and two similar controls were used with model 4 (fig. 5(b)). The controls were attached along the lower edge of the base of the models. The control deflection angle, δ, is defined to be zero when the controls are normal to the body base and positive when deflected downward into the air stream.

Two rotatable tip controls (rotavons), mounted at the tips of model 4 as shown in figure 5(b), were also tested. The axes of rotation for the controls run parallel to the body leading edges and the angle of rotation is designated by θ (positive when the control is rotated upward).

An additional study involved the use of an upper surface vertical stabilizer (dorsal fin) mounted on model 4 as shown in figure 5(c). This fixed, vertical stabilizer was tested in order to provide some information at high speeds regarding the effectiveness of upper surface stabilizers in the shadow of the body at angle of attack.

TESTS AND PROCEDURE

Range of Test Variables

The tests at high speeds were conducted at free-stream Mach numbers of 3 through 6, and at angles of attack up to 50°. The tests at low speeds were conducted at Mach numbers of 0.6 through 1.3, and at angles of attack up to 20°. The directional and lateral stability data were obtained by testing through a range of sideslip angles from -4° to +4° at several angles of attack for each of the test Mach numbers from 0.6 to 6. The wind-tunnel test conditions and the corresponding Reynolds numbers per foot are tabulated below:

Mach number, M_∞	Total pressure, psia	Total temperature, °F	Reynolds number, ft^{-1}
0.6	11.2	70	2.7×10^6
.9	8.9	70	2.7×10^6
1.0	8.6	70	2.7×10^6
1.1	8.5	70	2.7×10^6
1.3	8.4	70	2.7×10^6
3.0	15 to 30[a]	50	2.6 to 5.1×10^6
4.0	85	50	8.9×10^6
5.0	87	200	3.8×10^6
6.0	87	350	1.9×10^6

[a] Total pressure was reduced at large angles of attack (above 20°) so as not to exceed balance load limitations.

Reduction of Data

The force and moment data were reduced to standard coefficient form. The lift and drag coefficients are referred to the wind axes while the remaining coefficients are referred to body axes as shown in figure 1. A common moment reference center with regard to the reference length l_2 was chosen as indicated in figure 1.

The experimental data presented in this report include the effects of base pressure. Interference effects between model and model support system are known to be negligibly small at high speeds. At low speeds the interference effects are believed to be small since the ratio of support sting area to model base area is small.

The directional and lateral data were plotted relative to sideslip angle, β, and the derivatives C_{Y_β}, C_{n_β}, and C_{l_β} were evaluated from the plots. Because the test results were essentially linear within the ±4° range of sideslip angles, only the derivatives are presented and discussed herein.

Accuracy of Test Results

The accuracy of the test results was influenced by uncertainties in the measurements of forces and moments and in the determination of stream static and dynamic pressures and angles of attack and sideslip. These uncertainties resulted in estimated maximum errors in the test results as shown in the following table:

A
2
5
9

Tests	Force coefficients	Pitching-moment coefficients	Lateral stability derivatives		
			C_{Y_β}/deg	C_{n_β}/deg	C_{l_β}/deg
Low speed	±0.01	±0.005	±0.0002	±0.0002	±0.0001
High speed	±.02	±.01	±.0005	±.0005	±.0002

It should be noted that, for the most part, the test results presented herein are in error by less than these estimates.

RESULTS AND DISCUSSION

The experimental results obtained from low-speed tests of the four basic body shapes are presented first and are followed by the results obtained at high speeds. Next, a comparison of models and a discussion of Mach number effects are presented; and finally, the results of the rather limited control surface study at high speeds are presented.

Low-Speed Characteristics

The experimental results at low speeds, obtained from tests of the four basic body shapes at Mach numbers from 0.6 to 1.3, are presented in figures 6 to 9. Representative values of the measured base-pressure coefficients are tabulated in table I and representative values of the measured centers of pressure in pitch and sideslip are tabulated in table II. The centers of pressure in pitch and sideslip (normalized with respect to length l_2, see figs. 1 and 2) are defined as follows:

$$\frac{X_N}{l_2} = 0.6 - \frac{l_1}{l_2}\frac{C_m}{C_N} \tag{1}$$

$$\frac{X_Y}{l_2} = 0.6 - \frac{b}{l_2}\frac{C_{n_\beta}}{C_{Y_\beta}} \tag{2}$$

High-Speed Characteristics

The experimental results obtained at Mach numbers from 3 to 6 for the four basic body shapes are presented in figures 10 through 13. (At large angles of attack, data were obtained only for Mach numbers of 3 and 5.) Representative values of the measured base-pressure coefficient and the base axial-force coefficient are presented in table III. Also presented in this table are estimated values for the axial-force coefficient. These values were based on the assumption that the pressure coefficient was equal to $-1/M_\infty^2$.

In figures 10 through 13 the experimental results for a Mach number of 5 are compared with estimated values obtained by application of Newtonian impact theory together with an estimated skin-friction drag coefficient of 0.008 and an estimated base drag coefficient equivalent to a base-pressure coefficient of $-1/M_\infty^2$. In the simple impact theory, as used here (see appendix A), the pressure coefficient on all forward-facing surfaces is assumed to vary as

$$C_p = 2 \sin^2\delta \tag{3}$$

where δ is the local angle of inclination of the surface relative to the wind.

Mach Number Effects and Comparison of Models

Various cross plots of the data, illustrating, in particular, Mach number effects, are presented in figures 14 through 16.

A comparison of the zero-lift drag coefficients and the corresponding base-drag coefficients is presented in figure 14 and a direct comparison of the zero-lift drag coefficients for the various models is presented in figure 15(a). The increase in drag which occurs as the Mach number is increased from 5 to 6 is not fully understood. The increase in skin-friction drag (the test Reynolds number per foot decreases from 3.8×10^6 to 1.9×10^6) accounts for less than 50 percent of this increase.

At hypersonic speeds (Mach numbers greater than about 6) the base drag is negligible. At low speeds, however, the base drag constitutes the major portion of the drag. It is interesting to note that all four bodies had nearly the same value of base-pressure coefficient at any given Mach number (see tables I and III).

The lift-curve slope, measured at $\alpha = 0$, is presented in figure 15(b). The Mach number effect is small and all four models have close to the same values of lift-curve slope except at near-sonic Mach numbers. It is instructive to compare the present results with the theoretical result of R. T. Jones (ref. 9)

A259

$$\frac{dC_L}{d\alpha} = \frac{\pi}{2} A \text{ , per radian}$$

which is applicable at subsonic and supersonic speeds for slender wings of very low aspect ratio and for wings of moderate aspect ratio at near-sonic speeds. In the present case models 1 and 4 have aspect ratios (based on plan-form area) of approximately 1.07, while models 2 and 3 have aspect ratios of approximately 1.17. The measured values of lift-curve slopes are not too different from the idealized values, a result which is somewhat surprising since the streamwise shapes of these configurations bear little resemblance to conventional airfoil profiles.

The variations of maximum lift-drag ratios with Mach number are presented in figure 15(c). (Values are not presented for model 1 at low speeds since the maximum lift-drag ratios for this model were not reached in the tests.) As could be expected, the maximum lift-drag ratios for the various configurations vary inversely with the ratio of base area to plan-form area throughout the speed range since this ratio is a qualitative measure of the over-all slenderness and, hence, is indicative of the wave drag to be expected as well as the base drag. The low aerodynamic efficiency at subsonic speeds is, of course, the direct consequence of the extremely large base drags.

The variations of the lateral stability derivatives with Mach number for several angles of attack are presented in figure 16. The decrease in C_{n_β} as the Mach number is decreased is the result of a forward travel in the location of the center of pressure in sideslip (see tables II and IV) and a decrease in side-force derivative C_{Y_β}. The quantity C_{l_β} was found to be considerably more negative at low speeds than at supersonic speeds.

Control Studies

Various horizontal and vertical control surfaces were tested in conjunction with models 2 and 4 at Mach numbers of 3 and 5.

Trailing-edge controls.- A series of three small, flat, trailing-edge controls were tested in conjunction with model 2. The controls were attached along the lower periphery of the model base as shown in figure 5(a). The control deflection angle, δ, is defined to be zero when the controls are normal to the body base and positive when deflected downward (into the air stream). The ratio of control-surface area to model plan-form area was arbitrarily chosen as 0.25.

The measured pitching-moment coefficients for various trailing-edge control deflection angles are presented in figure 17. The incremental changes in pitching-moment and normal-force coefficients due to the presence of the controls are presented in figure 18. The agreement between experiment and values estimated from impact theory (assuming zero pressure coefficient on the upper surfaces of the controls) is reasonably good only when the local angles of attack of the controls are large. A somewhat better agreement is obtained if the pressure coefficient on the upper surface of the controls is assumed to be equal to $-1/M_\infty^2$.

A set of two similar trailing-edge controls was tested with model 4 (see fig. 5(b)). The incremental changes in pitching-moment and normal-force coefficients for this configuration are presented in figure 19.

It should be pointed out here that trailing-edge controls when used with hypersonic vehicles at moderate to large angles of attack can be deflected to create negative increments of pitching moment but significant positive increments are not possible since the upper surfaces of the controls are shielded from the flow and therefore are relatively ineffective. A discussion of the general problem of longitudinal stability and control of hypersonic glide vehicles will be deferred to a later section of this report (appendix B).

Tip controls.- The rotatable tip controls, mounted on model 4 as shown in figure 5(b), were tested in the vertical ($\theta = 90^\circ$) and horizontal ($\theta = 0^\circ$) positions. The measured lateral stability derivatives are presented in figure 20. (The body-alone results presented in fig. 20 were obtained by fairing lines through the data of fig. 13(g).) Also presented are estimated values obtained by adding to the experimental data for the basic body the calculated results derived by impact theory for the controls alone. Large increases in C_{n_β} due to the presence of the controls were obtained for both the horizontal and vertical position of these controls. In the horizontal position this increase is due to changes with β of the rather large drag forces acting at the blunt leading edges of the controls.

These controls at angles of rotation of 0° and 90° contribute little to C_{l_β}. Theoretical results for controls alone are presented in figure 21 and indicate that large contributions of C_{l_β} could be expected at values of θ between 0° and 90°.

Upper surface vertical stabilizer.- The dorsal fin shown in figure 5(c) was tested with model 4 in order to provide some information regarding the manner in which the body shields the region near the upper surface and thus alters the effectiveness of upper surface stabilizers. The lateral stability derivatives, measured at Mach numbers of 3 and 5 and angles of attack of 0° and 14°, are presented in figure 22 and compared with the results for the basic body shape (model 4 without dorsal fin). The experimental data obtained at an angle of attack of 14° indicate that this vertical surface retains a considerable amount of effectiveness at a Mach number of 3, but virtually all of the effectiveness is lost as the Mach number is increased to 5. This result indicates that control surfaces can be considered to be ineffective for Mach numbers greater than about 5 if located in the shadow of the body (i.e., shielded from the oncoming flow).

A
2
5
9

CONCLUDING REMARKS

The measured aerodynamic characteristics for a series of four simple body shapes have been presented together with the results of a rather limited control surface study. Reasonably good agreement between experiment and values estimated from simple impact theory was obtained at a Mach number of 5.

The aerodynamic performance at transonic and subsonic speeds deteriorates as a result of the very large base-drag effects associated with vehicles of the type considered here (vehicles having relatively large ratios of base area to plan-form area). It is probable, however, that much could be done to alleviate the base-area effect at low speeds. For instance, the shape of the upper surface is relatively unimportant at high angles of attack and hypersonic speeds, and consequently the upper surface could well be designed from low-speed considerations, particularly with regard to reducing base-drag effects. It also appears desirable from trim and static-stability considerations to shape the lower surface by means of a certain amount of longitudinal curvature (see discussion in appendix B), a process which also could be used to advantage in reducing the base area.

Ames Research Center
National Aeronautics and Space Administration
Moffett Field, Calif., Nov. 5, 1959

[redacted]

APPENDIX A

CONVENIENT RELATIONSHIPS FOR USE IN THE APPLICATION OF IMPACT THEORY

It is well known, of course, that Newtonian impact theory has wide application at hypersonic speeds for estimating forces on three-dimensional shapes. In the present report reasonably good agreement between theoretical and experimental results was obtained, not only with regard to forces but also with regard to various stability derivatives. Since impact theory is extremely attractive because of its simplicity and since the impact theory has wide application, at least for qualitative estimates of aerodynamic properties of simple body shapes at hypervelocities, it appears worthwhile to present here various convenient relationships for use in applications of the theory.

A
2
5
9

The suggested refinements of impact theory, in particular, inclusion of centrifugal forces (see, e.g., ref. 10), are not considered here. A detailed discussion of hypersonic flows and various hypersonic approximations may be found in references 10 and 11.

General Relationships for Arbitrary Bodies

Consider a body having a coordinate system as shown in sketch (a). The free-stream velocity vector is oriented so that the body is at relative angles of attack,[1] α, and of sideslip, β. It is convenient to represent the free-stream velocity and the unit, outer normal at the body surface by the vector quantities

$$\overline{V}_\infty = V_\infty(\overline{i} \cos \alpha \cos \beta - \overline{j} \sin \beta + \overline{k} \sin \alpha \cos \beta) \tag{A1}$$

$$\overline{n} = \overline{i} \cos(nx) + \overline{j} \cos(ny) + \overline{k} \cos(nz) \tag{A2}$$

where $\overline{i}, \overline{j}, \overline{k}$ are unit vectors directed along the x, y, z axes and $\cos(nx)$, $\cos(ny)$, $\cos(nz)$ are direction cosines (components of the unit outer normal in the x, y, z directions).

The pressure coefficient at the body surface is given by

---

[1] In this section of the report the quantities α and β are expressed in radians.

[redacted]

A
2
5
9

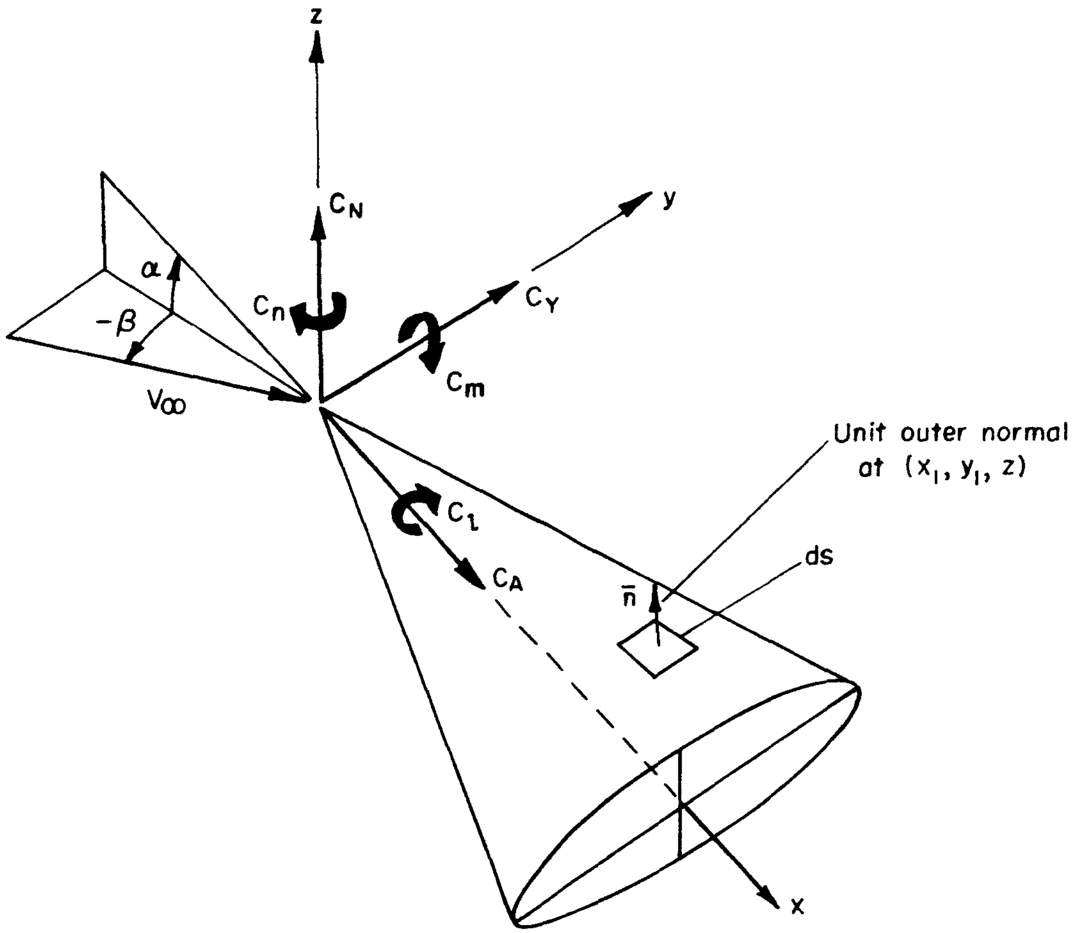

Sketch (a)

$$C_p = 2\,\frac{(\bar{V}_\infty \cdot \bar{n})^2}{V_\infty{}^2}$$

$$= 2[\cos^2(nx)\cos^2\alpha\ \cos^2\beta + \cos^2(ny)\sin^2\beta + \cos^2(nz)\sin^2\alpha\ \cos^2\beta$$
$$-2\cos(nx)\cos(ny)\cos\alpha\ \cos\beta\ \sin\beta - 2\cos(ny)\cos(nz)\sin\alpha\ \sin\beta\ \cos\beta$$
$$+2\cos(nx)\cos(nz)\cos\alpha\ \sin\alpha\ \cos^2\beta] \qquad \text{(A3)}$$

The particular quantities useful for our purposes are as follows:

$$(C_p)_{\beta=0} = 2[\cos^2(nx)\cos^2\alpha + \cos^2(nz)\sin^2\alpha + 2\cos(nx)\cos(nz)\cos\alpha\ \sin\alpha] \qquad \text{(A4)}$$

[redacted]

$$\left(\frac{\partial C_p}{\partial \beta}\right)_{\beta=0} = -4[\cos(nx)\cos(ny)\cos\alpha + \cos(ny)\cos(nz)\sin\alpha] \qquad (A5)$$

The pressure coefficient and derivative (eqs. (A4) and (A5)) are assumed to be zero at all body surfaces shielded from the flow. See sketch (b).

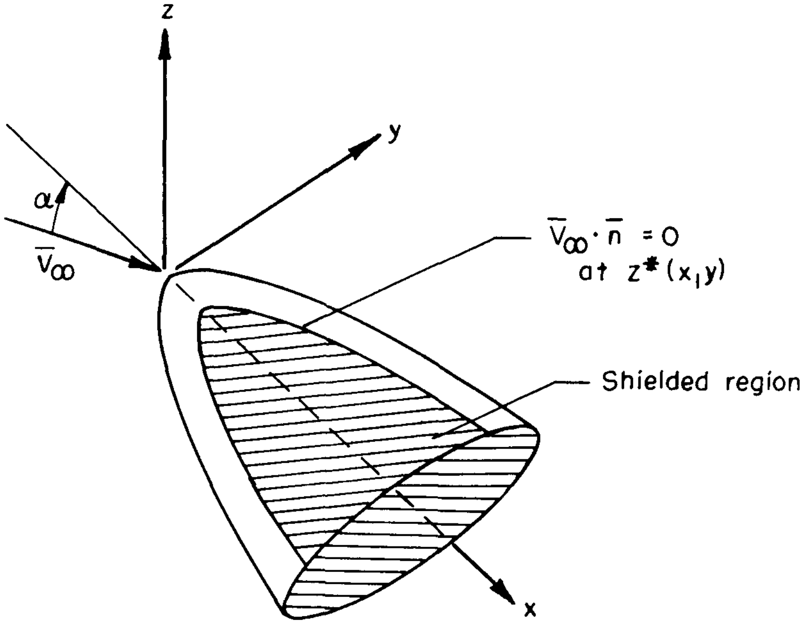

Sketch (b)

Force coefficients.- The force vector resulting from flow impact on the surface element ds is

$$\overline{F} = -\rho_\infty(\overline{V}_\infty \cdot \overline{n})^2 \overline{n}\, ds$$

and the force coefficients are defined as

$$C_A = -\iint C_p \cos(nx) \frac{ds}{A} \qquad (A6)$$

$$C_Y = -\iint C_p \cos(ny) \frac{ds}{A} \qquad (A7)$$

$$C_N = -\iint C_p \cos(nz) \frac{ds}{A} \qquad (A8)$$

[redacted]

where the pressure coefficient is given by equation (A4), A is the reference area, and the shielded region (see sketch (b)) is to be excluded from the surface integration. When flat surfaces are involved, the direction consines are easily obtained if the unit normal is resolved into components parallel to the x, y, z axes. If the body shape can be expressed analytically in the form $Z = Z(x,y)$, it is convenient to relate the surface element of area to the projected area in the x, y plane,

$$ds = \frac{dx\ dy}{|\cos(nz)|}$$

A
2
5
9

with the integrations performed along positive directions. In this case the direction cosines for the upper surface are defined as

$$\cos(nx),\cos(ny),\cos(nz) = \frac{(-\partial Z/\partial x),(-\partial Z/\partial y),1}{\sqrt{1+(\partial Z/\partial x)^2+(\partial Z/\partial y)^2}} \tag{A9}$$

and for the lower surfaces the signs are reversed,

$$\cos(nx),\cos(ny),\cos(nz) = \frac{(\partial Z/\partial x),(\partial Z/\partial y),-1}{\sqrt{1+(\partial Z/\partial x)^2+(\partial Z/\partial y)^2}} \tag{A10}$$

Moment coefficients and lateral stability derivatives.- If the moment reference center is taken at the origin (0,0,0), the moment coefficients (see sketch (a)) are given by

$$C_l = \frac{1}{bA}\iint[y\cos(nz) - Z\cos(ny)]C_p ds \tag{A11}$$

$$C_m = \frac{1}{cA}\iint[Z\cos(nx) - x\cos(nz)]C_p ds \tag{A12}$$

$$C_n = \frac{1}{bA}\iint[x\cos(ny) - y\cos(nx)]C_p ds \tag{A13}$$

The various lateral stability derivatives of interest here are as follows,

$$C_{Y_\beta} = -\frac{1}{A}\iint C_{p_\beta}\cos(ny)ds \tag{A14}$$

$$C_{l_\beta} = \frac{1}{bA}\iint C_{p_\beta}[y\ \cos(nz) - Z\ \cos(ny)]ds \qquad \text{(A15)}$$

$$C_{n_\beta} = \frac{1}{bA}\iint C_{p_\beta}[x\ \cos(ny) - y\ \cos(nx)]ds \qquad \text{(A16)}$$

where the subscript β denotes differentiation with respect to β. In the above equations $Z(x,y)$ represents the body shape, A is a reference area, b and c are reference lengths, and the region of surface integration excludes the shielded portion.

Smooth Bodies Possessing Lateral Symmetry, $\beta = 0$

In the case of smooth bodies possessing lateral symmetry at $\beta = 0$, it is sufficient to consider only the right-hand portion of the body (positive y). It is also convenient to use a coordinate system (ξ,η,ζ) where the distances have been normalized by dividing by the body length l. The body shape is assumed to be given by the expressions (positive η only)

$$Z_U = Z_U(\xi,\eta)$$

$$Z_L = Z_L(\xi,\eta)$$

where the subscripts U and L are used to designate upper and lower surface quantities, respectively.

The axial- and normal-force coefficients are given by

$$C_A = \frac{2}{K_1}\left[\int_0^1\left(\int_{\eta^*}^{\eta_s} C_{p_U}\frac{\partial Z_U}{\partial\xi}\,d\eta - \int_0^{\eta_s} C_{p_L}\frac{\partial Z_L}{\partial\xi}\,d\eta\right)d\xi\right] \qquad \text{(A17)}$$

$$C_N = \frac{2}{K_1}\left[\int_0^1\left(\int_0^{\eta_s} C_{p_L}d\eta - \int_{\eta^*}^{\eta_s} C_{p_U}d\eta\right)d\xi\right] \qquad \text{(A18)}$$

where K_1 is the ratio of reference area (plan-form area, for instance) to body length squared,

$$K_1 = \frac{A}{l^2} \qquad \text{(A19)}$$

The upper surface lateral integration extends from $\eta^*(\xi)$, which is obtained from solution of

$$\frac{\partial Z_U}{\partial \xi} = \tan \alpha \tag{A20}$$

to the lateral extremity of the plan form, $\eta_s(\xi)$.

The pitching-moment coefficient for the moment reference center at (0,0,0) and based on reference length l is given by

A259

$$C_m = \frac{2}{K_1}\left\{\int_0^1\left[\int_{\eta^*}^{\eta_s} C_{p_U}\left(Z_U\frac{\partial Z_U}{\partial \xi} + \xi\right)d\eta - \int_0^{\eta_s} C_{p_L}\left(Z_L\frac{\partial Z_L}{\partial \xi} + \xi\right)d\eta\right]d\xi\right\} \tag{A21}$$

and the lateral stability derivatives (evaluated at $\beta = 0$) are given by

$$C_{Y_\beta} = -\frac{2}{K_1}\left\{\int_0^1\left[\int_0^{\eta_s}\left(C_{p_\beta}\right)_L\frac{\partial Z_L}{\partial \eta}\,d\eta - \int_{\eta^*}^{\eta_s}\left(C_{p_\beta}\right)_U\frac{\partial Z_U}{\partial \eta}\,d\eta\right]d\xi\right\} \tag{A22}$$

$$\begin{aligned} C_{l_\beta} = -\frac{2}{K_1K_2}\Bigg\{\int_0^1\Bigg[&\int_0^{\eta_s}\left(C_{p_\beta}\right)_L\left(\eta + Z_L\frac{\partial Z_L}{\partial \eta}\right)d\eta \\ &- \int_{\eta^*}^{\eta_s}\left(C_{p_\beta}\right)_U\left(\eta + Z_U\frac{\partial Z_U}{\partial \eta}\right)d\eta\Bigg]d\xi\Bigg\} \end{aligned} \tag{A23}$$

$$\begin{aligned} C_{n_\beta} = -\frac{2}{K_1K_2}\Bigg\{\int_0^1\Bigg[&\int_{\eta^*}^{\eta_s}\left(C_{p_\beta}\right)_U\left(\xi\frac{\partial Z_U}{\partial \eta} - \eta\frac{\partial Z_U}{\partial \xi}\right)d\eta \\ &+ \int_0^{\eta_s}\left(C_{p_\beta}\right)_L\left(\eta\frac{\partial Z_L}{\partial \xi} - \xi\frac{\partial Z_L}{\partial \eta}\right)d\eta\Bigg]d\xi\Bigg\} \end{aligned} \tag{A24}$$

where K_1 is defined by equation (A19) and K_2 by

$$K_2 = \frac{b}{l}$$

where the reference length b is usually taken as the span of the configuration.

In the above equations C_p and C_{p_β} are to be obtained by use of equations (A4) and (A5), and the direction cosines, from equations (A9) and (A10).

Elliptic Cones

As an example of the use of the foregoing equations and of their use in the present report, the general relationships have been used to obtain the impact forces and moments acting on a family of elliptic cones (sketch (c)). The surface ordinates are, for convenience, expressed as follows:

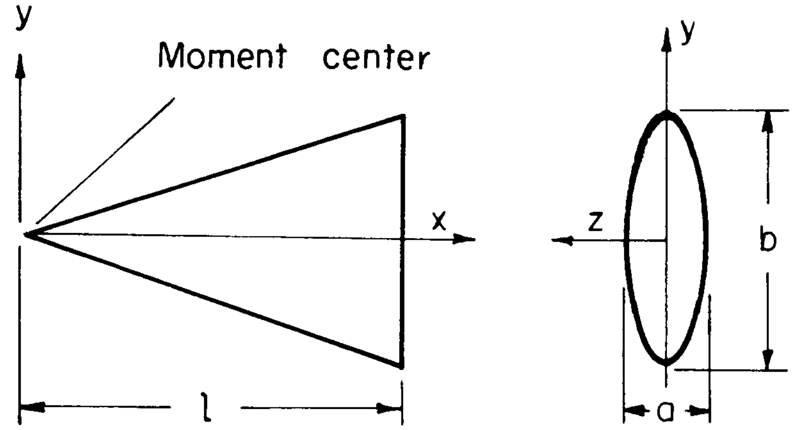

A
2
5
9

$$\lambda = \frac{b}{a}, \quad \mu = \frac{b/2}{l}$$

Sketch (c)

$$Z = \pm \frac{\mu x}{\lambda}\sqrt{1 - s^2}, \quad s = \frac{y}{\mu x}$$

When $\tan \alpha > \mu/\lambda$, the upper surface is shielded in the region

$$0 \leqq s \leqq \sqrt{1 - \frac{\mu^2}{\lambda^2 \tan^2 \alpha}}$$

The force, moment, and lateral stability derivatives (defined in the same manner as in the Notation section of this report, except that the moment reference center is taken at the apex rather than at $0.6\, l_2$ and β is measured in radians) are as follows:

$$C_A = \frac{2\mu\lambda}{\lambda^2 - 1}\left(f_1 \frac{\mu^2}{\lambda^2 k\sqrt{k^2 - 1}} \cos^2\alpha + f_2 \frac{2\mu}{\lambda} \sin\alpha \cos\alpha + f_3 \sin^2\alpha\right)$$

$$C_N = \frac{2\lambda^2}{\lambda^2 - 1}\left(f_2 \frac{\mu^2}{\lambda^2} \cos^2\alpha + f_3 \frac{2\mu}{\lambda} \sin\alpha \cos\alpha + f_4 \sin^2\alpha\right)$$

$$C_m = -\frac{2}{3}\left[1 + \left(\frac{\mu}{\lambda}\right)^2\right] C_N$$

A
2
5
9

$$C_{Y_\beta} = -\frac{4}{\lambda^2 - 1}\left(f_5 \frac{\mu}{\lambda} \cos\alpha + f_6 \sin\alpha\right)$$

$$C_{n_\beta} = -\frac{2}{3}\left(\frac{1 + \mu^2}{2\mu}\right) C_{Y_\beta}$$

$$C_{l_\beta} = -\frac{4}{3\lambda}\left(f_6 \frac{\mu}{\lambda} \cos\alpha + f_7 \sin\alpha\right)$$

where

$$f_1 = \pi - \tan^{-1}\left(\frac{s^*}{\sqrt{1 - s^{*2}}} \sqrt{\frac{k^2 - 1}{k^2}}\right)$$

$$f_2 = \frac{1}{k} \tanh^{-1} \frac{s^*}{k}$$

$$f_3 = \pi\left(1 - \sqrt{\frac{k^2 - 1}{k^2}}\right) + \sqrt{\frac{k^2 - 1}{k^2}} \tan^{-1}\left(\frac{s^*}{\sqrt{1 - s^{*2}}} \sqrt{\frac{k^2 - 1}{k^2}}\right) - \sin^{-1} s^*$$

$$f_4 = s^* - \frac{1 - k^2}{k} \tanh^{-1} \frac{s^*}{k}$$

$$f_5 = \pi\left(\sqrt{\frac{k^2}{k^2 - 1}} - 1\right) - \sqrt{\frac{k^2}{k^2 - 1}} \tan^{-1}\left(\frac{s^*}{\sqrt{1 - s^{*2}}} \sqrt{\frac{k^2 - 1}{k^2}}\right) + \sin^{-1} s^*$$

$$f_6 = k \tanh^{-1} \frac{s^*}{k} - s^*$$

$$f_7 = \frac{2k^2 - 1}{2}\left(\pi - \sin^{-1} s^*\right) + \frac{s^*}{2}\sqrt{1 - s^{*2}} - k\sqrt{k^2 - 1}\left[\pi - \tan^{-1}\left(\frac{s^*}{\sqrt{1 - s^{*2}}} \sqrt{\frac{k^2 - 1}{k^2}}\right)\right]$$

[redacted]

and

$$k^2 = \frac{\lambda^2 + \mu^2}{\lambda^2 - 1}$$

$$s^* = 0 \qquad \text{for} \quad \tan\alpha < \frac{\mu}{\lambda}$$

$$s^* = \sqrt{1 - \frac{\mu^2}{\lambda^2 \tan^2\alpha}} \qquad \text{for} \quad \tan\alpha > \frac{\mu}{\lambda}$$

The above equations for force and moment coefficients cannot be applied directly for cones ($\lambda = 1$). Letting $\lambda \rightarrow 1$ results in the following:

A259

$$C_A = \frac{\mu}{1 + \mu^2}\left(2\mu^2 g_1 \cos^2\alpha + 4\mu g_2 \sin\alpha \cos\alpha + g_3 \sin^2\alpha\right)$$

$$C_N = \frac{2}{1 + \mu^2}\left(\mu^2 g_2 \cos^2\alpha + \mu g_3 \sin\alpha \cos\alpha + g_4 \sin^2\alpha\right)$$

$$C_m = -\frac{2}{3}(1 + \mu^2)C_N$$

$$C_{Y_\beta} = -\frac{4}{3(1 + \mu^2)}\left(\frac{3}{2}\mu g_5 \cos\alpha + g_6 \sin\alpha\right)$$

$$C_{n_\beta} = -\frac{2}{3}(1 + \mu^2)\frac{C_{Y_\beta}}{2\mu}$$

$$C_{l_\beta} = 0$$

where

$$g_1 = \pi - \sin^{-1}s^*$$

$$g_2 = s^*$$

$$g_3 = \pi - s^*\sqrt{1 - s^{*2}} - \sin^{-1}s^*$$

$$g_4 = s^*\left(1 - \frac{1}{3}s^{*2}\right)$$

$$g_5 = \pi + s^* \sqrt{1 - s^{*2}} - \sin^{-1} s^*$$

$$g_6 = s^{*3}$$

and

$$s^* = 0 \quad \text{for} \quad \tan\alpha < \mu$$

$$s^* = \sqrt{1 - \frac{\mu^2}{\tan^2\alpha}} \quad \text{for} \quad \tan\alpha > \mu$$

A 2 5 9

It should be mentioned that the undersurface forces and moments for cones or elliptic cones can be obtained by simply setting $s^* = 1$ in the above results.

Various calculated results are presented in figure 23. (The effects of skin friction and base pressure on axial force have not been considered here.)

[redacted]

APPENDIX B

SOME REMARKS ON THE LONGITUDINAL STABILITY AND CONTROL OF HYPERSONIC GLIDE VEHICLES AT HIGH ANGLES OF ATTACK

Consider a hypersonic glide vehicle operating at sufficiently high angles of attack that the upper surface is completely shielded from the flow (sketch (d)). The vehicle is assumed to consist of a body (such as a thick, blunt delta wing) and a trailing-edge flap. If Newtonian impact theory is assumed to hold, the forces acting on the body and the flap may be considered separately, as indicated in sketch (d) where subscripts 1 refer to the main body and subscripts 2 refer to the trailing-edge control. The normal forces acting at the lower surfaces are represented by $C_{N_1}S_1q_\infty$ and $C_{N_2}S_2q_\infty$ where C_{N_1} and C_{N_2} are normal-force coefficients based on projected (plan form) areas S_1 and S_2, respectively.

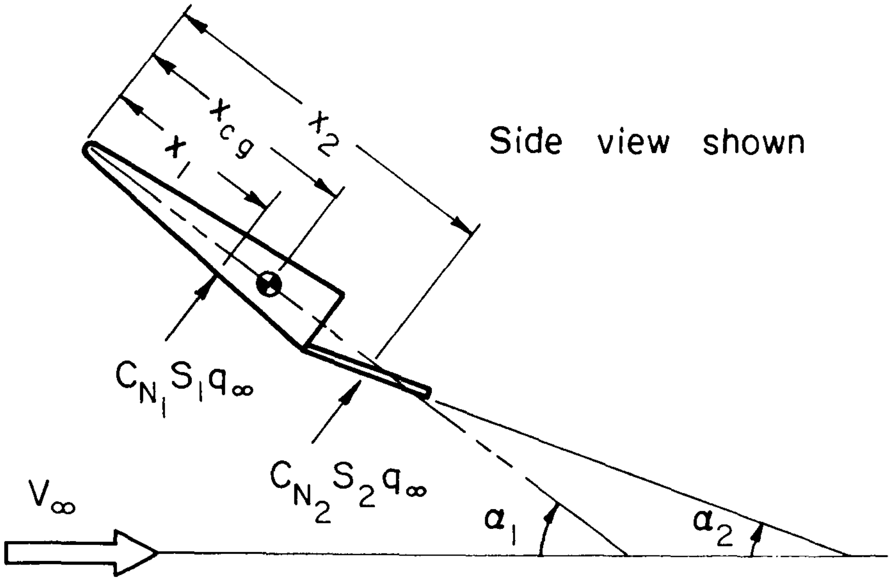

Sketch (d)

If it is assumed that the local angles of attack α_1 and α_2 are perturbed by the amount ϵ, the rate of change of pitching moment about the center-of-gravity location x_{cg} is given by

[redacted]

$$\frac{S}{S_1}\,\frac{\partial C_{m_{cg}}}{\partial \epsilon} \approx \frac{\partial C_{N_1}}{\partial \epsilon}\left(\frac{x_{cg} - x_1}{l}\right) - \frac{\partial C_{N_2}}{\partial \epsilon}\left(\frac{x_2 - x_{cg}}{l}\right)\frac{S_2}{S_1}$$

where quantities of the order $\partial x_1/\partial\alpha$, $\partial x_2/\partial\alpha$ are assumed to be negligible and C_{N_1}, C_{N_2} are functions of $\alpha_1 + \epsilon$ and $\alpha_2 + \epsilon$, respectively. The pitching-moment coefficient $C_{m_{cg}}$ is defined as the moment at x_{cg} normalized with respect to $q_\infty S l$ where S is a reference area and l a reference length. It is convenient to consider the above relationship as $\epsilon \to 0$ and, for simplicity of notation, define $(\partial C_{m_{cg}}/\partial\epsilon)_{\epsilon \to 0}$ as simply $\partial C_{m_{cg}}/\partial\alpha$. Then, the trim and the static longitudinal stability requirements involve the simultaneous consideration of the following two equations,

A
2
5
9

$$C_{N_1}\left(\frac{x_{cg} - x_1}{l}\right) = C_{N_2}\left(\frac{x_2 - x_{cg}}{l}\right)\frac{S_2}{S_1} \qquad \text{(B1)}$$

$$\frac{\partial C_{m_{cg}}}{\partial\alpha} = C_{N_1}\,\frac{S_1}{S}\left(\frac{x_{cg} - x_1}{l}\right)\left[\left(\frac{\partial C_{N_1}/\partial\alpha}{C_{N_1}}\right)_{\alpha=\alpha_1} - \left(\frac{\partial C_{N_2}/\partial\alpha}{C_{N_2}}\right)_{\alpha=\alpha_2}\right] \qquad \text{(B2)}$$

If the trim requirement is satisfied (eq. (B1)), a negative quantity $\partial C_{m_{cg}}/\partial\alpha$ (which is required for static stability) is obtained for bodies having trailing-edge controls if α_2 is less than α_1. For example, consider a flat-plate body and flat-plate trailing-edge control for which the curves presented in figures 24 and 25 are applicable. The inverse variation of $(\partial C_N/\partial\alpha)/C_N$ with α leads to a negative result for equation (B2) if α_2 is less than α_1. It is interesting to note that, for a given α_1 and $(x_2 - x_{cg})(S_2/S_1)$, $\partial C_{m_{cg}}/\partial\alpha$ varies with α_2 in such a manner as to attain a maximum absolute value in the neighborhood of $2\alpha_2 = \alpha_1$. Specifically, the maximum absolute value for $\partial C_{m_{cg}}/\partial\alpha$ occurs when α_2 is chosen so that the following relationship holds,

$$\left(\frac{\partial C_{N_2}}{\partial\alpha}\right)_{\alpha=\alpha_2}\left(\frac{\partial C_{N_1}}{\partial\alpha}\right)_{\alpha=\alpha_1} = C_{N_1}\left(\frac{\partial^2 C_{N_2}}{\partial\alpha^2}\right)_{\alpha=\alpha_2} \qquad \text{(B3)}$$

If both the body and the control are flat plates, then by means of Newtonian impact theory, equation (B3) is reduced to

$$\text{ctn}\ \alpha_2 - \tan\alpha_2 = 2\ \text{ctn}\ \alpha_1$$

which becomes an obvious trigonometric identity for $\alpha_1 = 2\alpha_2$. This result implies that, for a given static margin and configuration angle of attack α, the minimum control size required is obtained when $\alpha_2 = (1/2)\alpha_1$. (The center-of-gravity location x_{cg} is assumed to be that which satisfies the trim requirement eq. (B1).)

[redacted]

[redacted]

The appropriate size and deflection angle for the trailing-edge control may be estimated by first assuming an angle of attack α_1 for the body so that all quantities having subscripts 1 may be treated as constants. If a desired value for $\partial C_{m_{cg}}/\partial\alpha$ is then specified, equation (B2) defines a unique relationship between $(S_1/S)(x_1 - x_{cg}/l)$ and α_2 which, in turn, by virtue of equation (B1), specifies a value for the control size parameter $(x_2 - x_{cg}/l)(S_2/S_1)$.

The above discussion involved a configuration for which the body, by itself, is unstable. The trailing-edge control was used to provide static trim and stability. Consider next a hypersonic glider of the type shown in sketch (e) where an appreciable amount of longitudinal curvature is incorporated in the lower surface (the vehicle is shown with vertical symmetry for simplicity). For convenience the undersurface is divided into two regions (subscripts 1 and 2). If the trailing-edge controls are ignored, the equations given previously may be applied directly. The undersurface shape may be chosen so that the vehicle is self-trimming and has the desired static margin at the design angle of attack. (Such a vehicle may be described as having stick-free stability at the design angle of attack.)

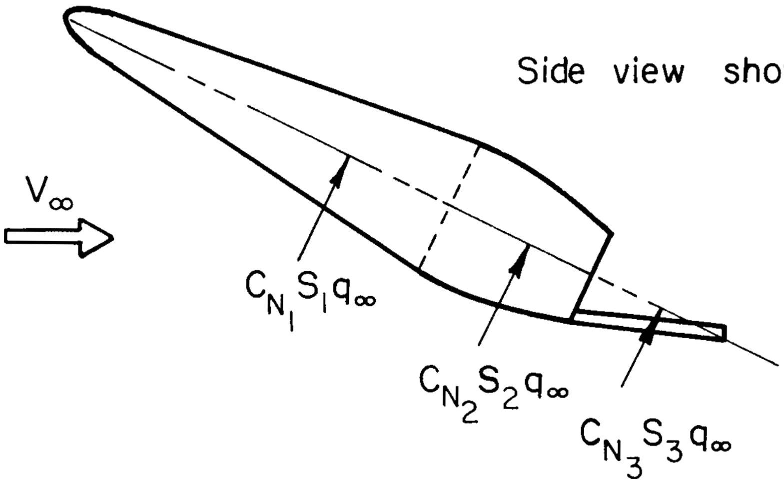

Sketch (e)

The use of a certain amount of longitudinal curvature appears desirable. It should be mentioned here that this type of body contouring could be used to advantage in reducing base area so as to alleviate the large base drag effects at low speeds. The upper surface shape is relatively unimportant at high angles of attack and hypersonic speeds so that the upper portion of the configuration could well be designed from low speed considerations, particularly with regard to reducing base drag effects. It should also be mentioned that the reduction in the vertical body

[redacted]

ordinates near the base, as illustrated in sketch (e), results in a forward shift of the center of pressure in pitch. This design procedure may be used to advantage in minimizing the center-of-pressure travel as the vehicle descends from hypersonic to subsonic Mach numbers.

A
2
5
9

REFERENCES

1. Allen, H. Julian, and Eggers, A. J., Jr.: A Study of the Motion and Aerodynamic Heating of Missiles Entering the Earth's Atmosphere at High Supersonic Speeds. NACA TN 4047, 1957.

2. Eggers, Alfred J., Jr., Allen, H. Julian, and Neice, Stanford E.: A Comparative Analysis of the Performance of Long-Range Hypervelocity Vehicles. NACA TN 4046, 1957. (Supersedes NACA RM A54L10)

3. Chapman, Dean R.: An Approximate Analytical Method for Studying Entry Into Planetary Atmospheres. NACA TN 4276, 1958.

4. Eggers, Alfred J., Jr., and Wong, Thomas J.: Re-entry and Recovery of Near-Earth Satellites, With Particular Attention to a Manned Vehicle. NASA MEMO 10-2-58A, 1958.

5. Eggers, A. J., Jr.: Performance of Long Range Hypervelocity Vehicles. Jet Propulsion, vol. 27, no. 11, Nov. 1957, pp. 1147-1151.

6. Jorgensen, Leland H.: Elliptic Cones Alone and With Wings at Supersonic Speeds. NACA Rep. 1376, 1958.

7. Spiegel, Joseph M., and Lawrence, Leslie F.: A Description of the Ames 2- by 2-Foot Transonic Wind Tunnel and Preliminary Evaluation of Wall Interference. NACA RM A55I21, 1956.

8. Eggers, A. J., Jr., and Nothwang, George J.: The Ames 10- by 14-Inch Supersonic Wind Tunnel. NACA TN 3095, 1954.

9. Jones, Robert T.: Properties of Low-Aspect-Ratio Pointed Wings at Speeds Below and Above the Speed of Sound. NACA Rep. 835, 1946. (Formerly NACA TN 1032)

10. Grimminger, G., Williams, E. P., and Young, G. B. W.: Lift on Inclined Bodies of Revolution in Hypersonic Flow. Jour. Aero. Sci., vol. 17, no. 11, Nov. 1950, pp. 675-690. (I.A.S. Preprint 247)

11. Lees, Lester: Hypersonic Flow. I.A.S. Preprint 554, 1955.

[redacted]

TABLE I.- BASE PRESSURE AND FORCE COEFFICIENTS AT LOW SPEEDS

Model	M_∞	α, deg	C_{p_b}	$C_{A_b} = -C_{p_b}\frac{A_b}{S}$	Model	M_∞	α, deg	C_{p_b}	$C_{A_b} = -C_{p_b}\frac{A_b}{S}$
1	0.6	0	-0.283	0.119	3	0.6	0	-0.244	0.075
		5.1	-.302	.127			5.1	-.265	.081
		10.2	-.333	.147			10.3	-.339	.104
		15.3	-.395	.167			15.4	-.414	.127
	.9	0	-.322	.136		.9	0	-.294	.090
		5.2	-.340	.143			5.2	-.310	.095
		10.3	-.365	.154			10.4	-.385	.118
		15.5	-.429	.181			15.7	-.457	.140
	1.0	0	-.500	.211		1.0	0	-.486	.149
		5.1	-.511	.216			5.2	-.481	.148
		10.3	-.518	.218			10.5	-.561	.172
		15.5	-.600	.253			15.8	-.641	.197
	1.1	0	-.415	.175		1.1	0	-.387	.119
		5.2	-.422	.178			5.2	-.408	.125
		10.3	-.451	.190			10.5	-.479	.147
		15.5	-.509	.214			15.8	-.552	.169
	1.3	0	-.329	.139		1.3	0	-.306	.094
		5.2	-.346	.146			5.3	-.342	.105
		10.4	-.392	.165			10.5	-.397	.122
		15.5	-.443	.187			15.9	-.474	.145
2	.6	0	-.280	.129	4	.6	0	-.238	.050
		5.1	-.298	.137			5.2	-.272	.057
		10.2	-.330	.152			10.3	-.345	.073
		15.3	-.385	.177			15.5	-.443	.094
	.9	0	-.312	.144		.9	0	-.296	.063
		5.1	-.334	.154			5.2	-.313	.066
		10.3	-.364	.167			10.5	-.396	.084
		15.4	-.409	.188			15.8	-.498	.105
	1.0	0	-.503	.231		1.0	0	-.468	.099
		5.1	-.503	.231			5.3	-.511	.108
		10.3	-.509	.234			10.5	-.619	.131
		15.5	-.576	.265			15.9	-.670	.142
	1.1	0	-.416	.191		1.1	0	-.377	.080
		5.2	-.422	.193			5.3	-.420	.089
		10.3	-.446	.205			10.6	-.525	.111
		15.5	-.516	.237			14.9	-.567	.120
	1.3	0	-.344	.158		1.3	0	-.309	.065
		5.2	-.356	.164			5.3	-.343	.072
		10.4	-.390	.180			9.5	-.410	.087
		15.6	-.463	.213			16.0	-.470	.099

A
2
5
9

[redacted]

[redacted]

TABLE II.- CENTERS OF PRESSURE AT LOW SPEEDS

Model	M_∞	α, deg	$\frac{X_N}{l_2}$	$\frac{X_Y}{l_2}$	Model	M_∞	α, deg	$\frac{X_N}{l_2}$	$\frac{X_Y}{l_2}$
1	0.6	0 7.1 14.3	0.643 .639 .630	0.719 .723 .747	3	0.6	0 7.2 14.4	0.650 .636 .643	0.716 .749 .741
	.9	0 7.2 14.4	.660 .660 .656	.737 .744 .753		.9	0 7.3 14.7	.668 .661 .678	.727 .762 .786
	1.0	0 7.2 14.5	.660 .662 .648	.751 .742 .757		1.0	0 7.3 14.7	.670 .670 .685	.744 .753 .763
	1.1	0 7.2 14.5	.660 .654 .655	.757 .736 .749		1.1	0 7.3 14.7	.668 .669 .683	.713 .753 .771
	1.3	0 7.2 14.5	.664 .682 .677	.750 .740 .746		1.3	0 7.4 14.8	.682 .698 .701	.730 .758 .734
2	.6	0 7.1 14.3	.657 .634 .640	.734 .734 .734	4	.6	0 7.2 14.4	.628 .612 .623	.644 .660 .673
	.9	0 7.2 14.4	.675 .670 .662	.760 .753 .754		.9	0 7.3 14.7	.655 .657 .659	.674 .700 .656
	1.0	0 7.2 14.4	.678 .656 .670	.759 .781 .765		1.0	0 7.3 14.8	.655 .663 .669	.689 .700 .727
	1.1	0 7.2 14.4	.674 .658 .647	.750 .752 .749		1.1	0 7.3 14.9	.655 .655 .659	.659 .686 .623
	1.3	0 7.2 14.5	.678 .674 .680	.746 .752 .757		1.3	0 7.4 14.9	.664 .653 .672	.640 .681 .652

A
2
5
9

[redacted]

[redacted]

TABLE III.- BASE PRESSURE AND FORCE COEFFICIENTS AT HIGH SPEEDS

Model	M_∞	α, deg	Measured C_{p_b}	Measured $C_{A_b} = -C_{p_b}\frac{A_b}{S}$	Estimated $C_{A_b} = \frac{1}{M_\infty^2}\frac{A_b}{S}$	Model	M_∞	α, deg	Measured C_{p_b}	Measured $C_{A_b} = -C_{p_b}\frac{A_b}{S}$	Estimated $C_{A_b} = \frac{1}{M_\infty^2}\frac{A_b}{S}$
1	3	0	-0.117	0.049	0.0468	3	3	0	-0.115	0.0352	0.0340
		14.5	-.126	.053				15.7	-.119	.0364	
		40.6	-.111	.047				40.6	-.102	.0312	
		51.7	-.109	.046				50.6	-.109	.0334	
	4	0	-.072	.030	.0263		4	0	-.072	.0220	.0191
		14.4	-.079	.033				15.8	-.072	.0220	
	5	0	-.039	.016	.0168		5	0	-.038	.0116	.0122
		14.3	-.046	.019				15.3	-.041	.0125	
		40.4	-.031	.013				45.4	-.030	.0092	
		49.5	-.028	.012							
	6	0	-.025	.011	.0117		6	0	-.023	.0070	.0085
		14.1	-.028	.012					-.028	.0086	
2	3	0	-.109	.0500	.0510	4	3	0	-.117	.0247	.0235
		15.5	-.119	.0546				15.8	-.126	.0266	
		30.6	-.112	.0514				40.7	-.113	.0238	
		45.5	-.107	.0491				50.7	-.111	.0234	
	4	0	-.069	.0317	.0287		4	0	-.073	.0154	.0132
		15.5	-.071	.0326				15.9	-.076	.0160	
	5	0	-.034	.0160	.0184		5	0	-.039	.0082	.0084
		15.2	-.038	.0174				15.3	-.044	.0093	
		30.4	-.037	.0170				40.4	-.032	.0068	
		45.4	-.027	.0124				49.6	-.030	.0063	
	6	0	-.021	.0096	.0128		6	0	-.018	.0038	.0059
		15.1	-.023	.0106				15.2	-.026	.0055	

[redacted]

[redacted]

TABLE IV.- CENTERS OF PRESSURE AT HIGH SPEEDS

Model	M_∞	α, deg	$\frac{X_N}{l_2}$	$\frac{X_Y}{l_2}$	Model	M_∞	α, deg	$\frac{X_N}{l_2}$	$\frac{X_Y}{l_2}$
1	3	0	0.682	0.732	3	3	0	0.708	0.753
		7.3	.675	.758			7.3	.710	.714
		14.5	.661	.728			14.7	.713	.760
		40.7	.663	.717			40.6	.712	.804
		47.6	.692	.714			47.6	.705	.781
	4	0	.691	.726		4	0	.718	.775
		7.3	.696	.749			7.4	.724	.775
		14.6	.667	.736			14.8	.716	.767
	5	0	.686	.735		5	0	.725	.772
		7.1	.718	.723			7.1	.764	.788
		14.3	.670	.734			14.3	.729	.769
		40.4	.677	.728			40.4	.742	.810
		47.5	.667	.738			47.5	.721	.811
	6	0	.690	.717		6	0	.735	.750
		7.1	.701	.690			7.1	.748	.762
		14.1	.638	.725			14.1	.735	.781
2	3	0	.715	.740	4	3	0	.680	.679
		7.2	.708	.764			7.4	.670	.723
		14.4	.723	.759			14.7	.659	.675
		40.6	.712	.753			40.7	.640	.665
		47.5	.705	.765			47.7	.643	.676
	4	0	.725	.753		4	0	.694	.662
		7.3	.715	.766			7.4	.710	.709
		14.5	.732	.766			14.8	.670	.679
	5	0	.735	.730		5	0	.692	.670
		7.1	.745	.776			7.2	.704	.715
		14.2	.753	.732			14.3	.670	.696
		40.4	.706	.766			40.4	.658	.661
		47.4	.713	.723			47.5	.652	.685
	6	0	.735	---		6	0	.698	---
		7.0	.750	.794			7.1	.592	---
		14.1	.740	---			14.2	.673	---

[redacted]

[redacted]

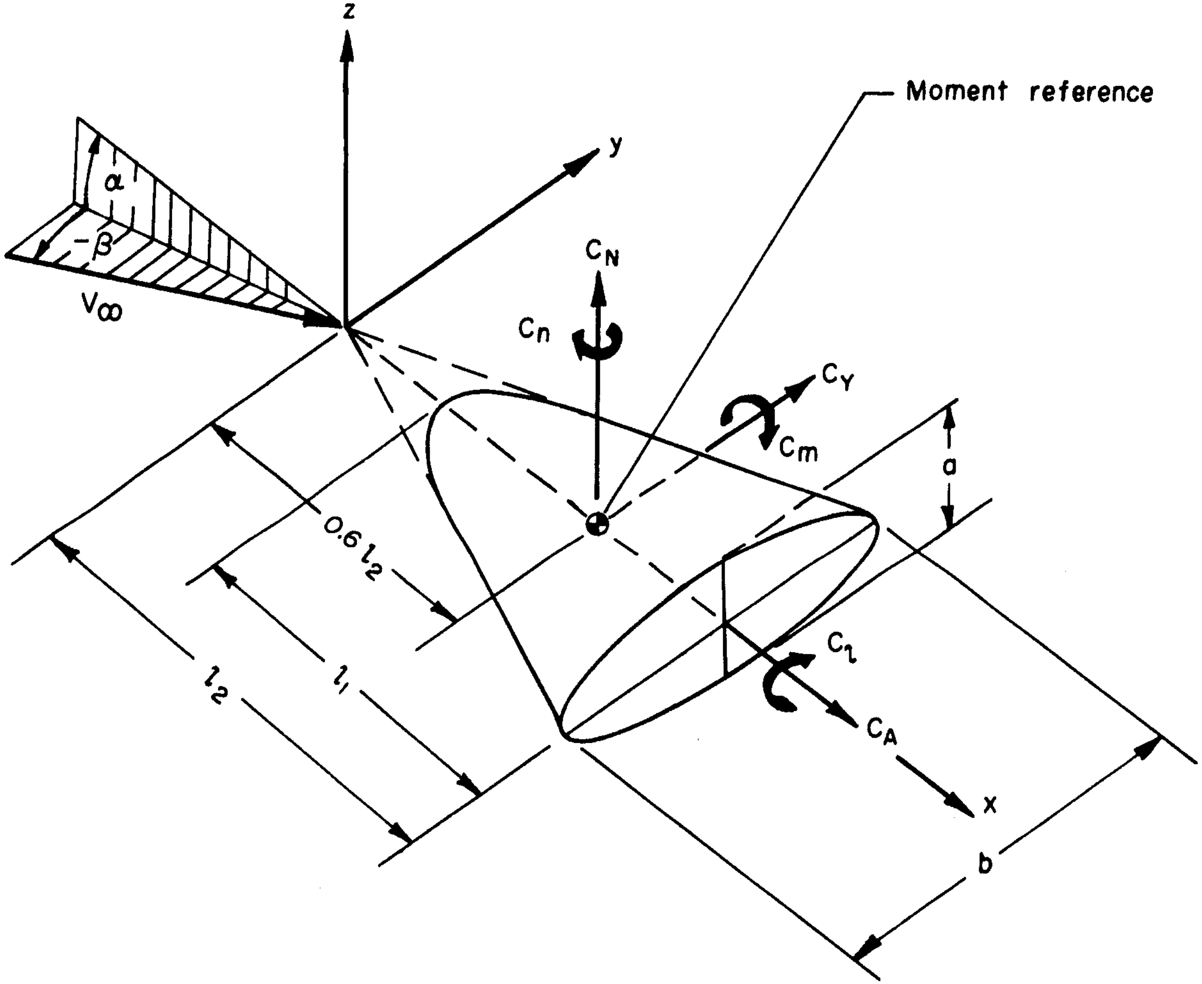

Figure 1.- Nomenclature.

[redacted]

[redacted]

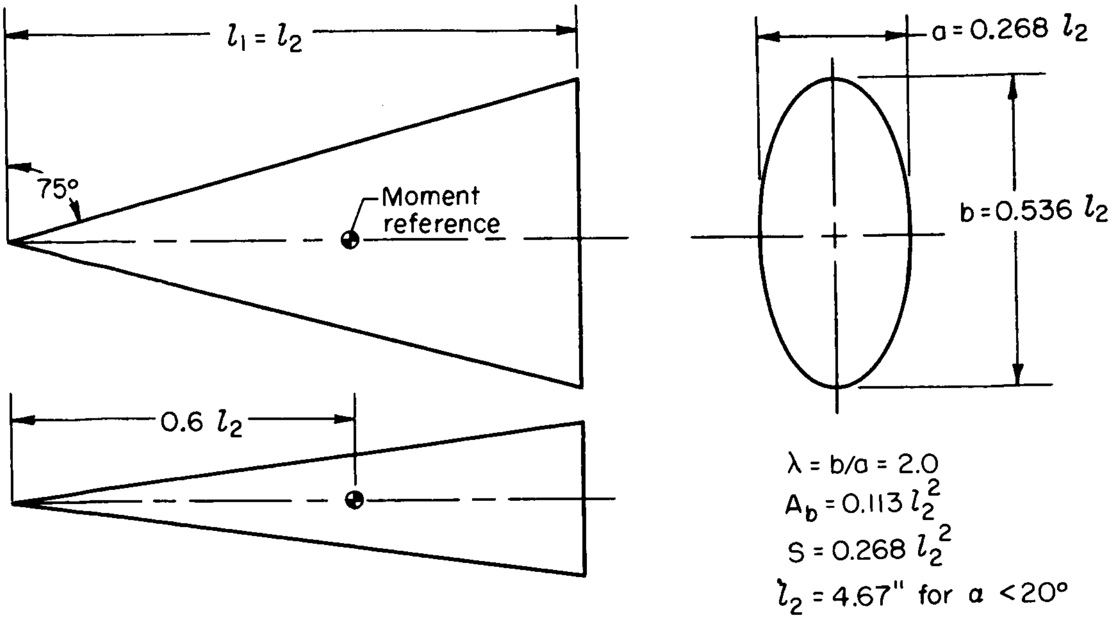

(a) Model 1

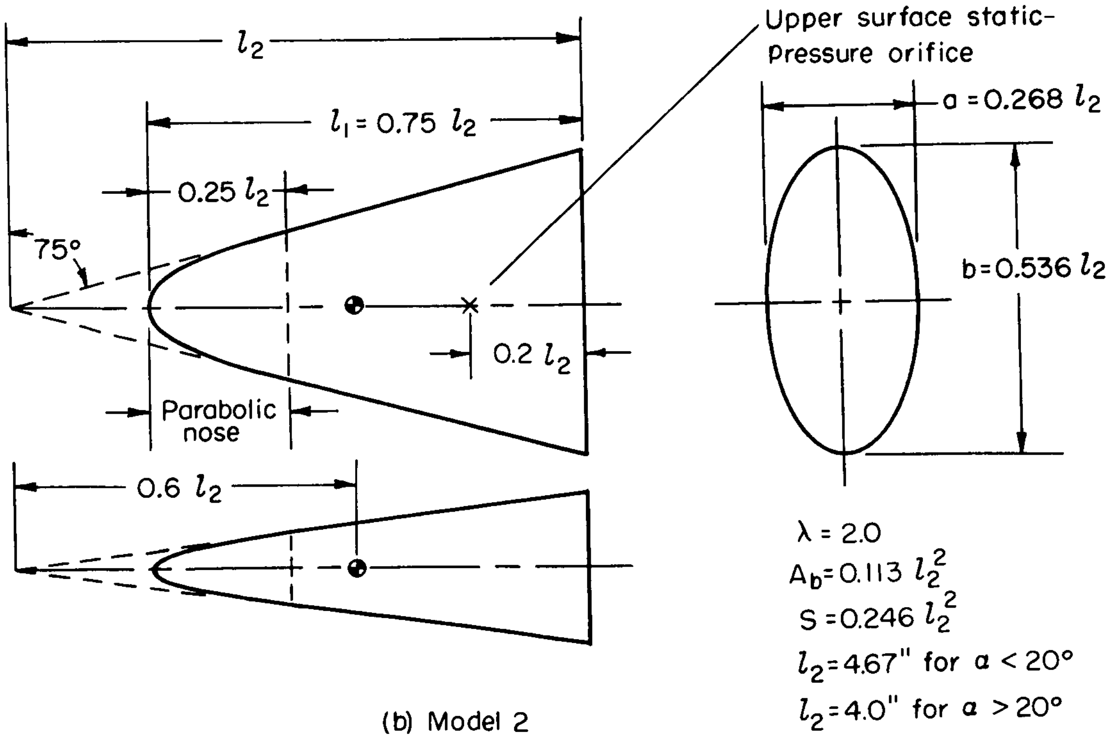

(b) Model 2

Figure 2.- Geometry of basic configurations.

[redacted]

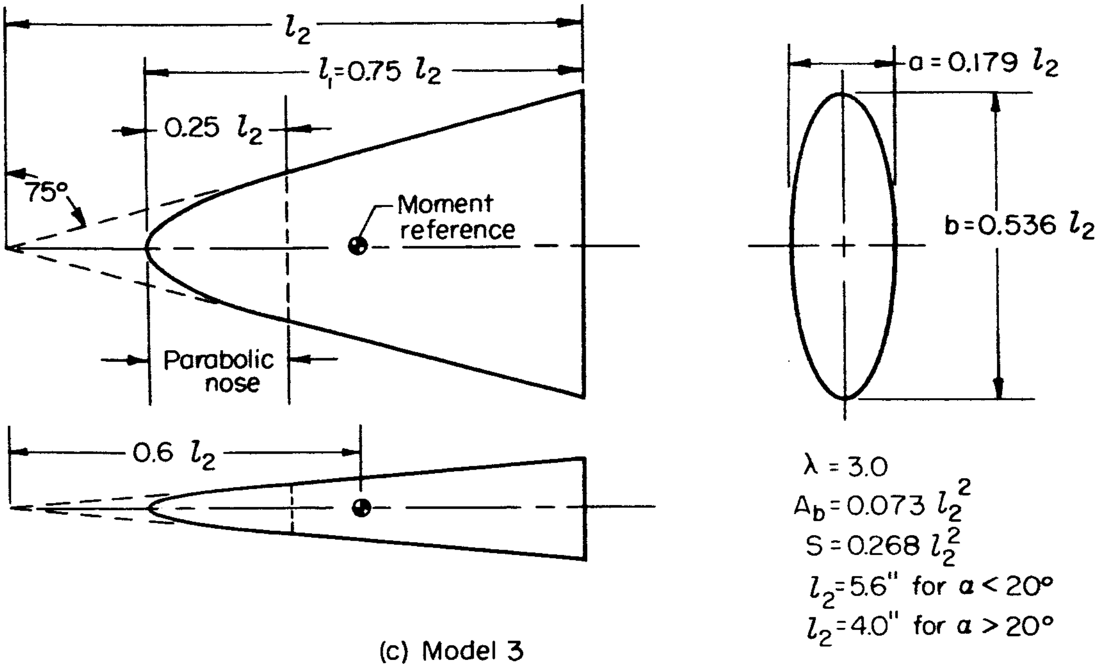

(c) Model 3

A
2
5
9

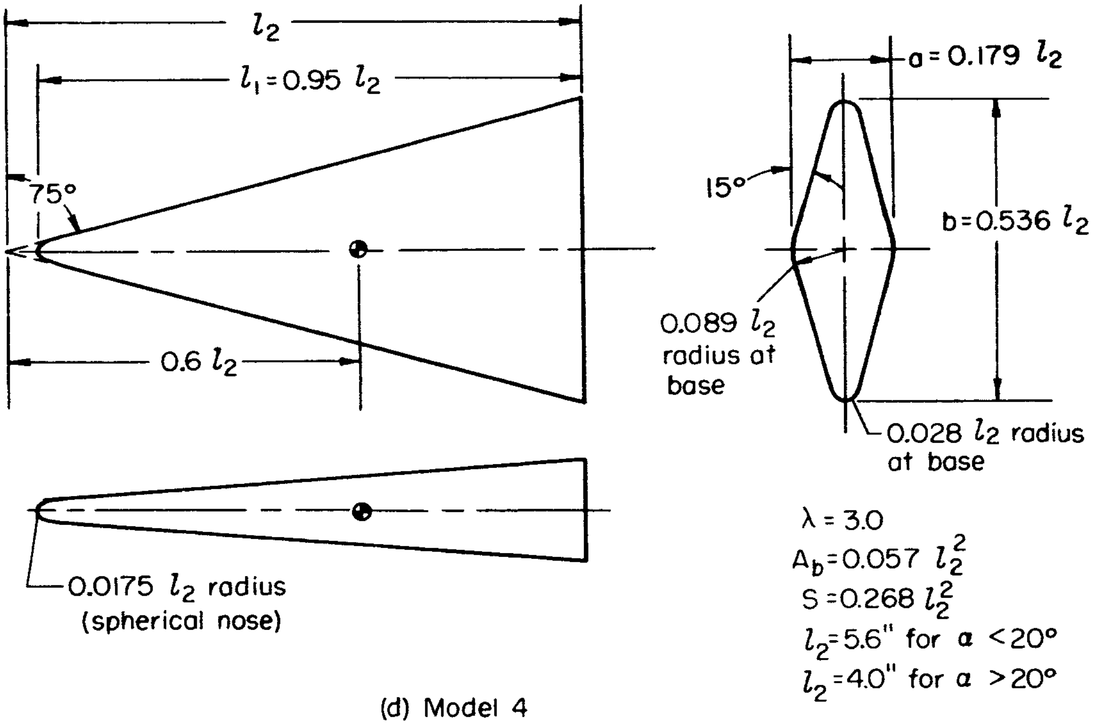

(d) Model 4

Figure 2.- Concluded.

[redacted]

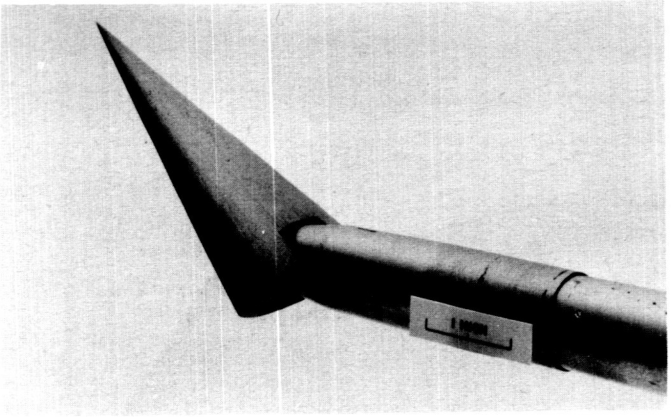

Small model. A-25086

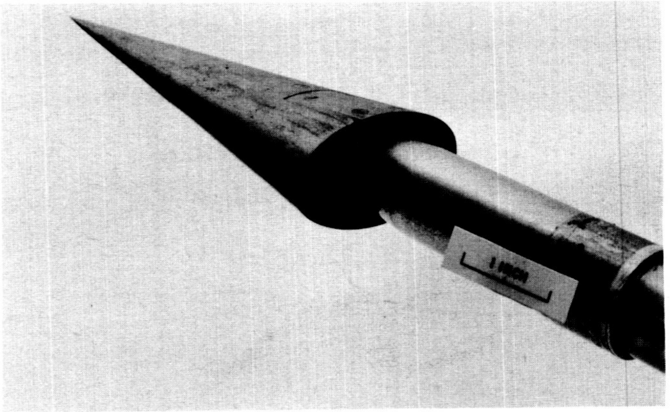

Large model. A-25085

(a) Model 1.

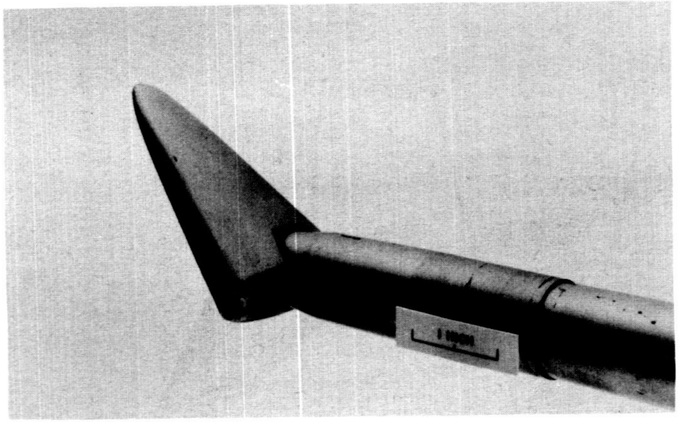

Small model. A-25088

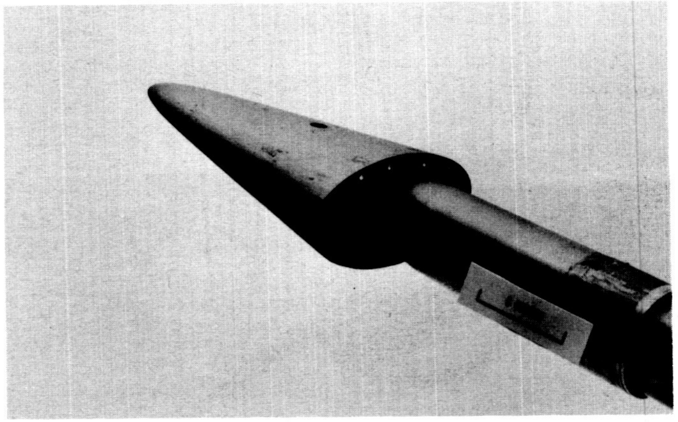

Large model. A-25087

(b) Model 2.

Figure 3.- Photographs of the models.

A
2
5
9

[redacted]

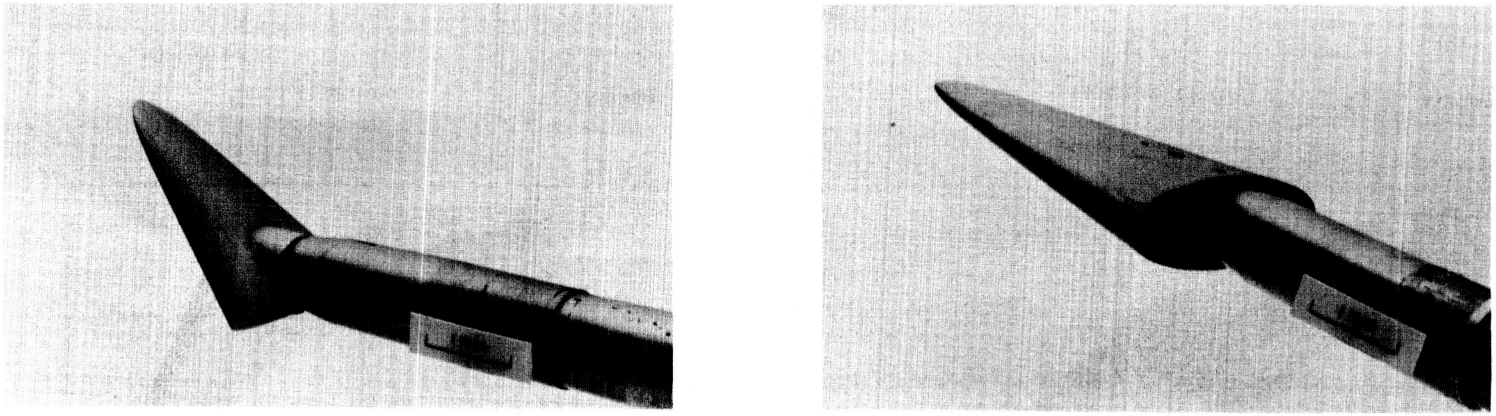

Small model. A-25090

Large model. A-25089

(c) Model 3.

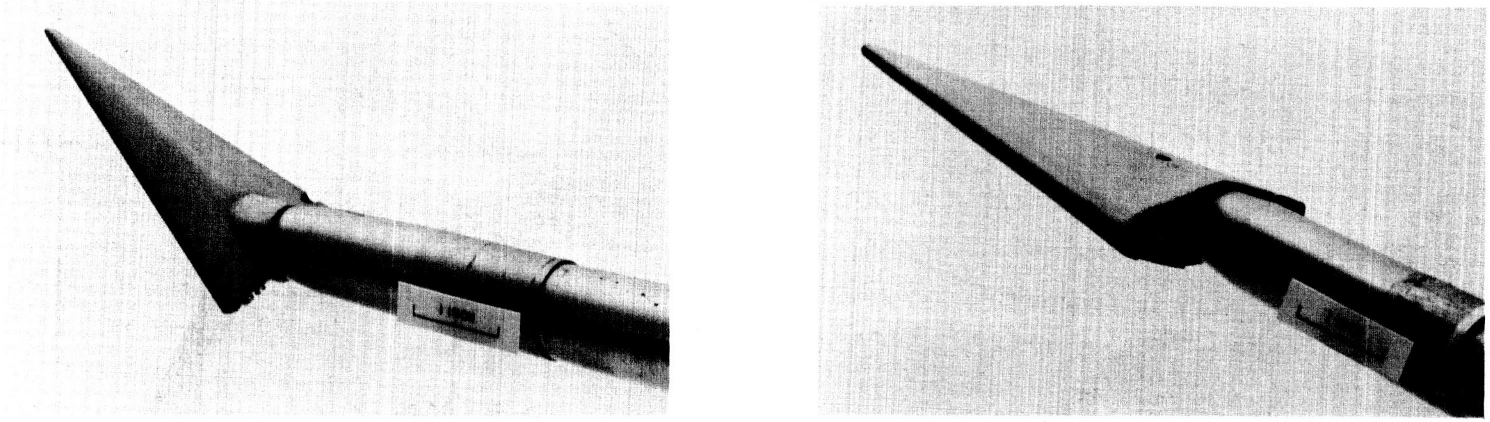

Small model. A-25092

Large model. A-25091

(d) Model 4.

Figure 3.- Concluded.

[redacted]

[redacted]

[redacted]

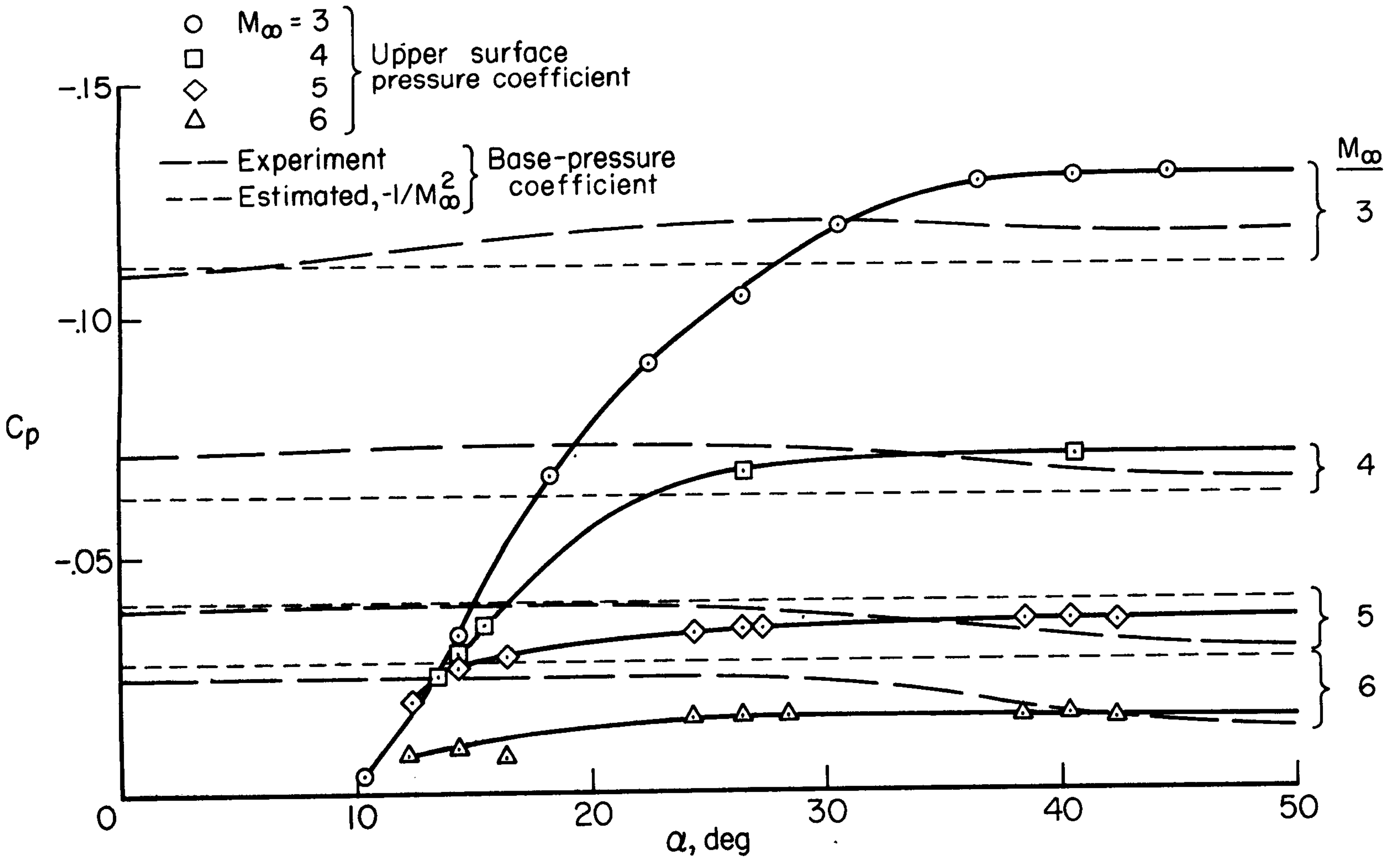

Figure 4.- Measured pressure coefficients at the upper surface of model 2.

[redacted]

A
2
5
9

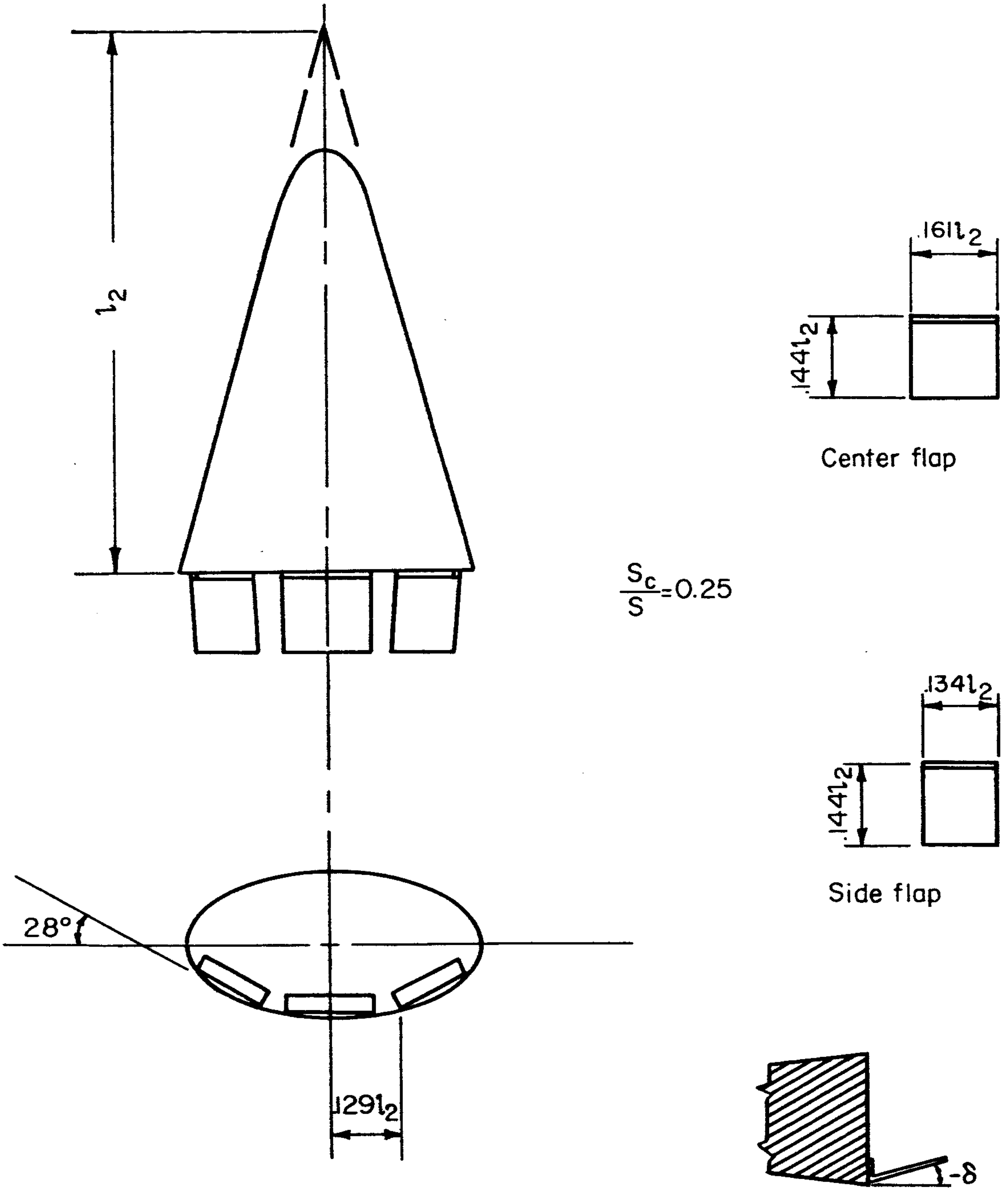

(a) Trailing-edge controls (model 2).

Figure 5.- Geometry of controls.

[redacted]

[redacted]

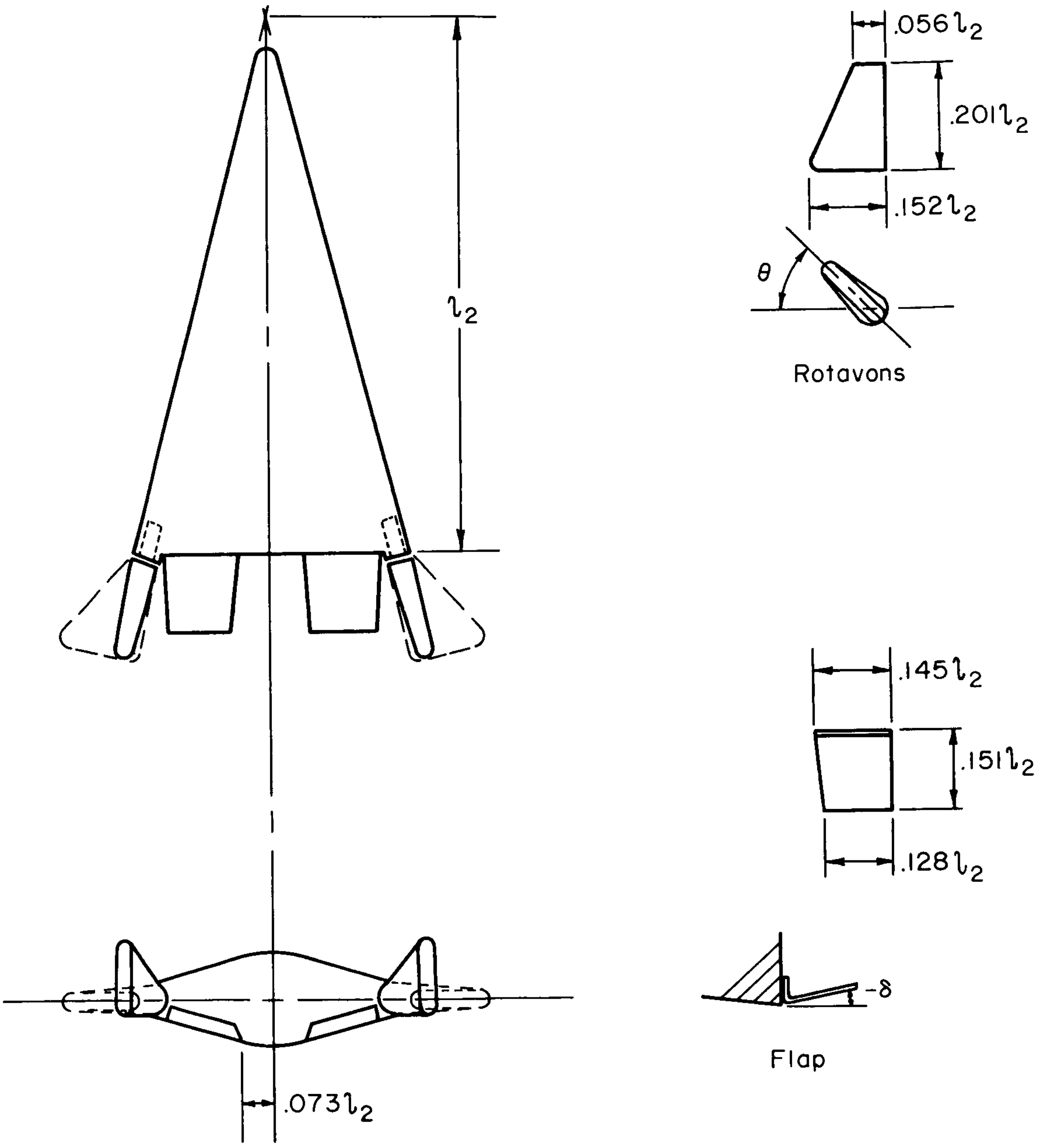

(b) Trailing-edge and tip controls (model 4)

Figure 5.- Continued.

[redacted]

A
2
5
9

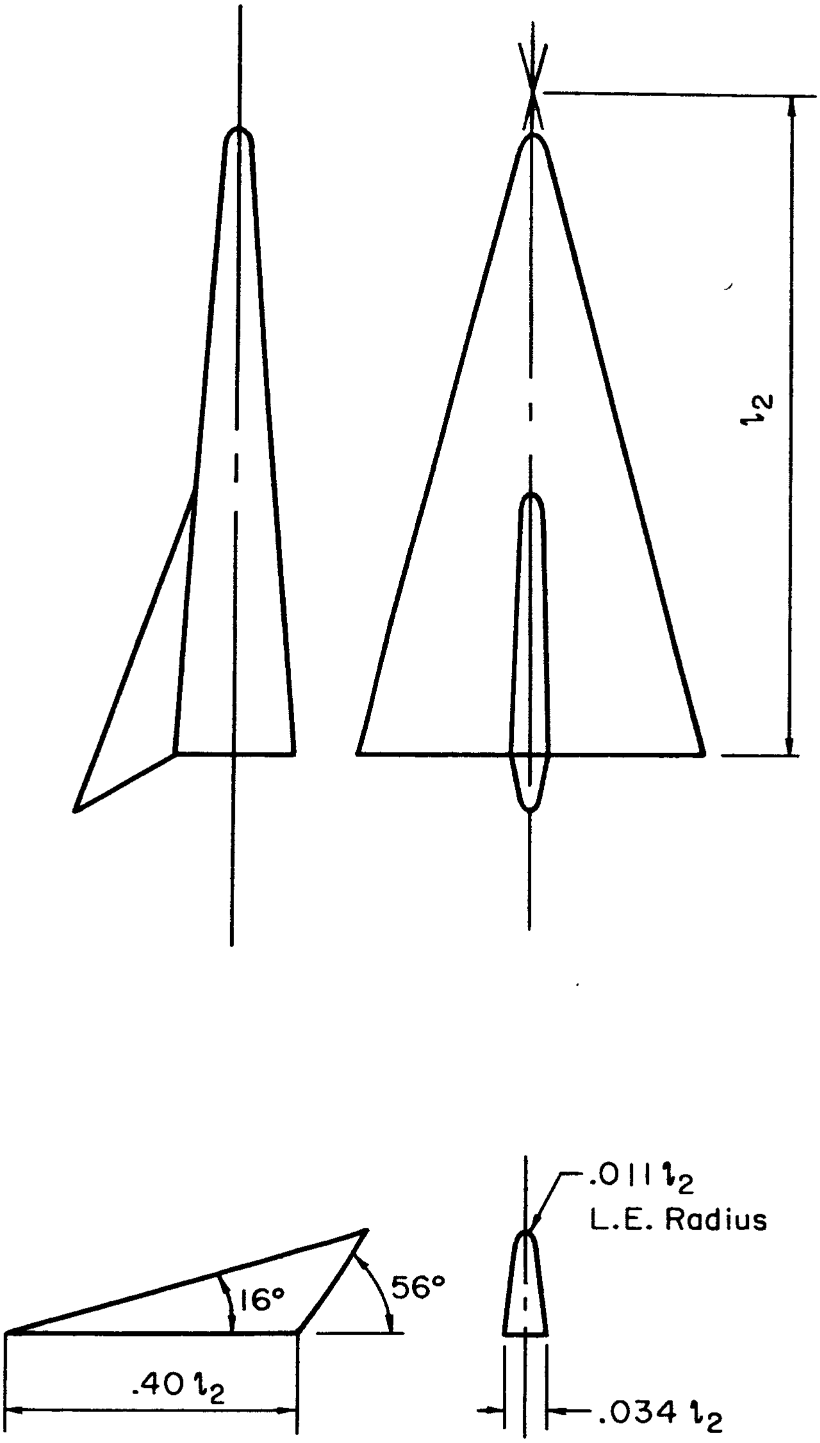

(c) Dorsal fin (model 4)

Figure 5.- Concluded.

[redacted]

[redacted]

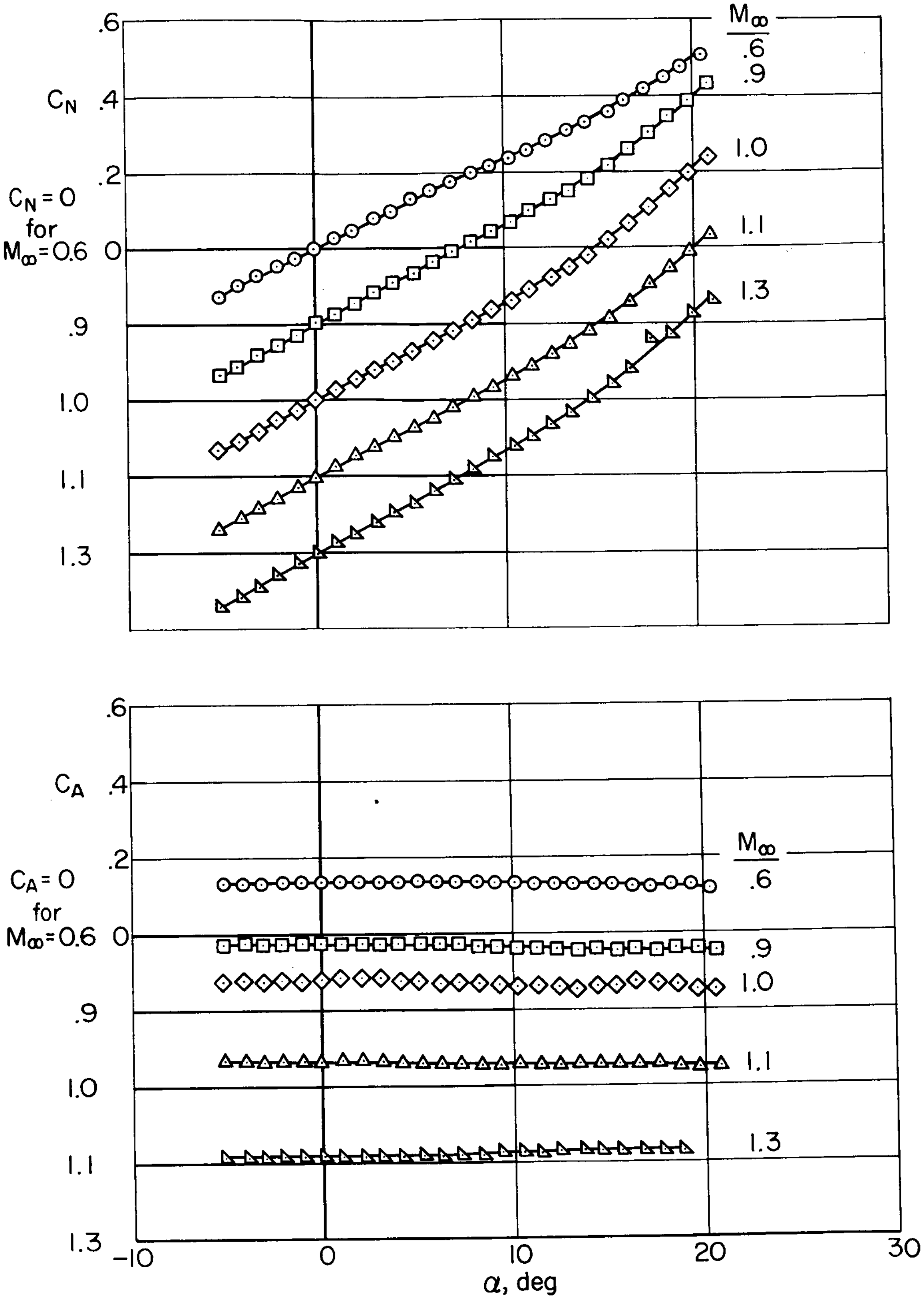

(a) Normal and axial forces

Figure 6.- Aerodynamic characteristics of model 1; M_∞ = 0.6 to 1.3.

[redacted]

A
2
5
9

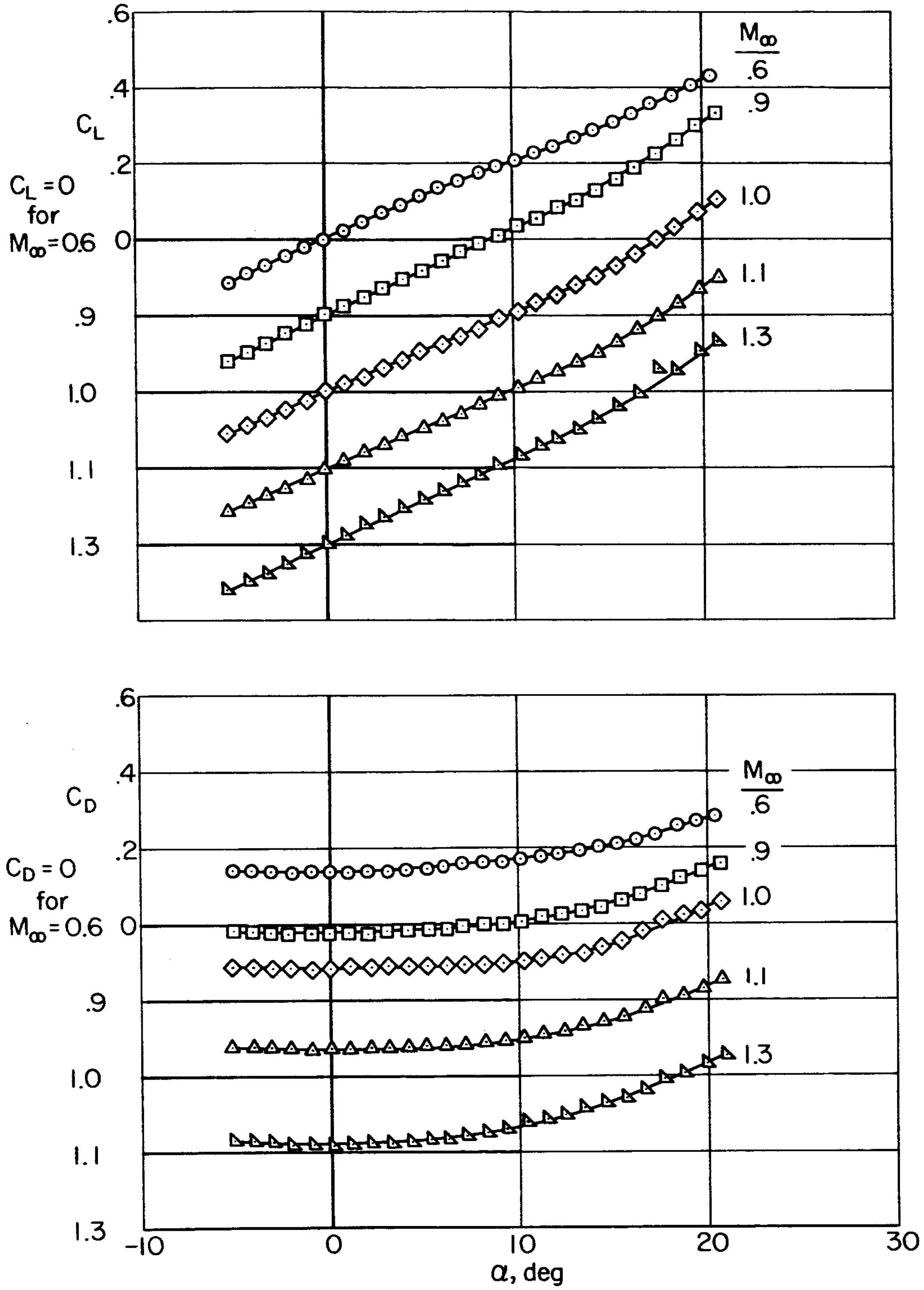

(b) Lift and drag

Figure 6.- Continued.

[redacted]

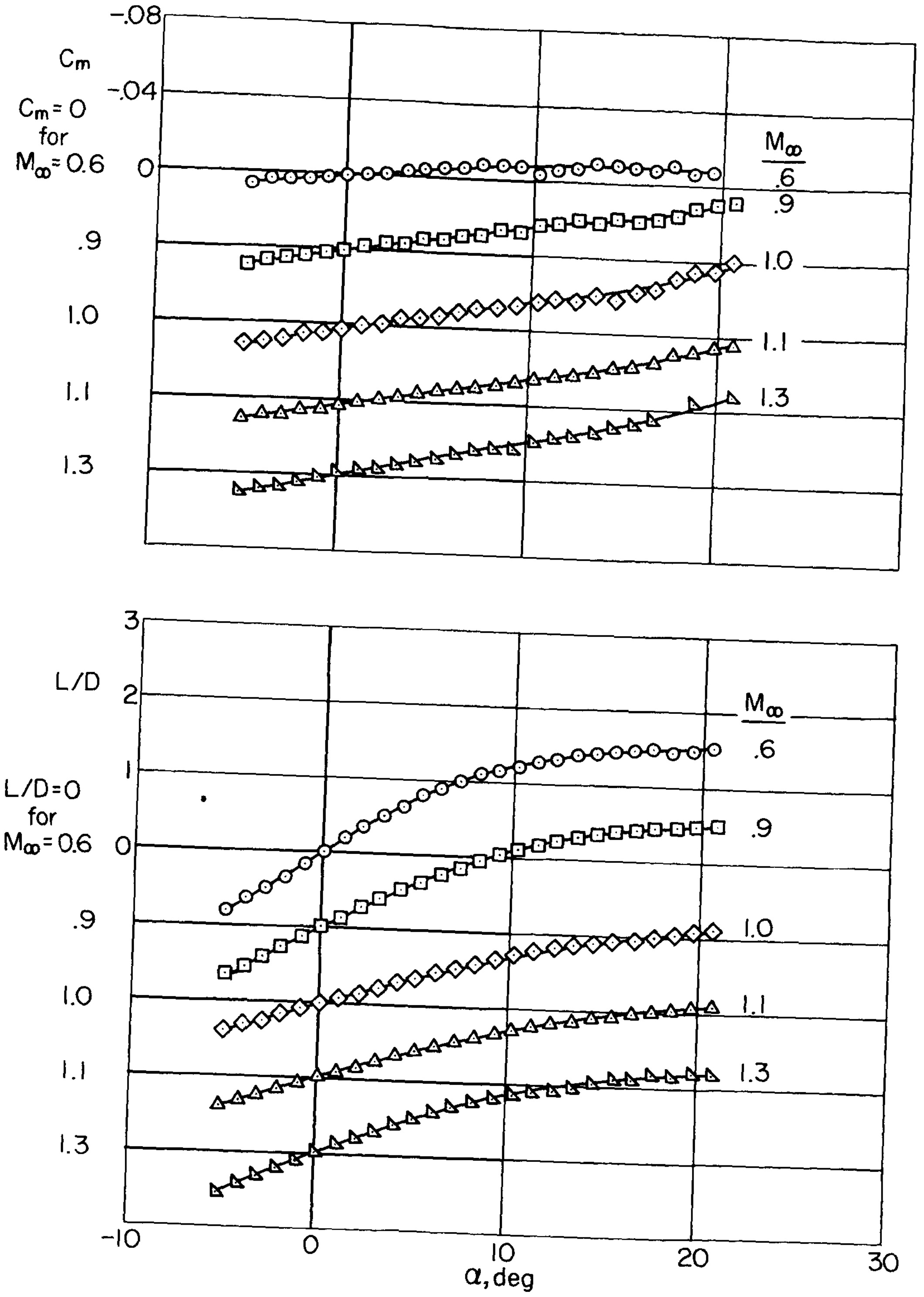

(c) Pitching moment and lift-drag ratio

Figure 6.- Continued.

[redacted]

[redacted]

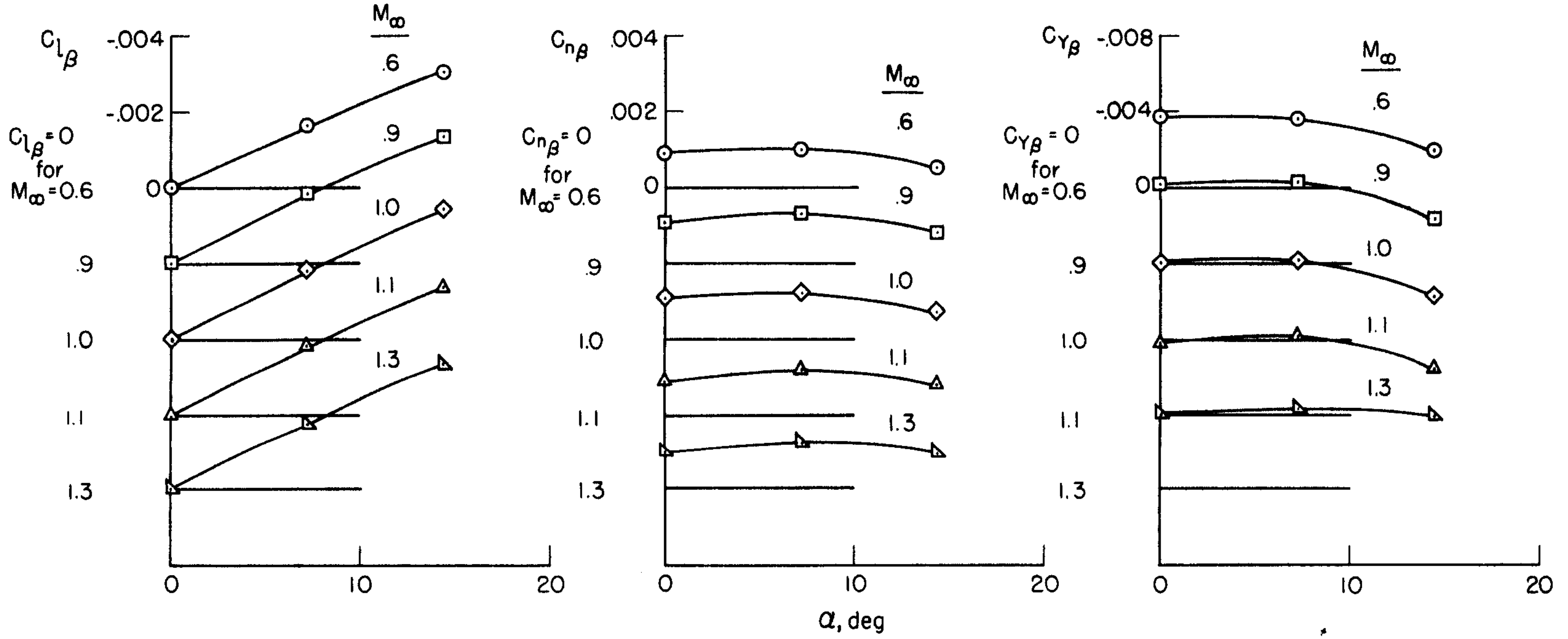

(d) Lateral stability derivatives

Figure 6.- Concluded.

[redacted]

[redacted]

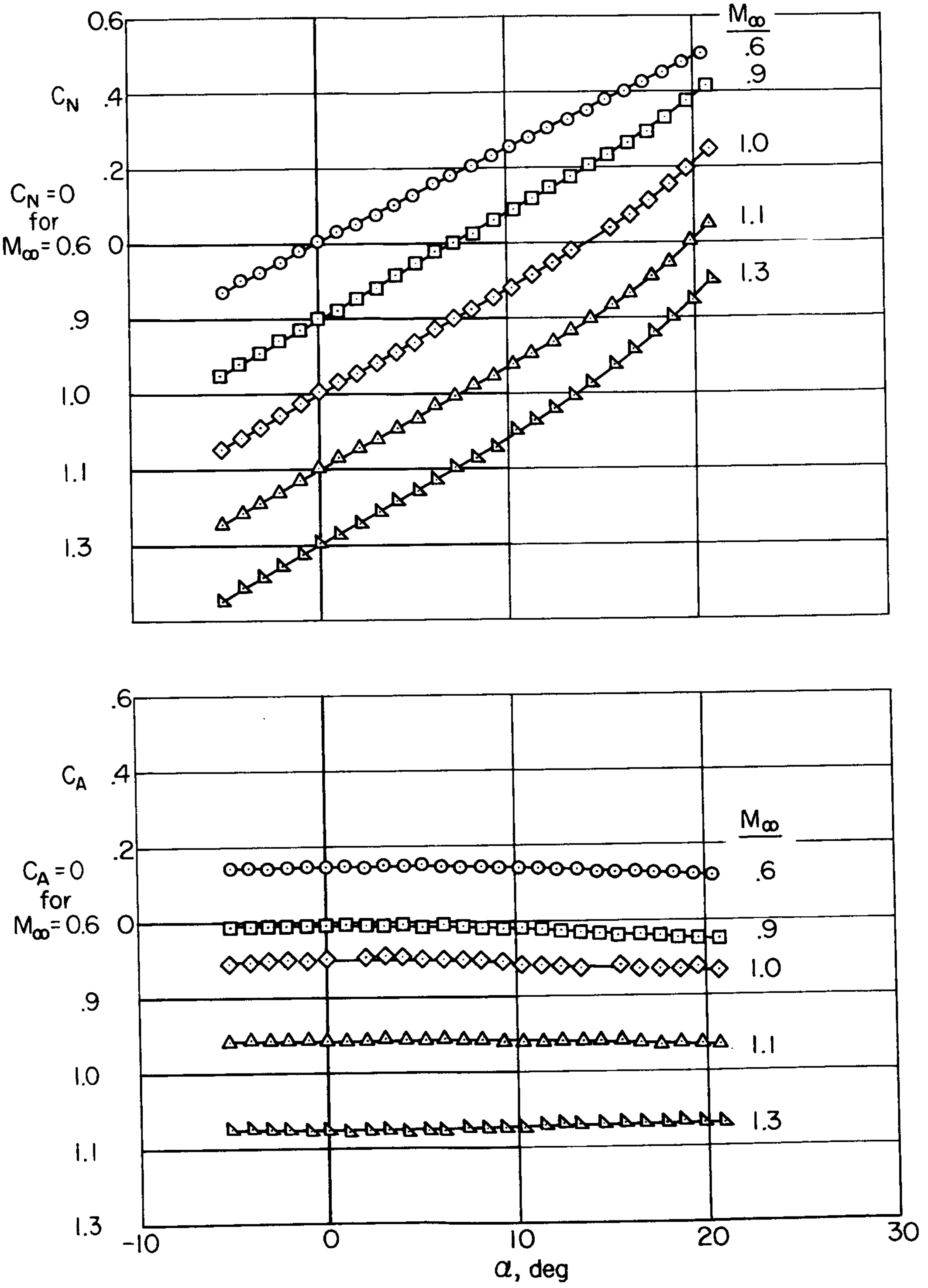

(a) Normal and axial forces.

Figure 7.- Aerodynamic characteristics of model 2; $M_\infty = 0.6$ to 1.3.

A
2
5
9

[redacted]

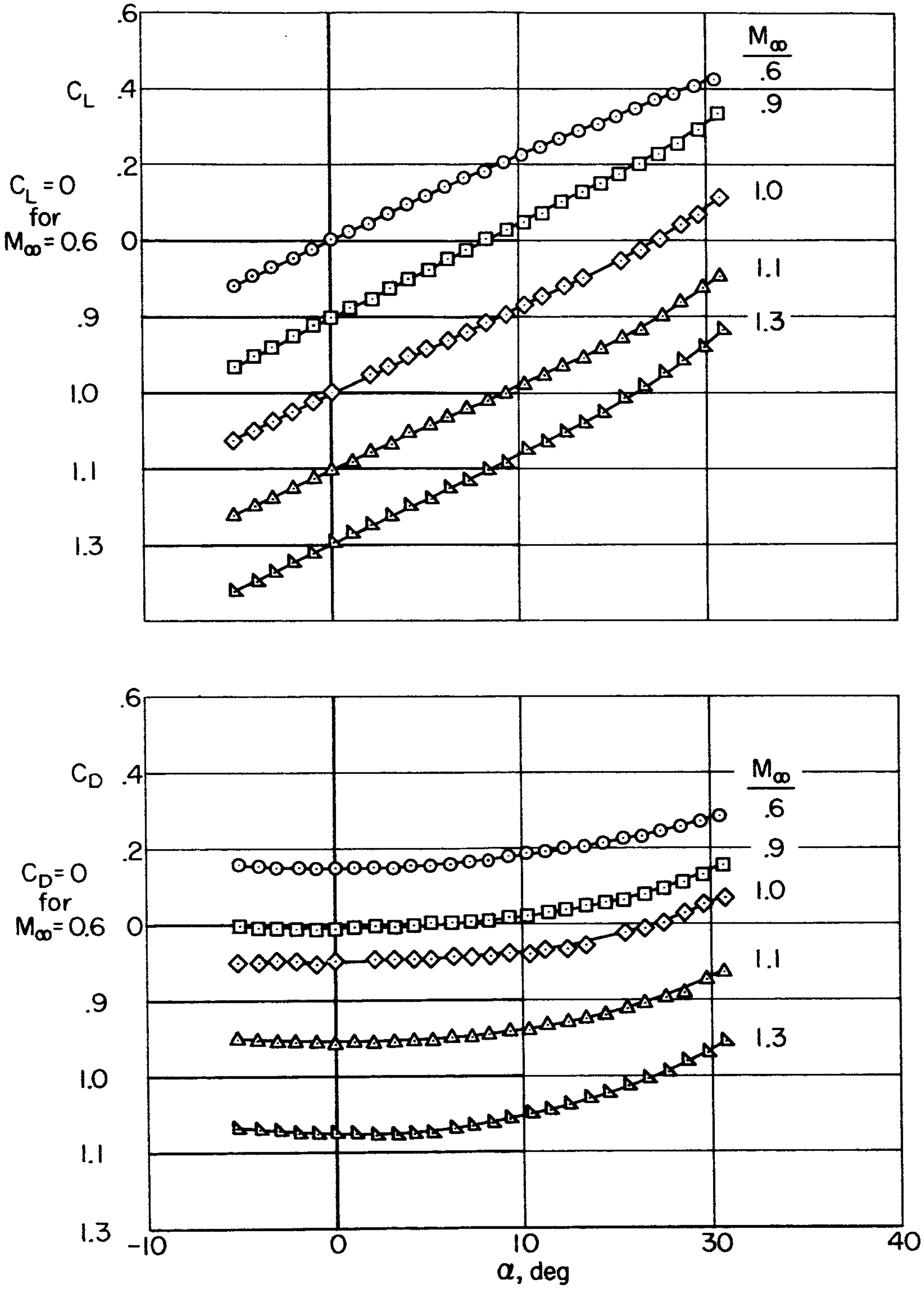

(b) Lift and drag.

Figure 7.- Continued.

[redacted]

[redacted]

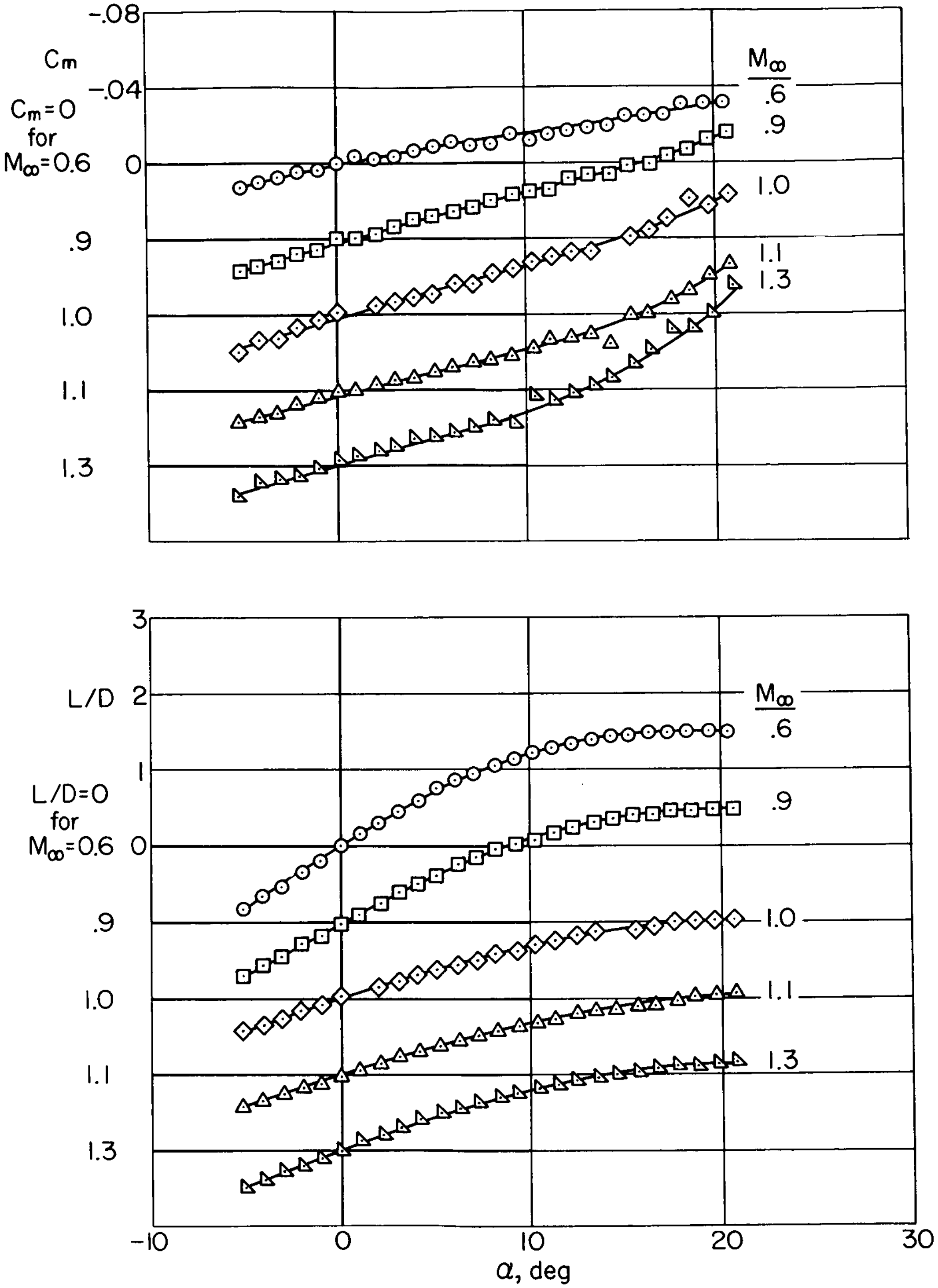

(c) Pitching moment and lift-drag ratio.

Figure 7.- Continued.

[redacted]

[redacted]

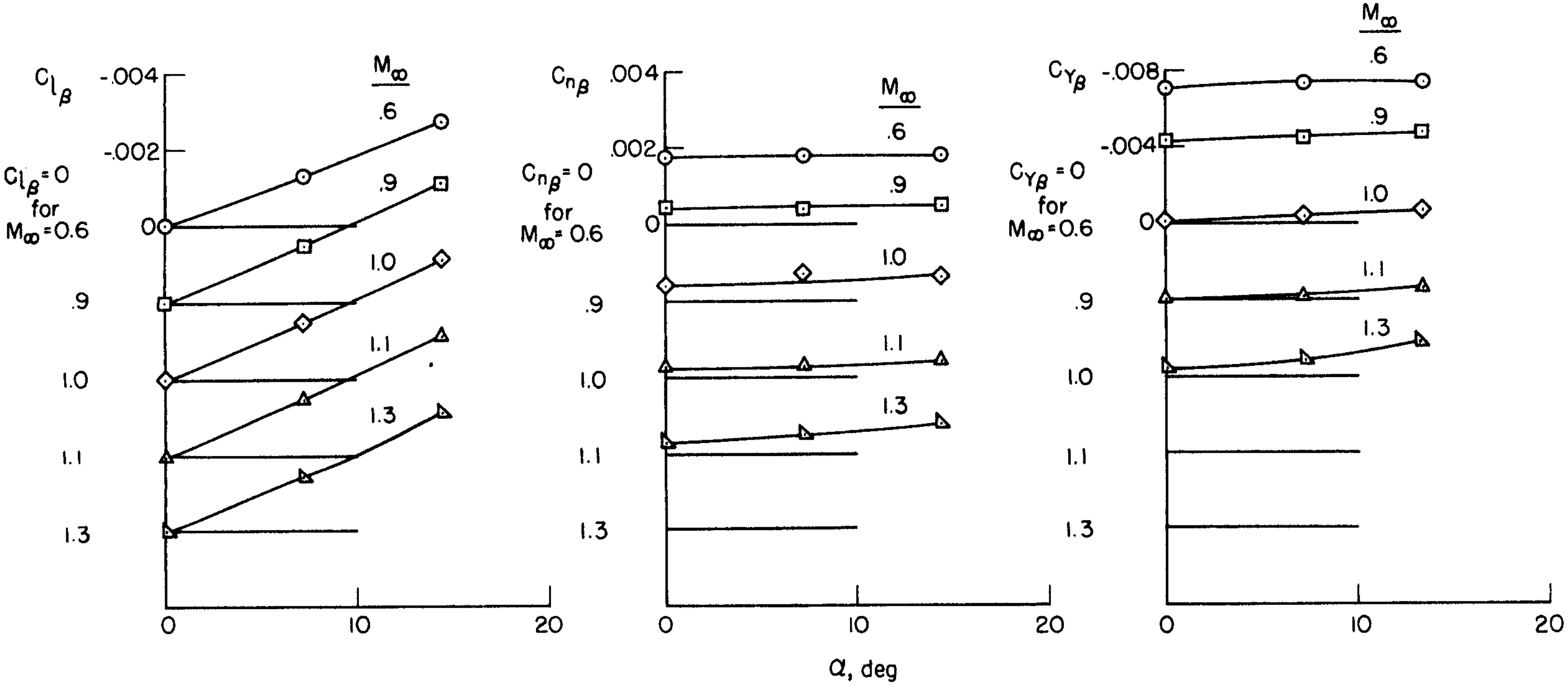

(d) Lateral stability derivatives.

Figure 7.- Concluded.

[redacted]

[redacted]

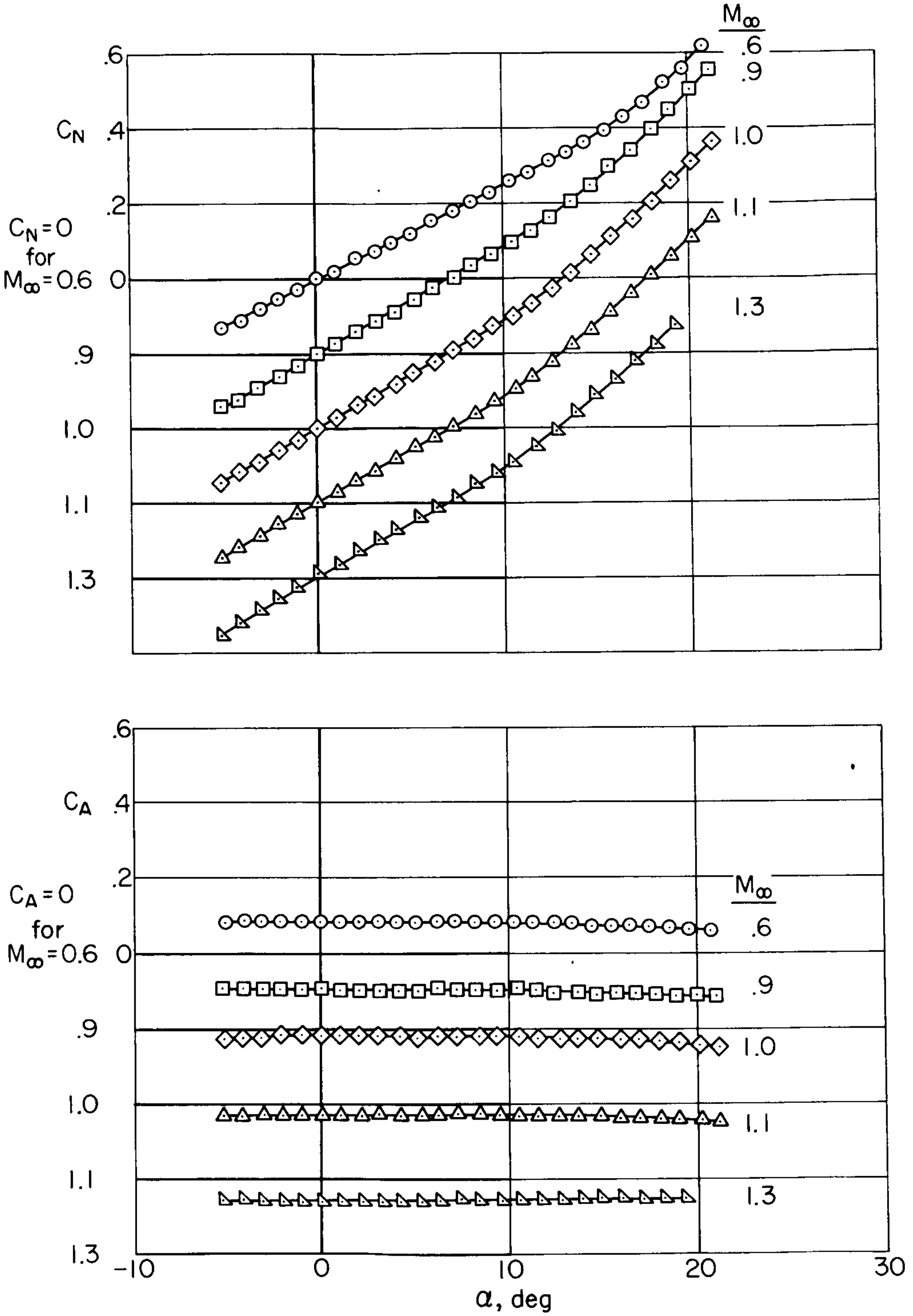

(a) Normal and axial force.

Figure 8.- Aerodynamic characteristics of model 3; M_∞ = 0.6 to 1.3.

[redacted]

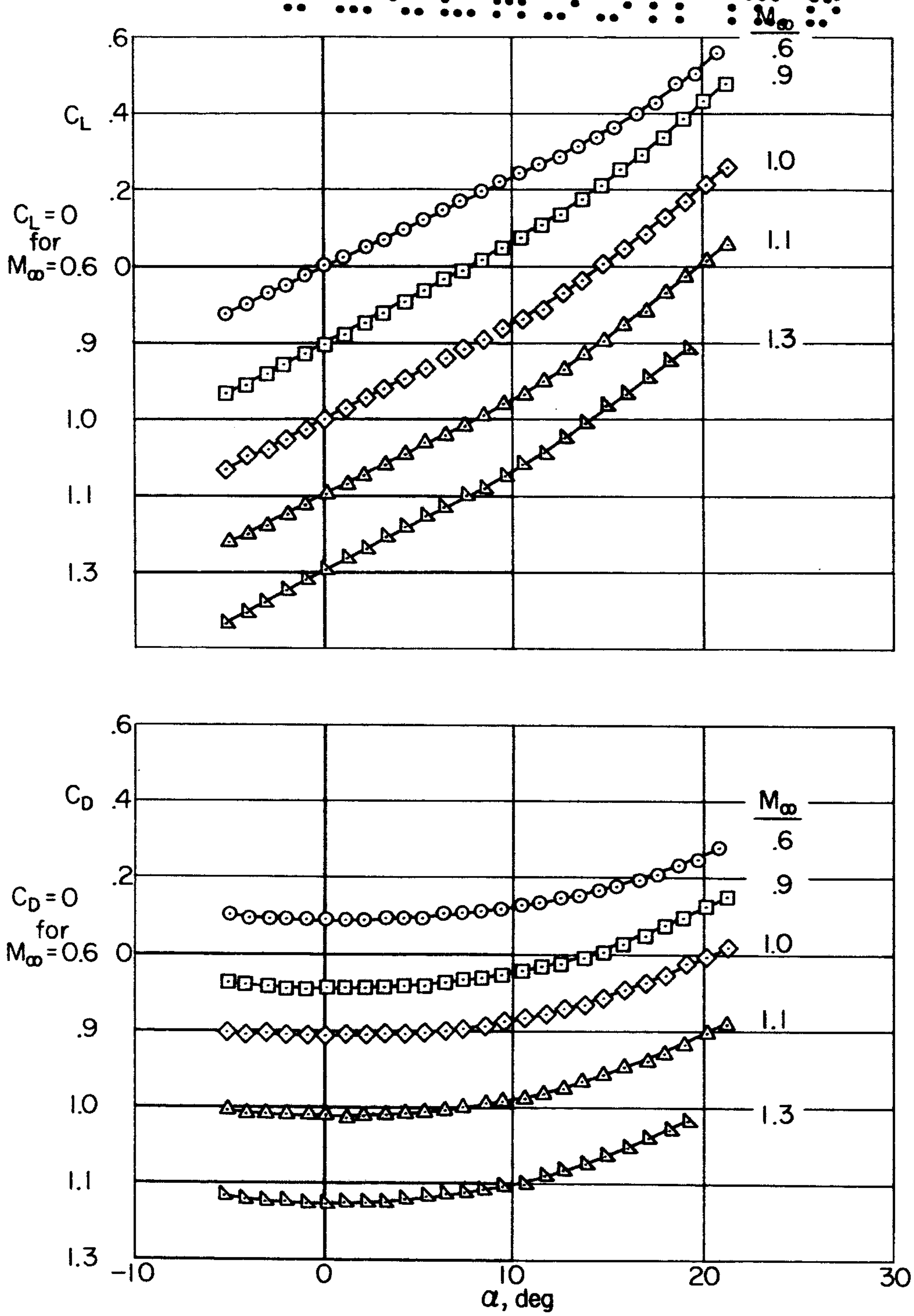

(b) Lift and drag.

Figure 8.- Continued.

[redacted]

[redacted]

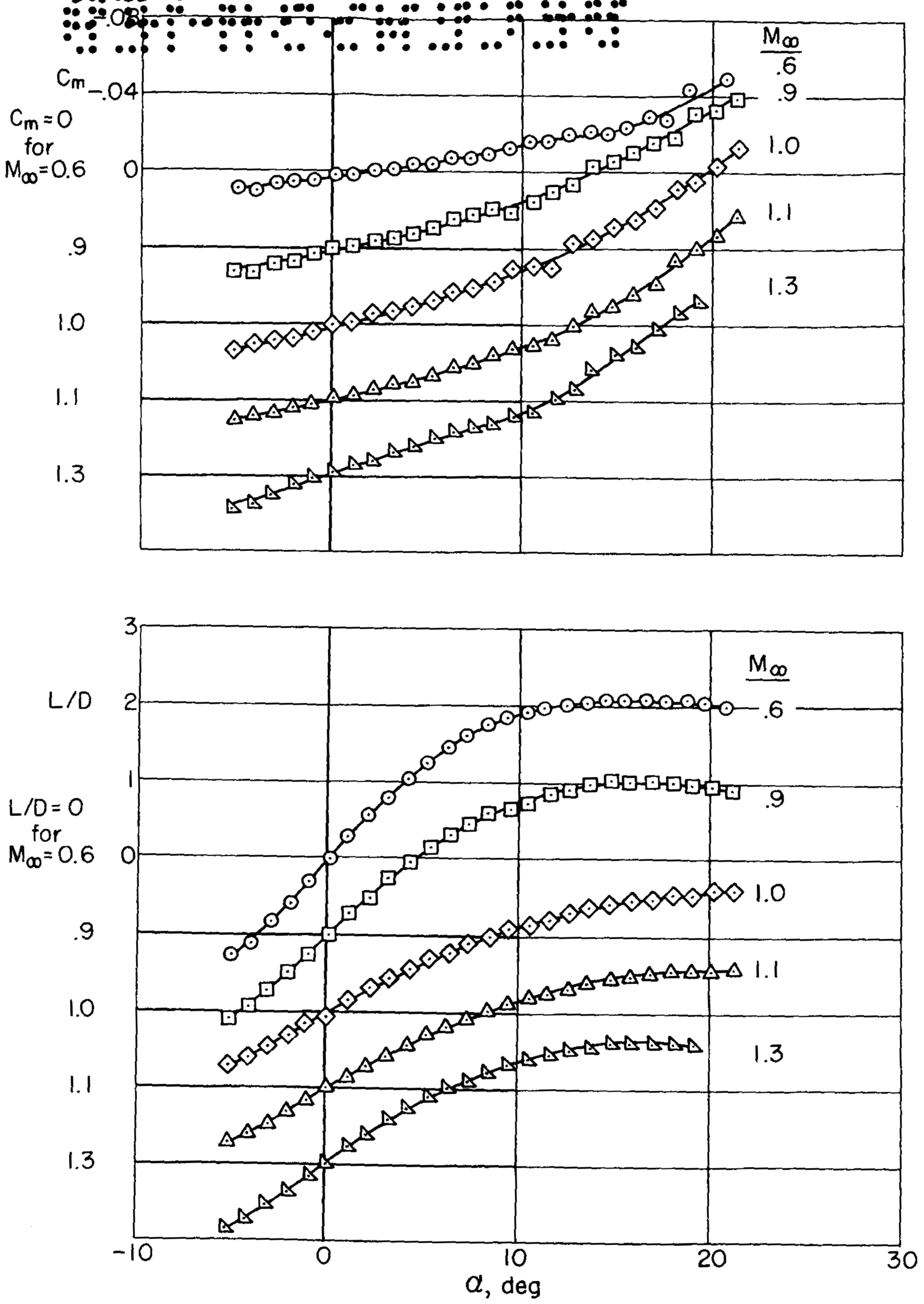

(c) Pitching moment and lift-drag ratio.

Figure 8.- Continued.

[redacted]

A
2
5
9

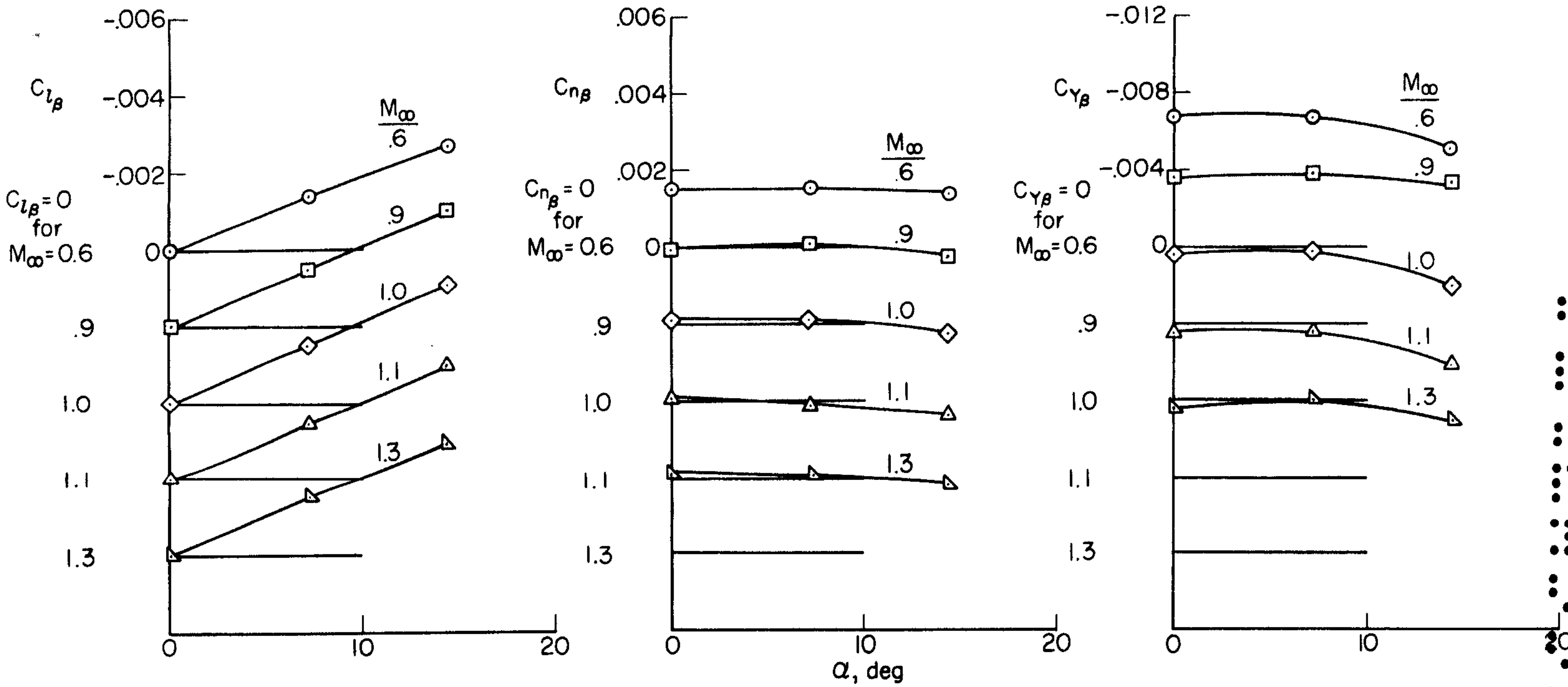

(d) Lateral stability derivatives

Figure 8.- Concluded.

[redacted]

[redacted]

[redacted]

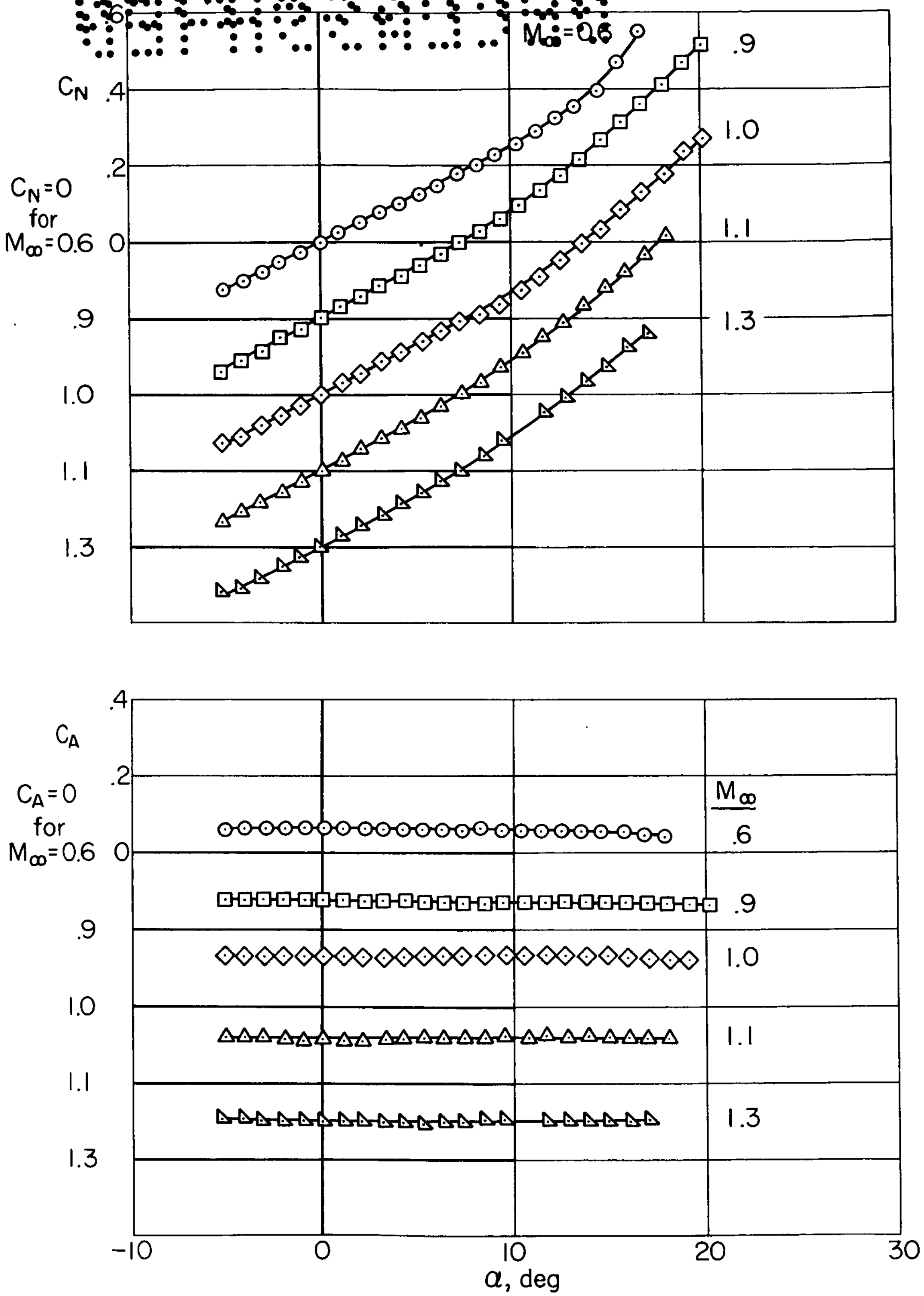

(a) Normal and axial forces.

Figure 9.- Aerodynamic characteristics of model 4; M_∞ = 0.6 to 1.3.

A
2
5
9

[redacted]

[redacted]

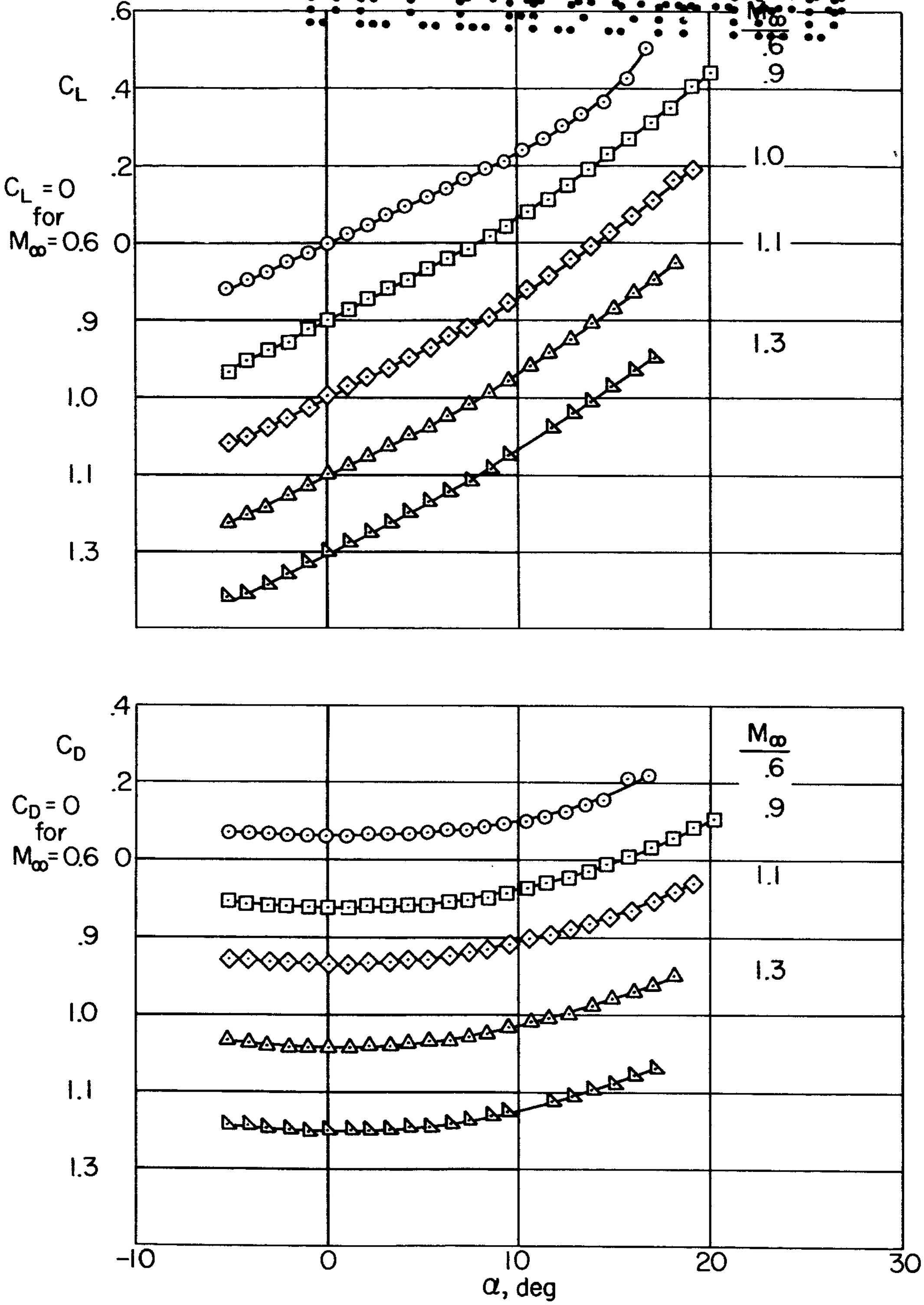

(b) Lift and drag.

Figure 9.- Continued.

[redacted]

[redacted]

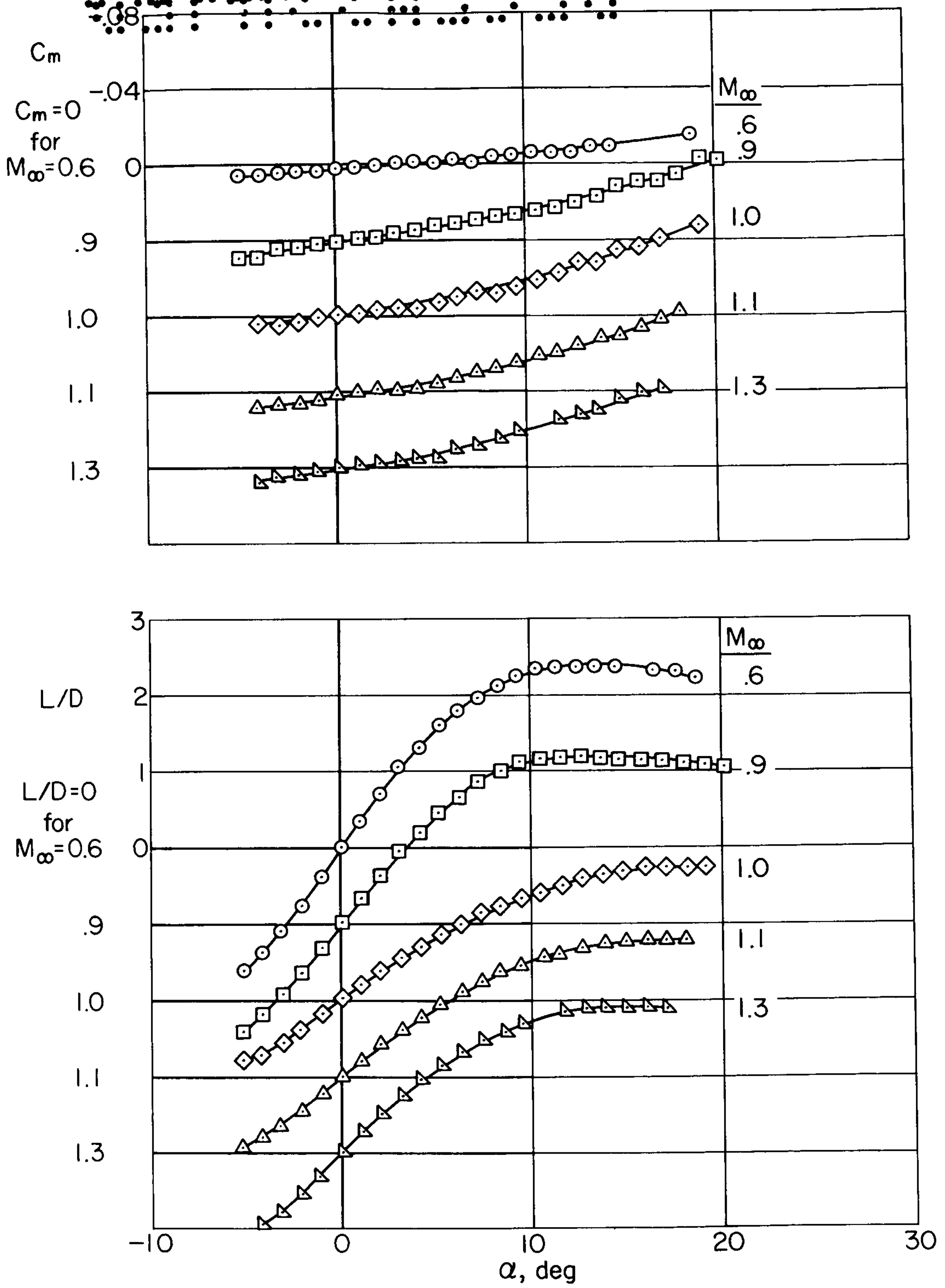

(c) Pitching moment and lift-drag ratio.

Figure 9.- Continued.

[redacted]

A 2 5 9

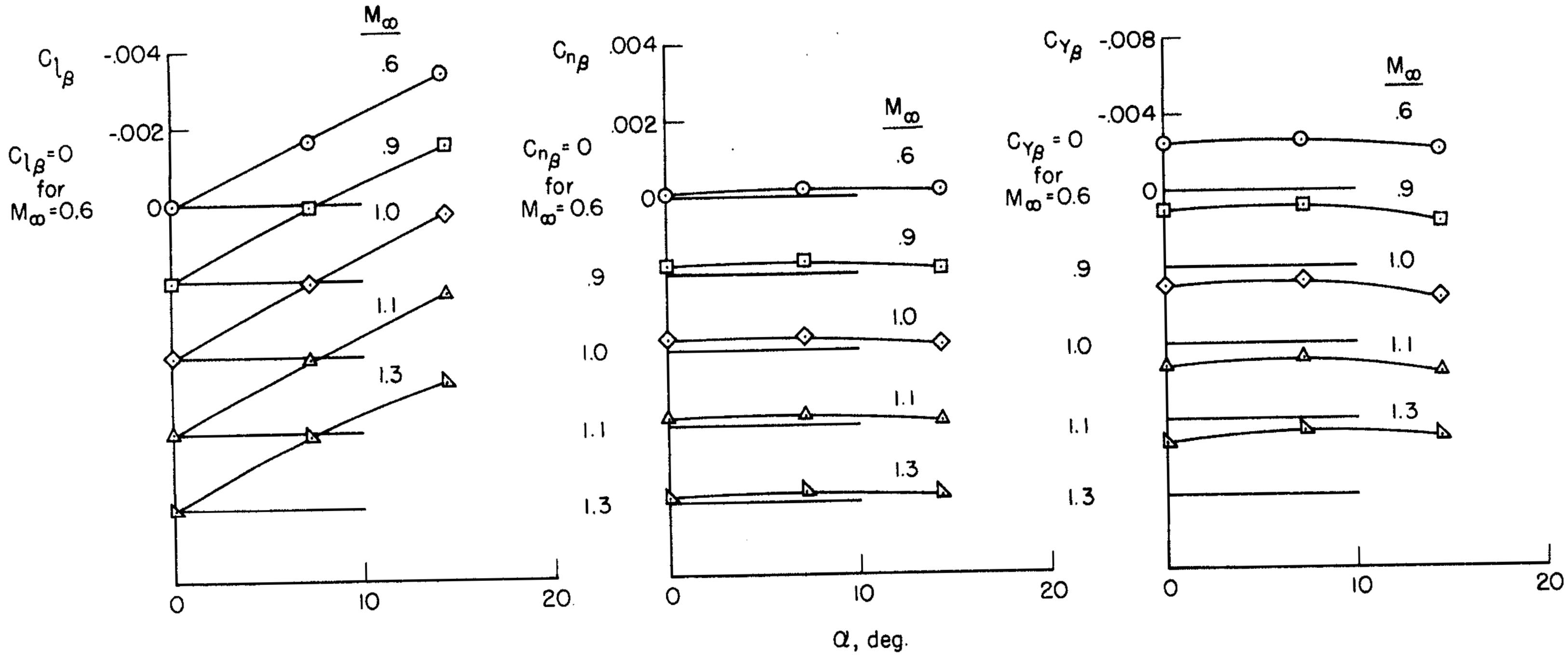

(d) Lateral stability derivatives.

Figure 9.- Concluded.

[redacted]

[redacted]

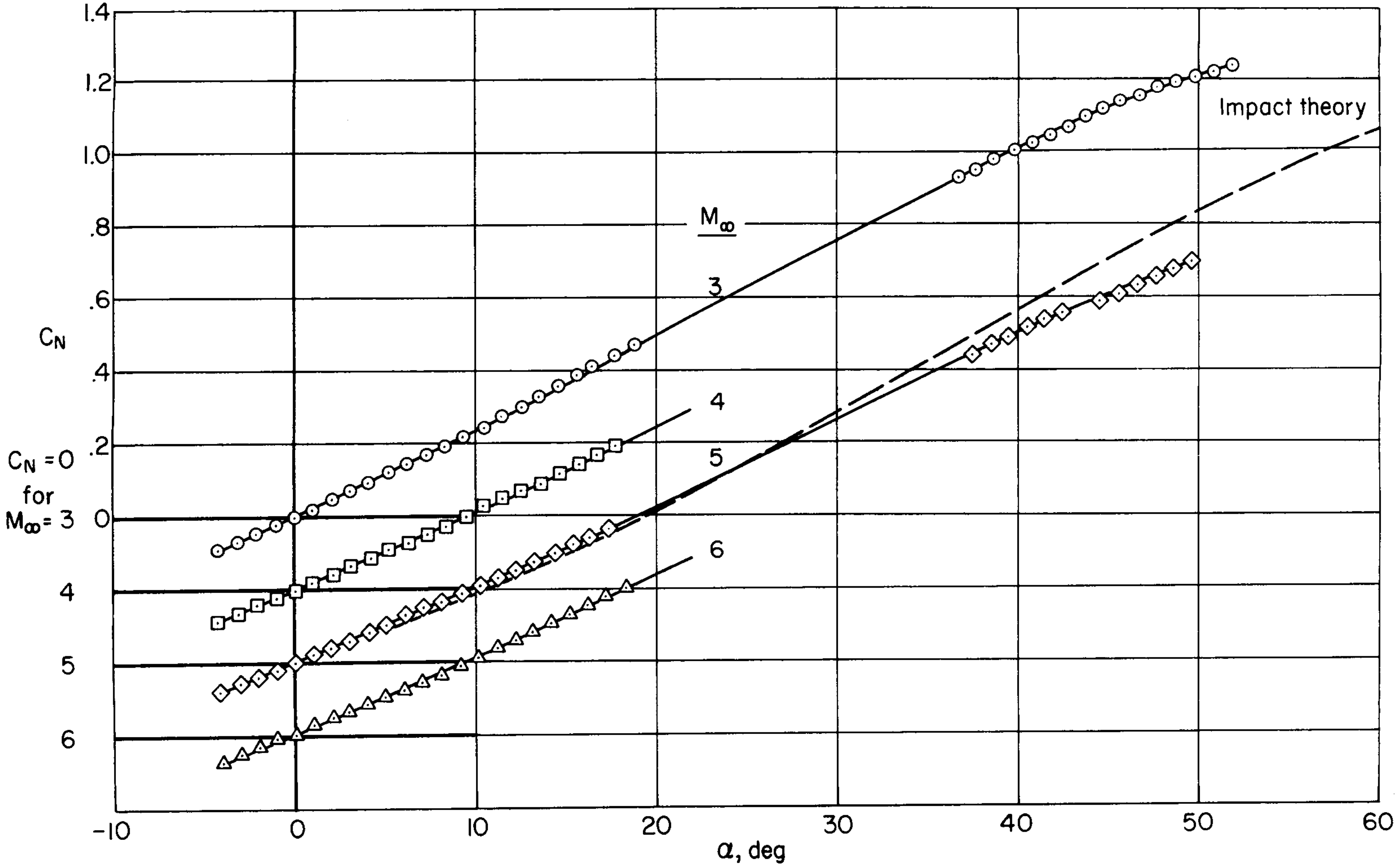

(a) Normal force

Figure 10.- Aerodynamic characteristics of model 1; M_∞ = 3 to 6.

[redacted]

A
2
5
9

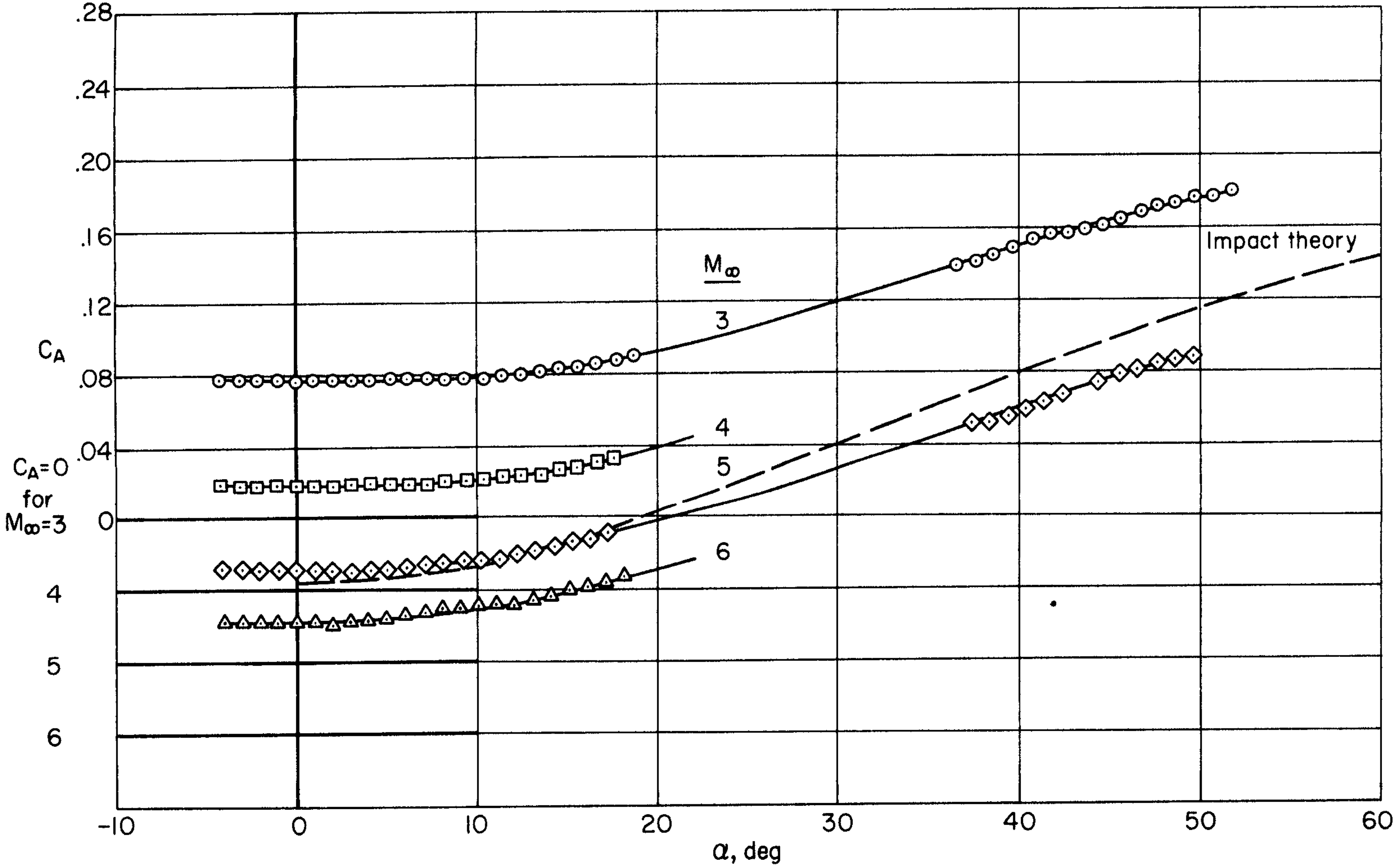

(b) Axial force

Figure 10.- Continued.

[redacted]

[redacted]

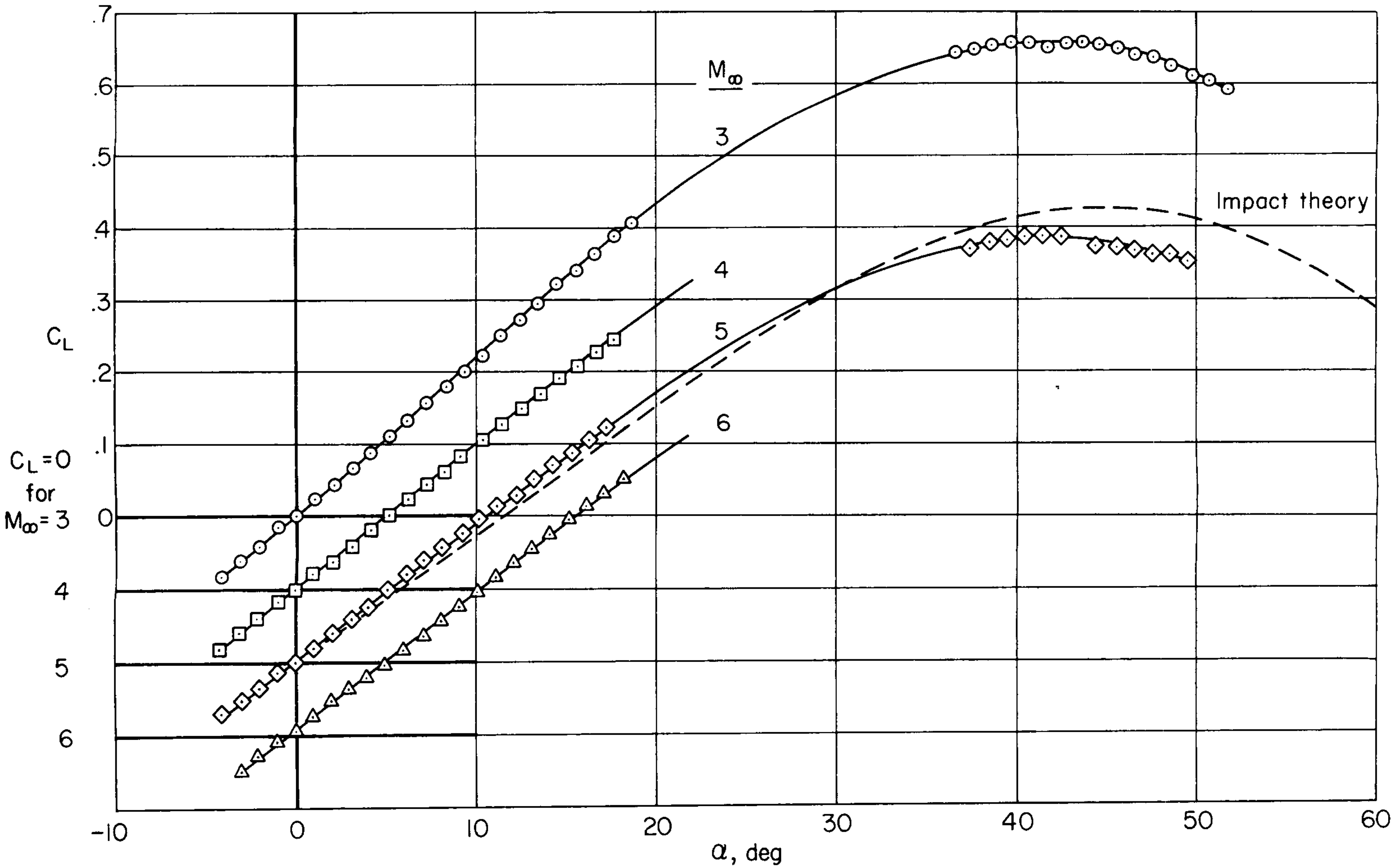

(c) Lift

Figure 10.- Continued.

A
2
5
9
9

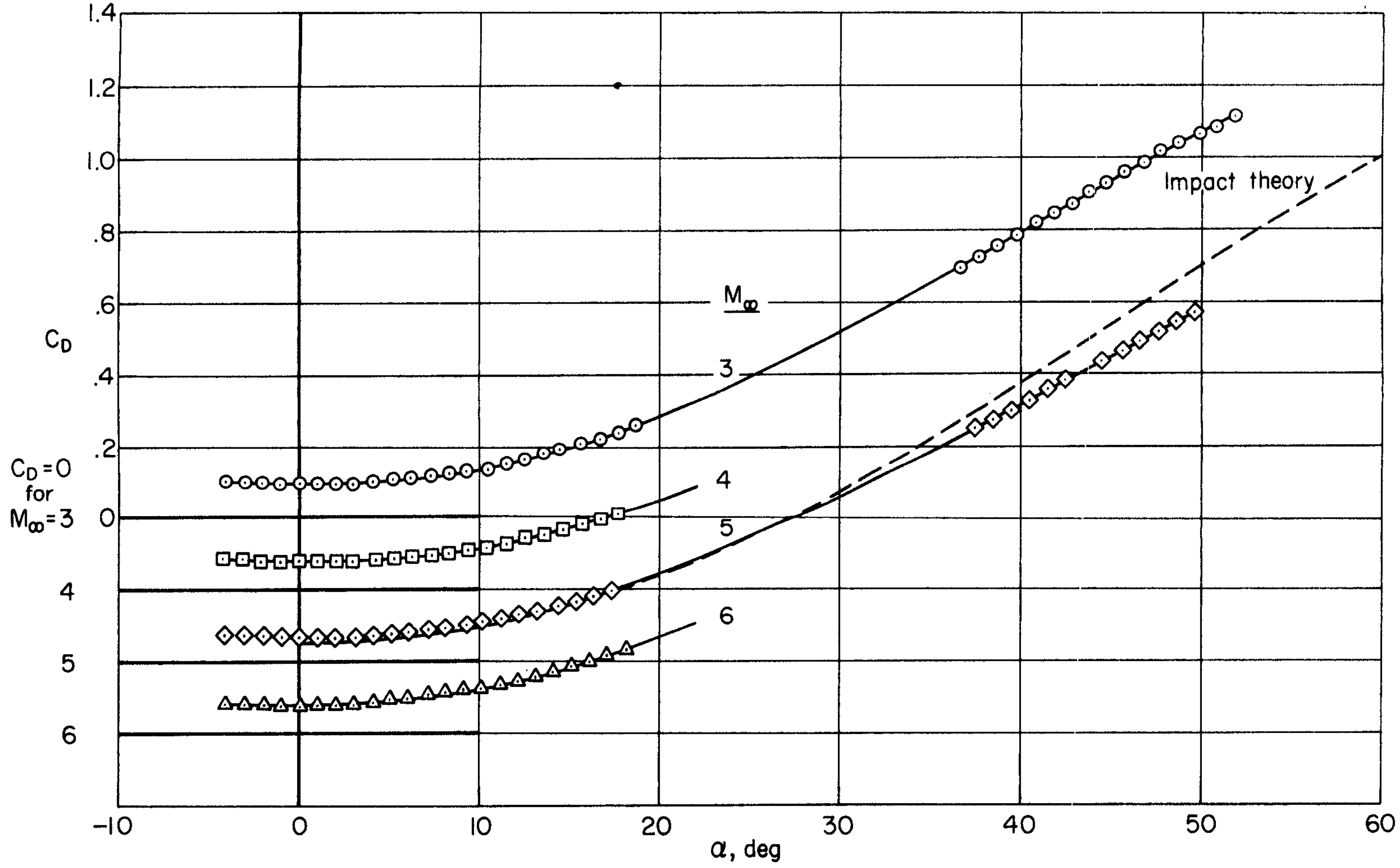

(d) Drag.

Figure 10.- Continued.

[redacted]

[redacted]

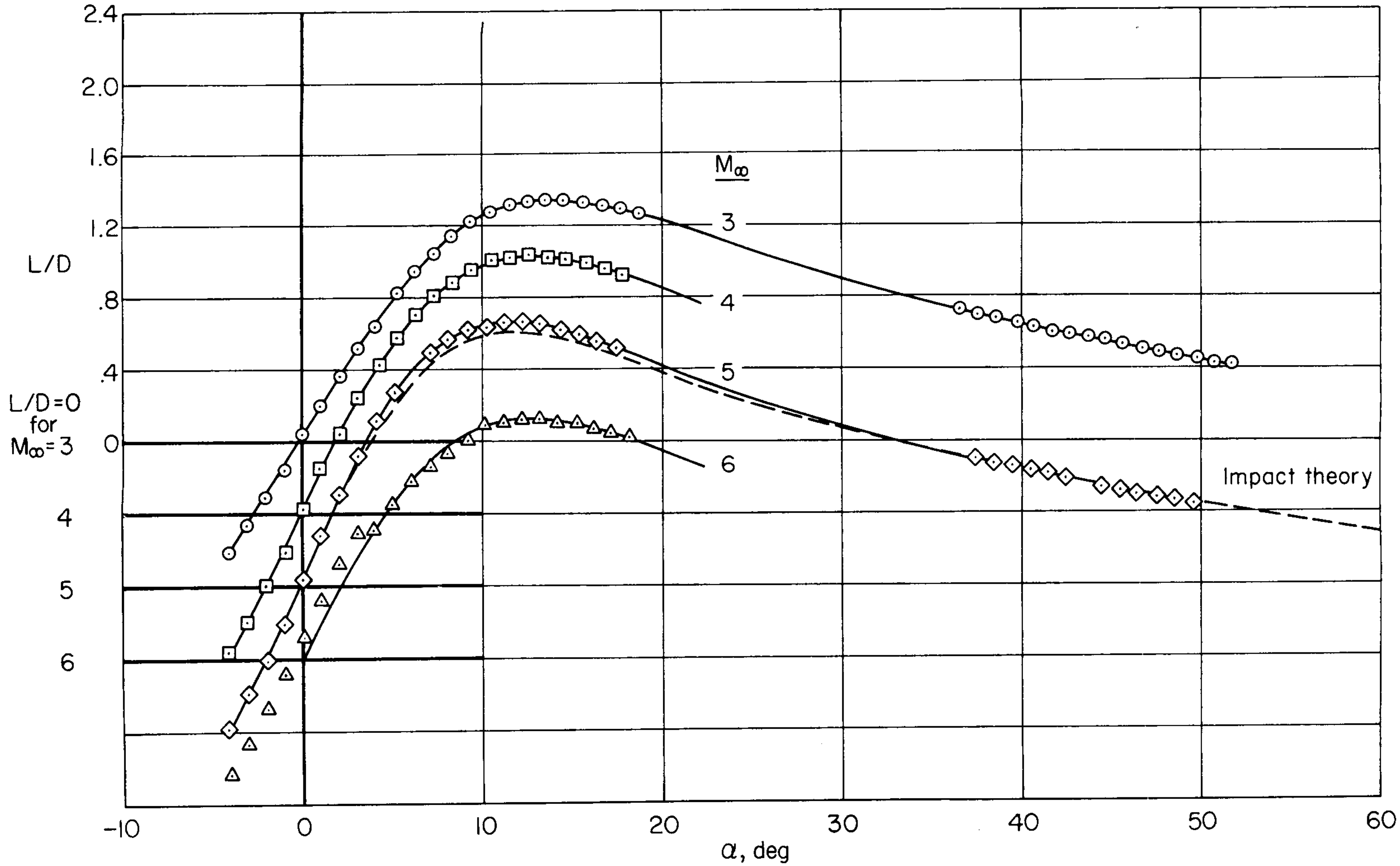

(e) Lift-drag ratio

Figure 10.- Continued.

[redacted]

A
2
5
9

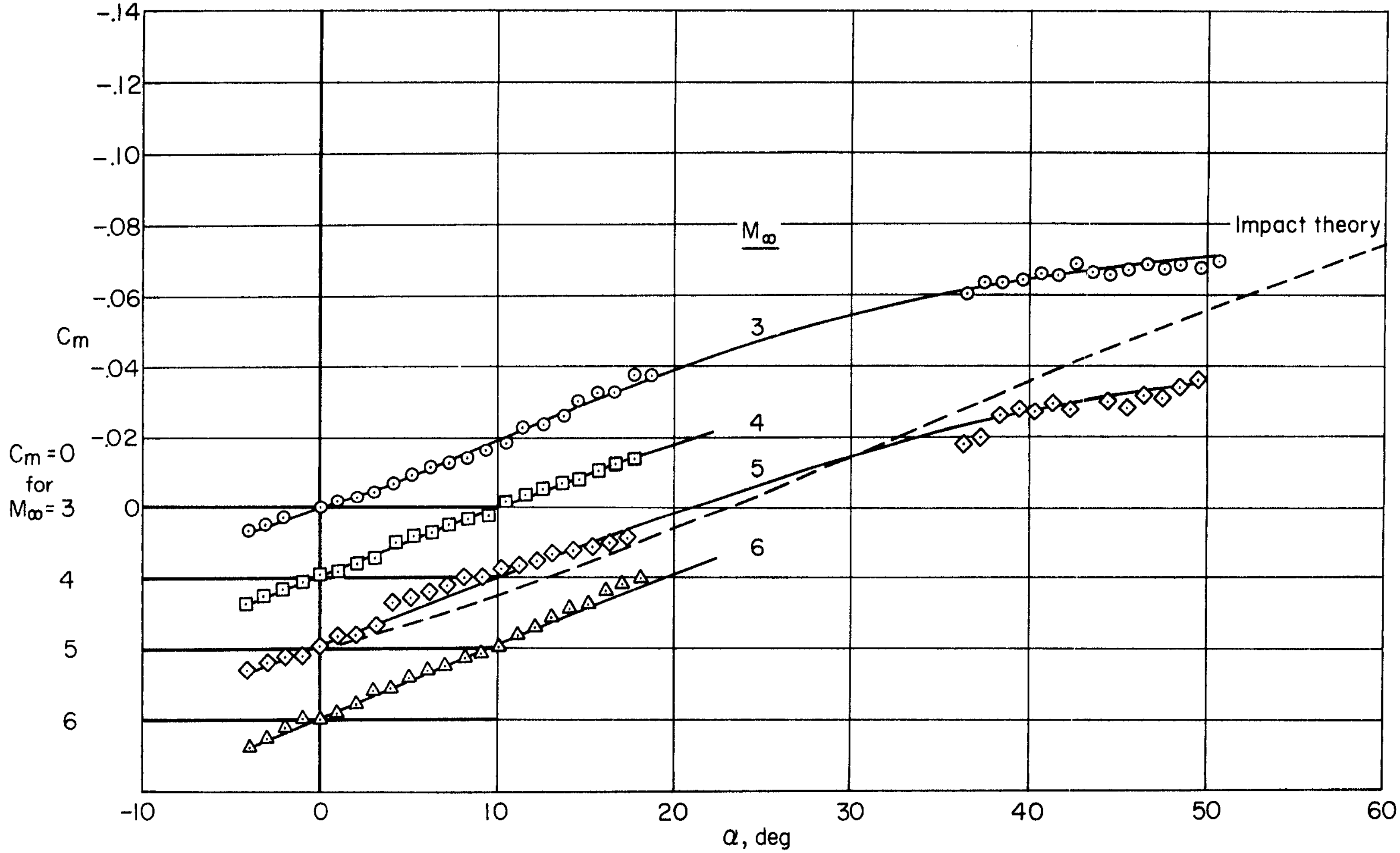

(f) Pitching moment

Figure 10.- Continued.

[redacted]

[redacted]

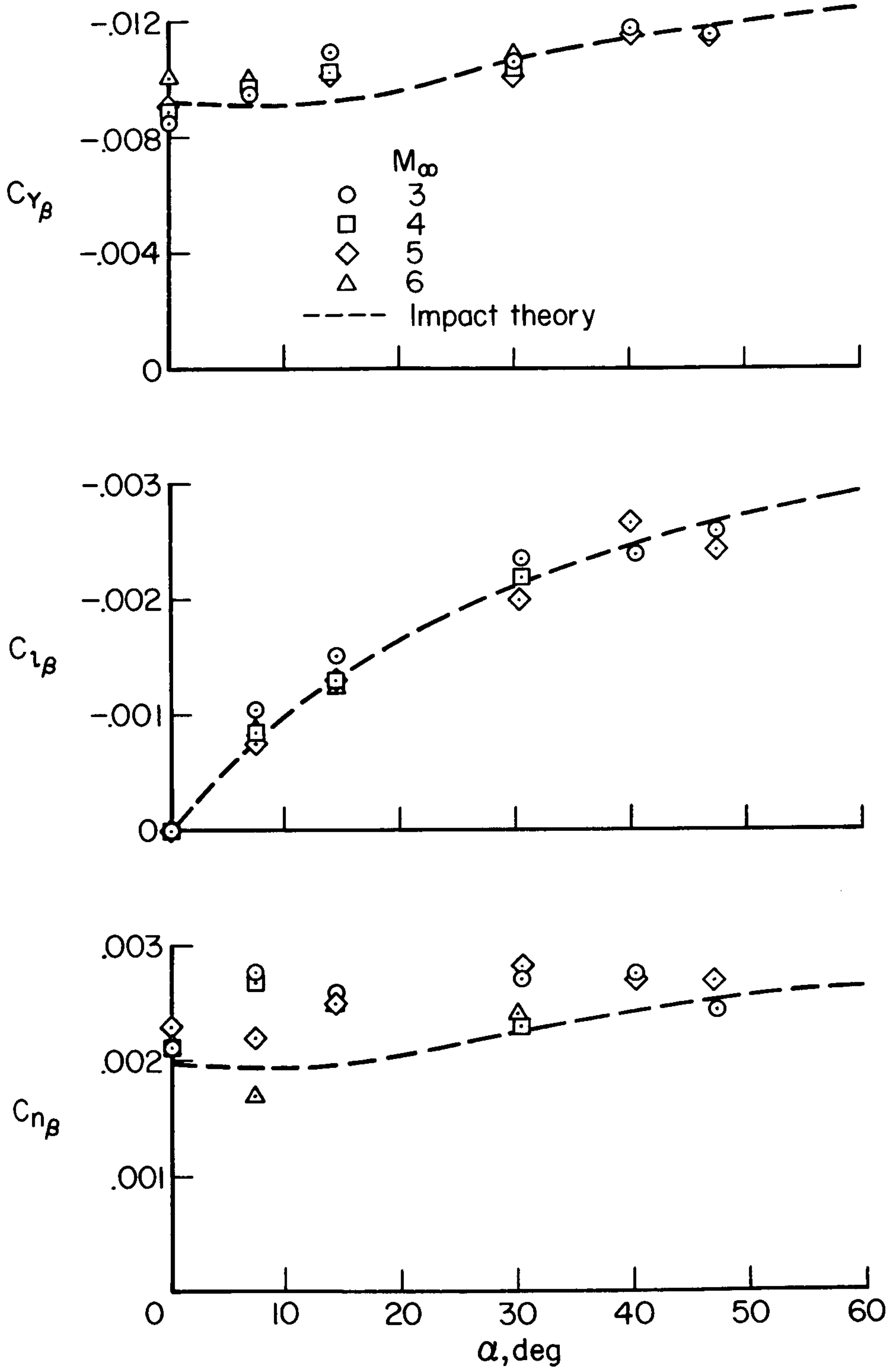

(g) Lateral stability derivatives.

Figure 10.- Concluded.

[redacted]

[redacted]

[redacted]

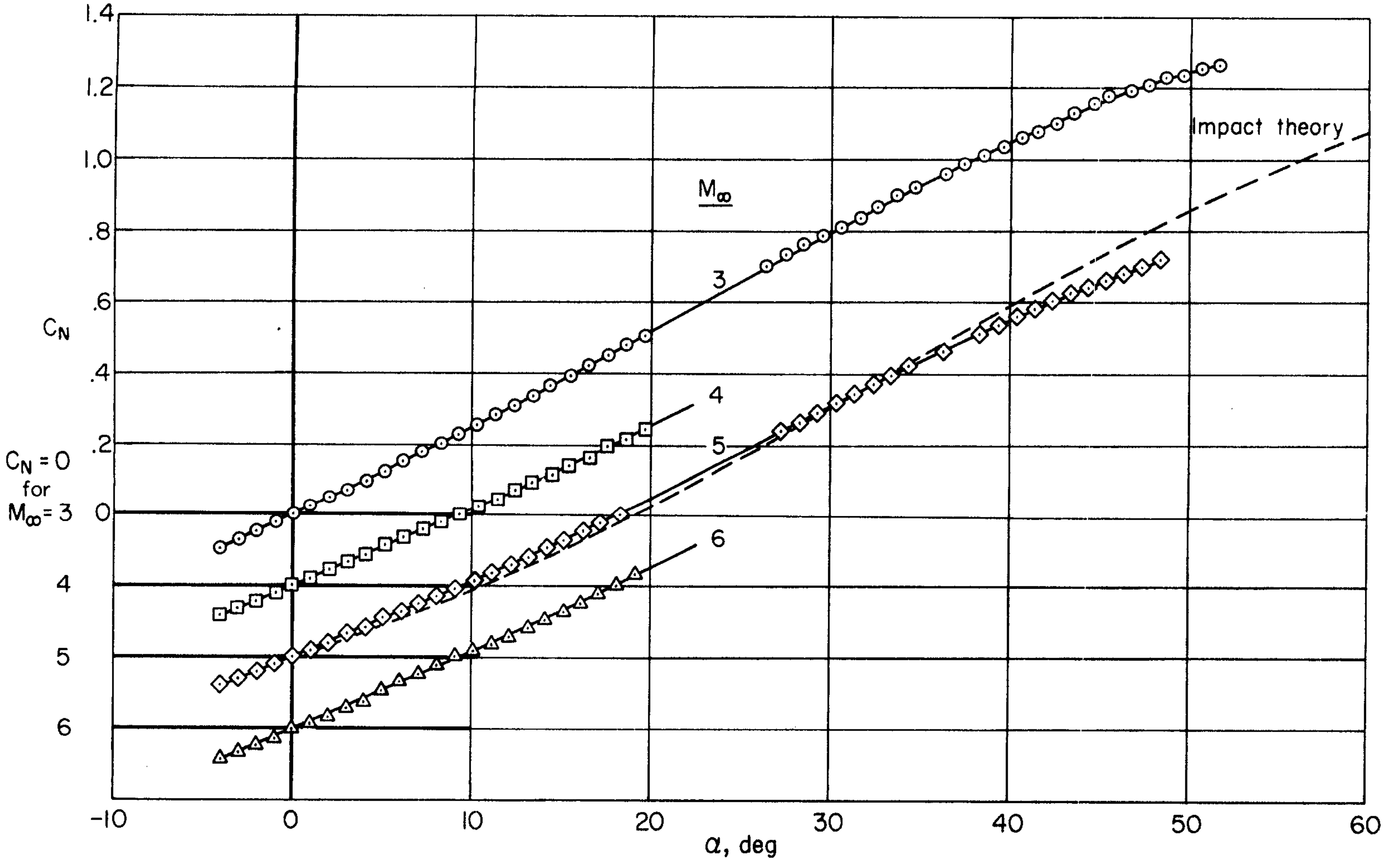

(a) Normal force

Figure 11.- Aerodynamic characteristics of model 2; $M_\infty = 3$ to 6.

[redacted]

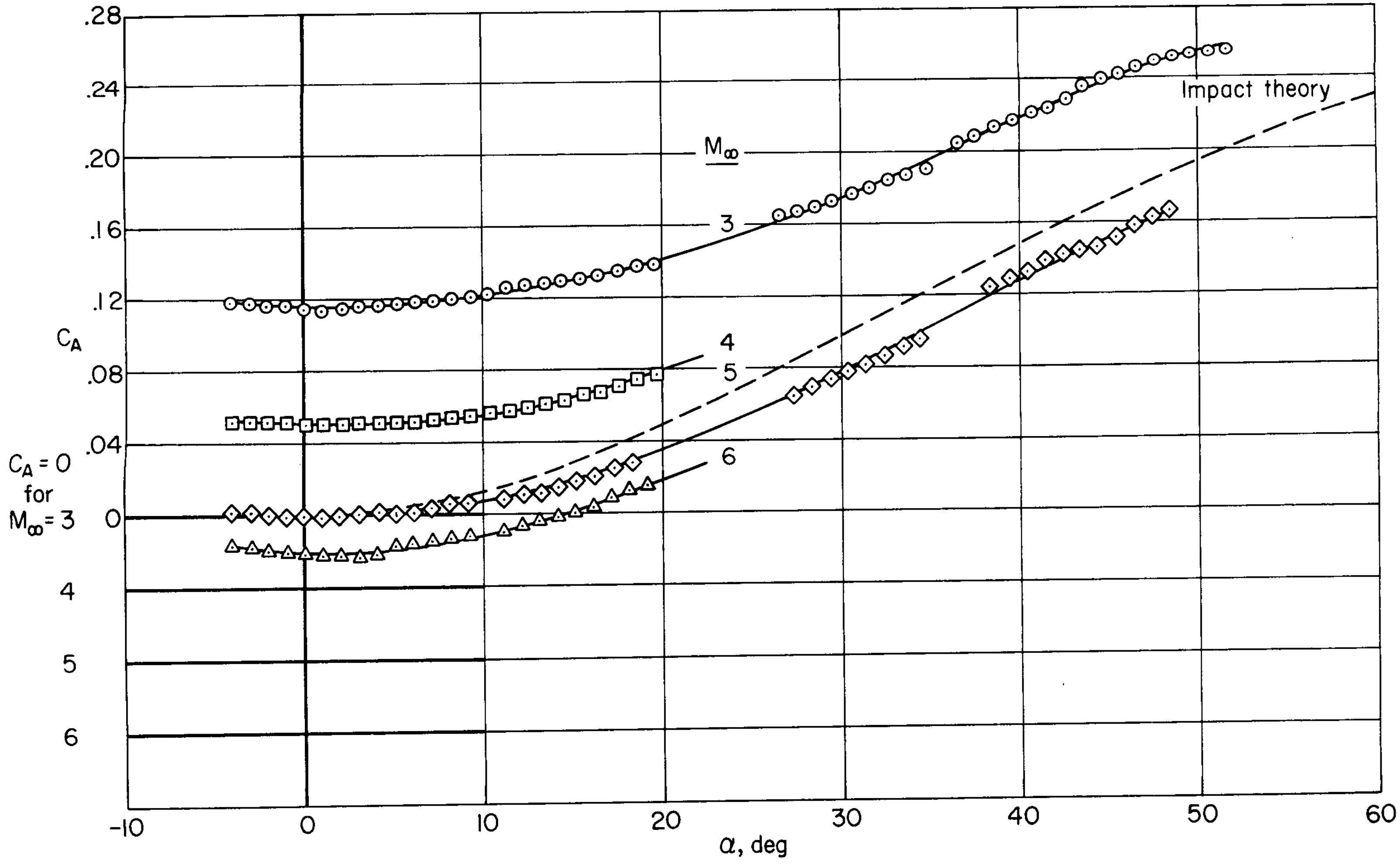

(b) Axial force

Figure 11.- Continued.

[redacted]

[redacted]

A
2
5
9

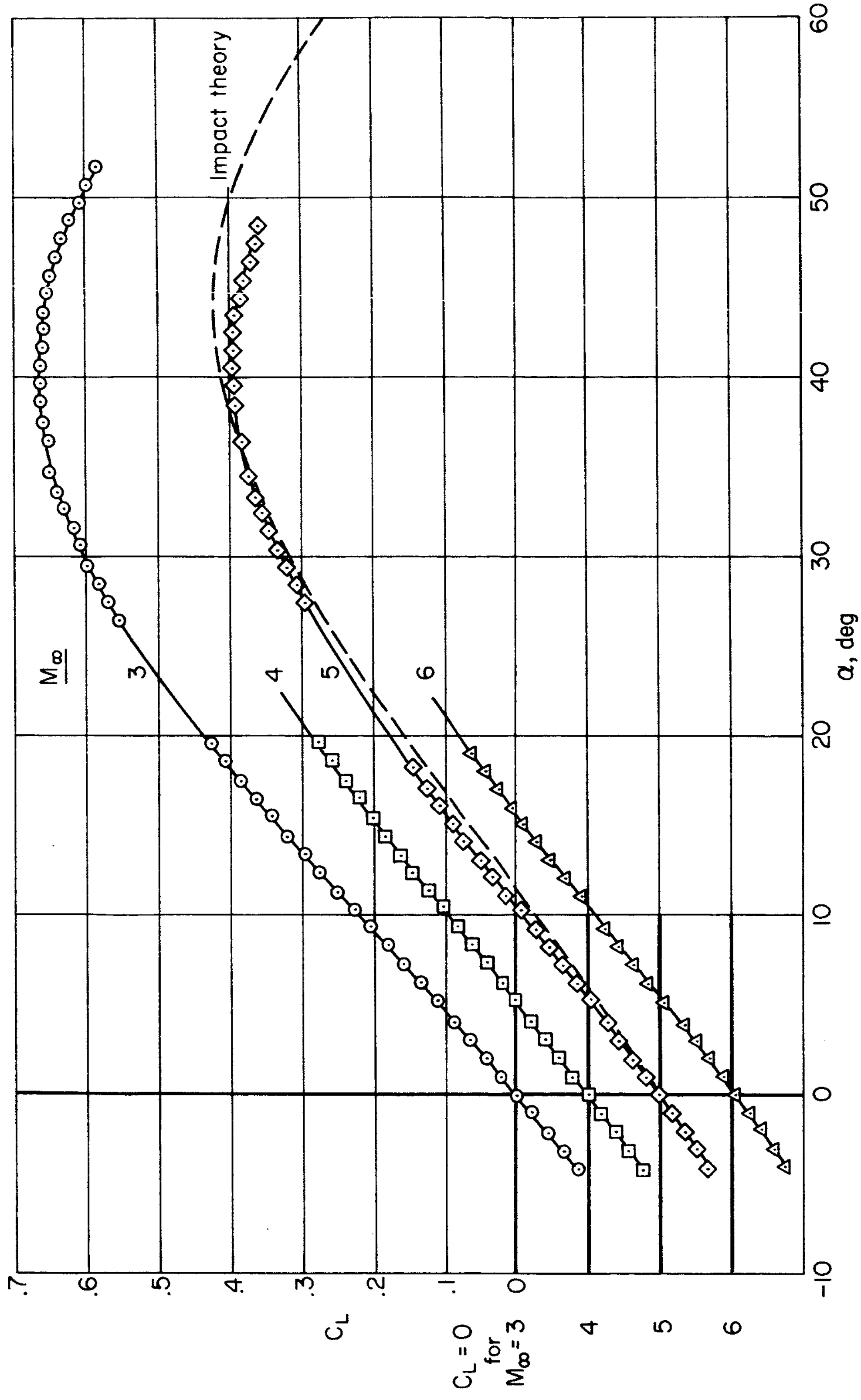

(c) Lift.

Figure 11.- Continued.

[redacted]

[redacted]

[redacted]

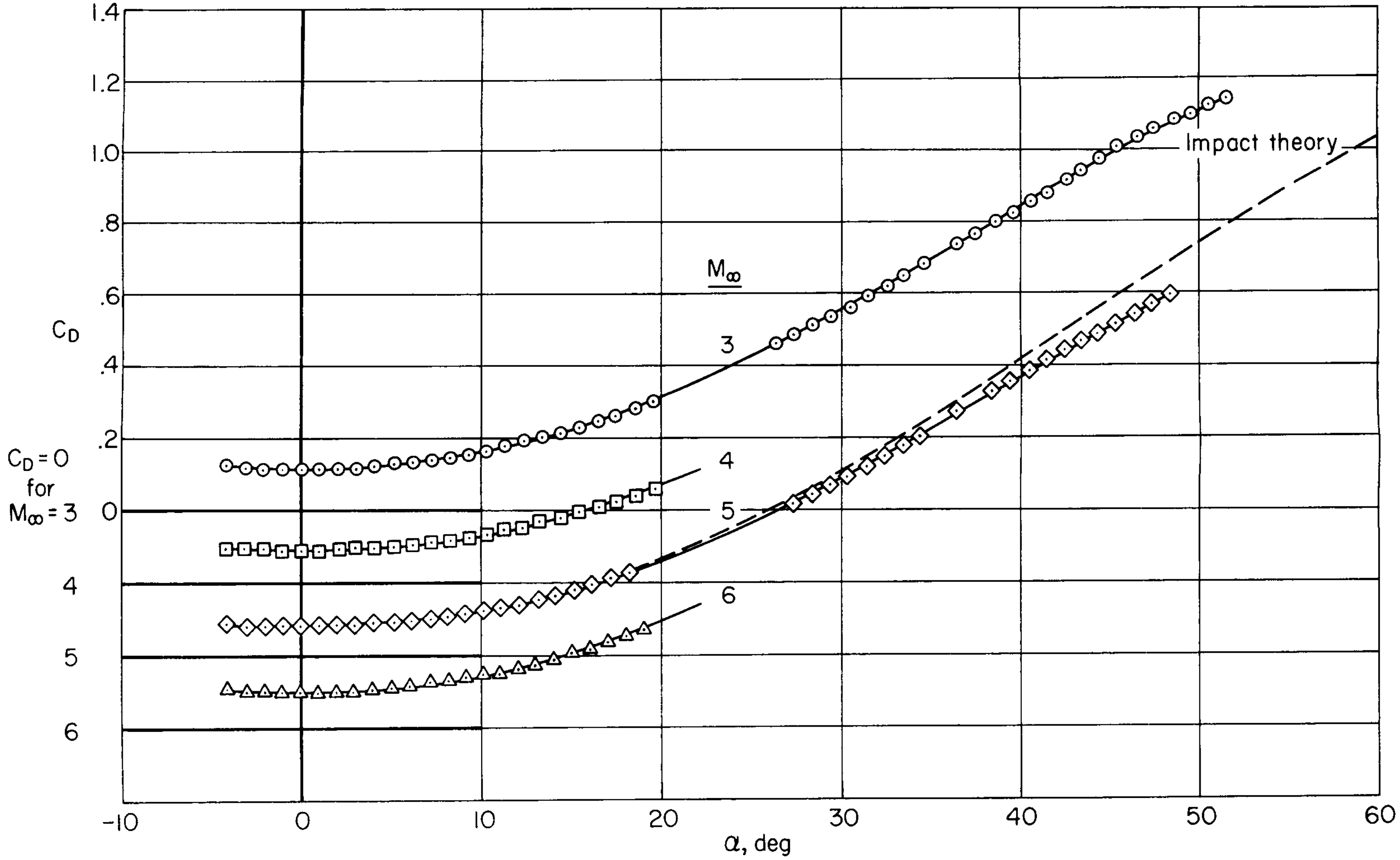

(d) Drag

Figure 11.- Continued.

[redacted]

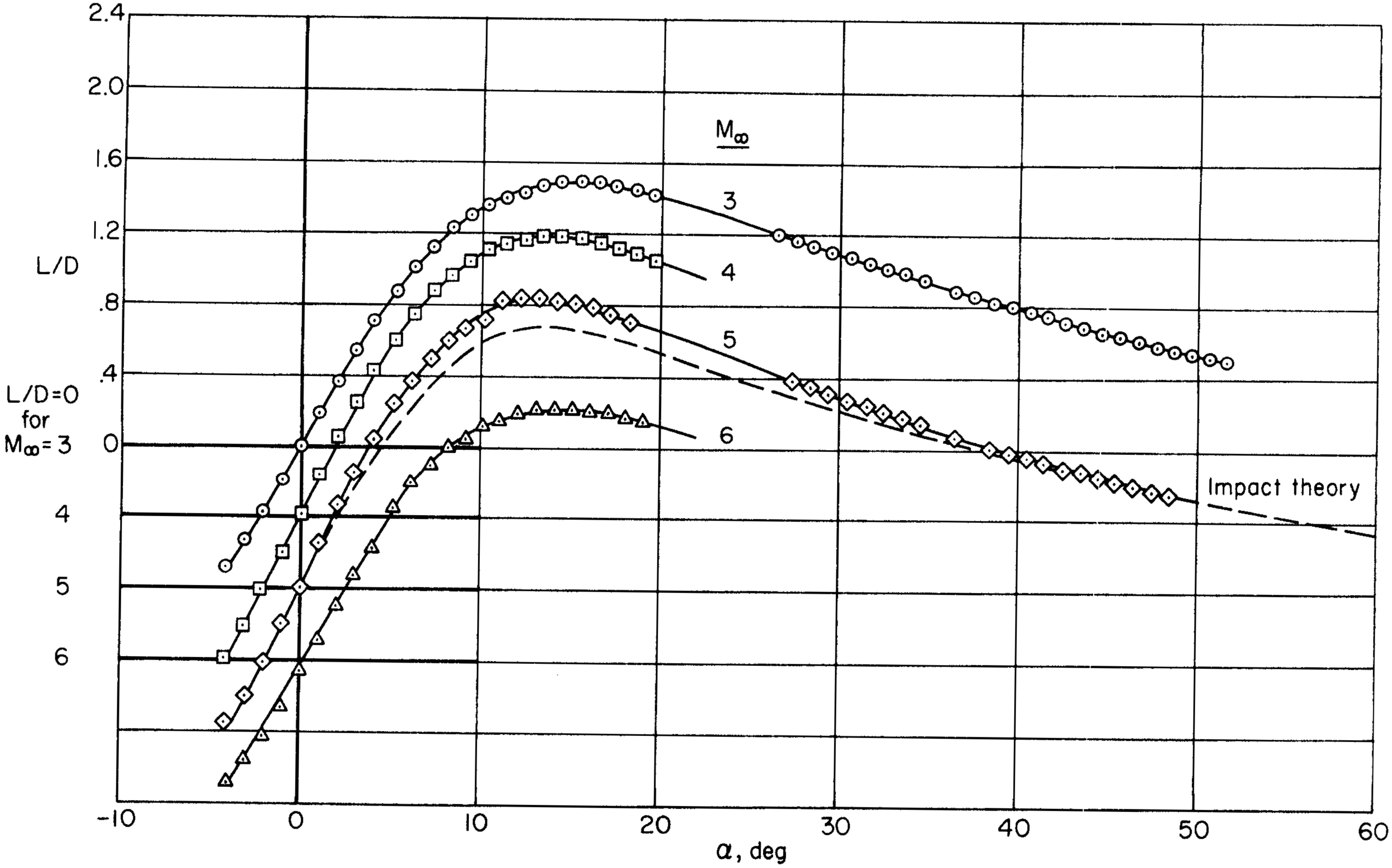

(e) Lift-drag ratio

Figure 11.- Continued.

[redacted]

[redacted]

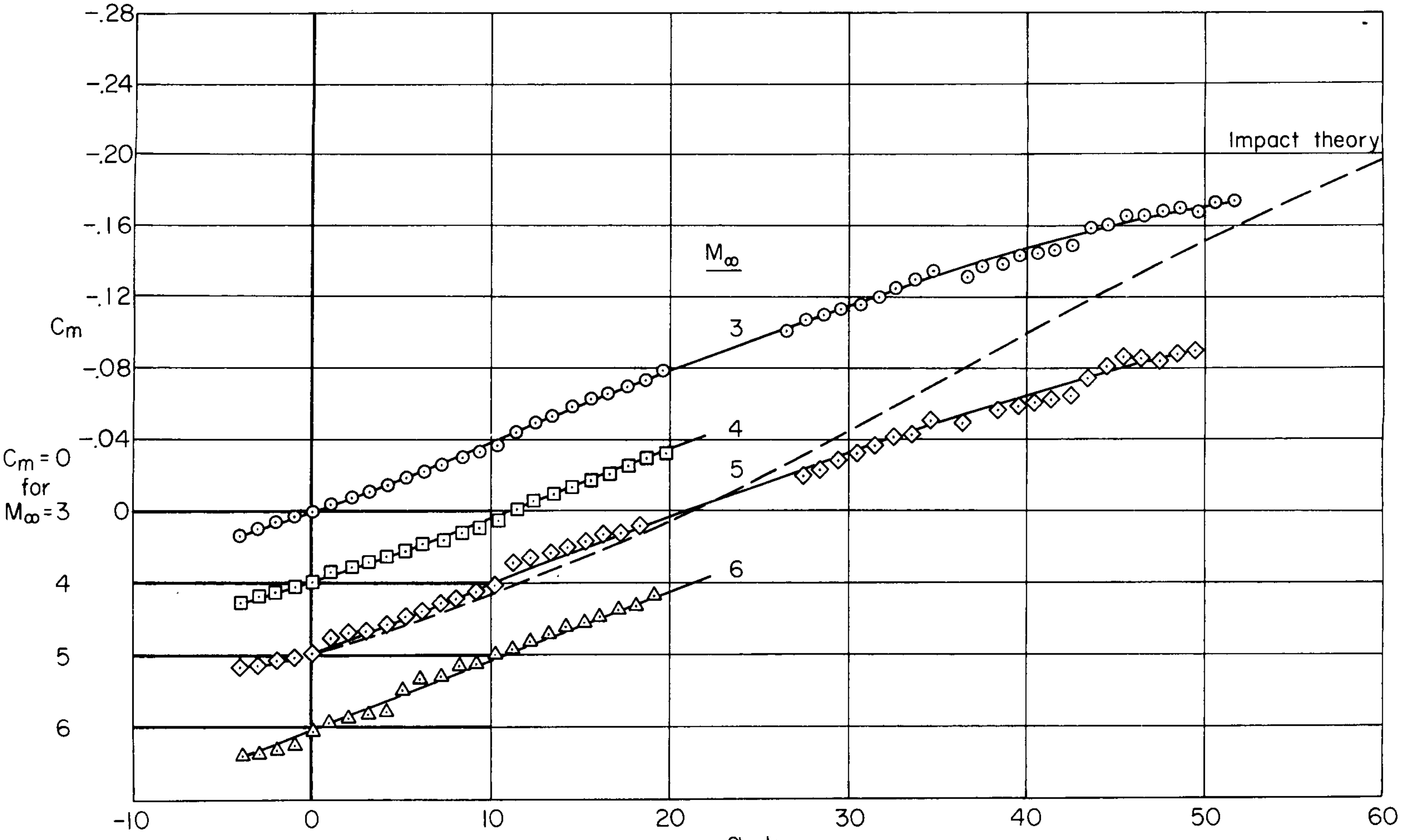

(f) Pitching moment

Figure 11.- Continued.

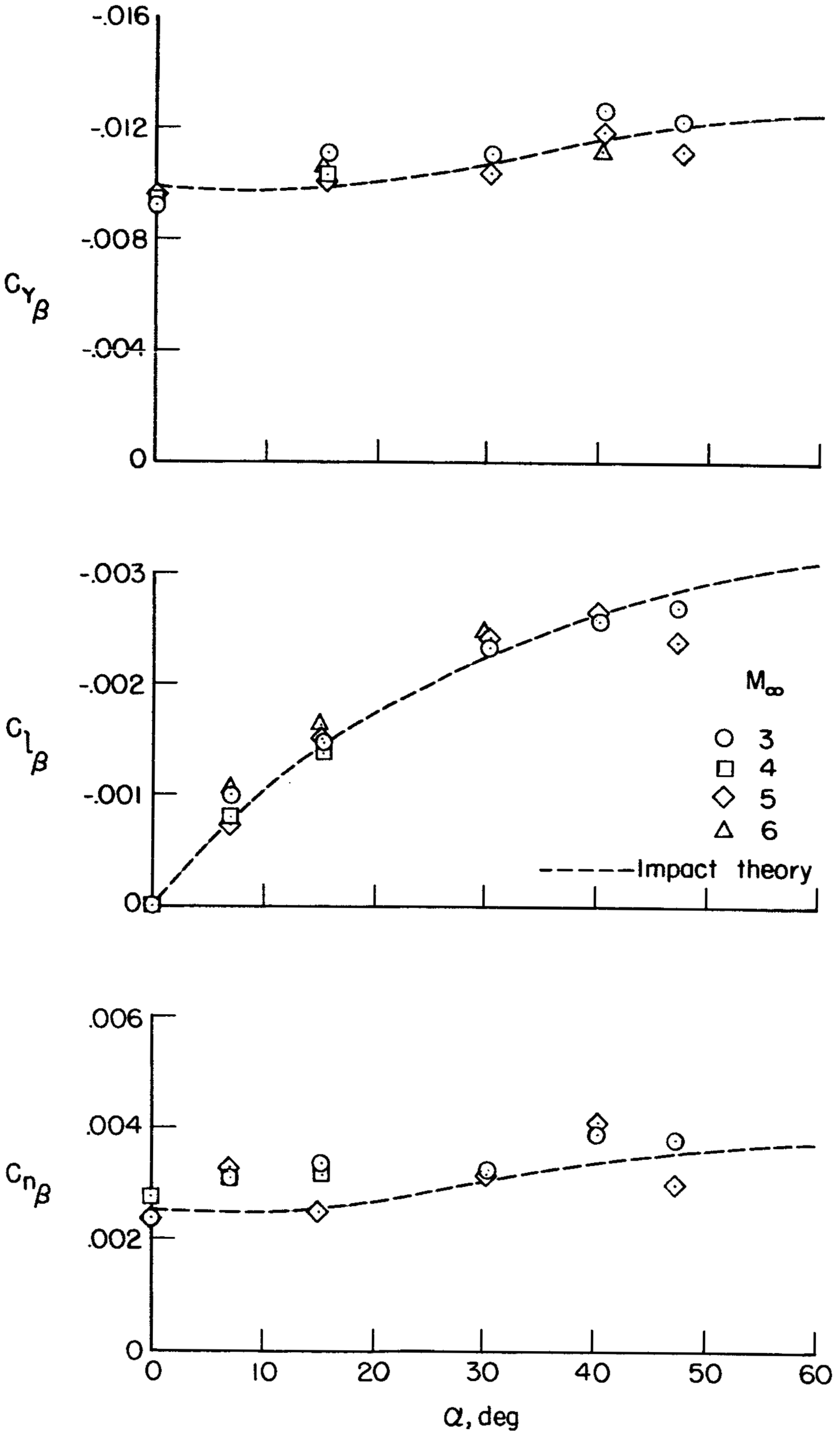

(g) Lateral stability derivatives.

Figure 11.- Concluded.

[redacted]

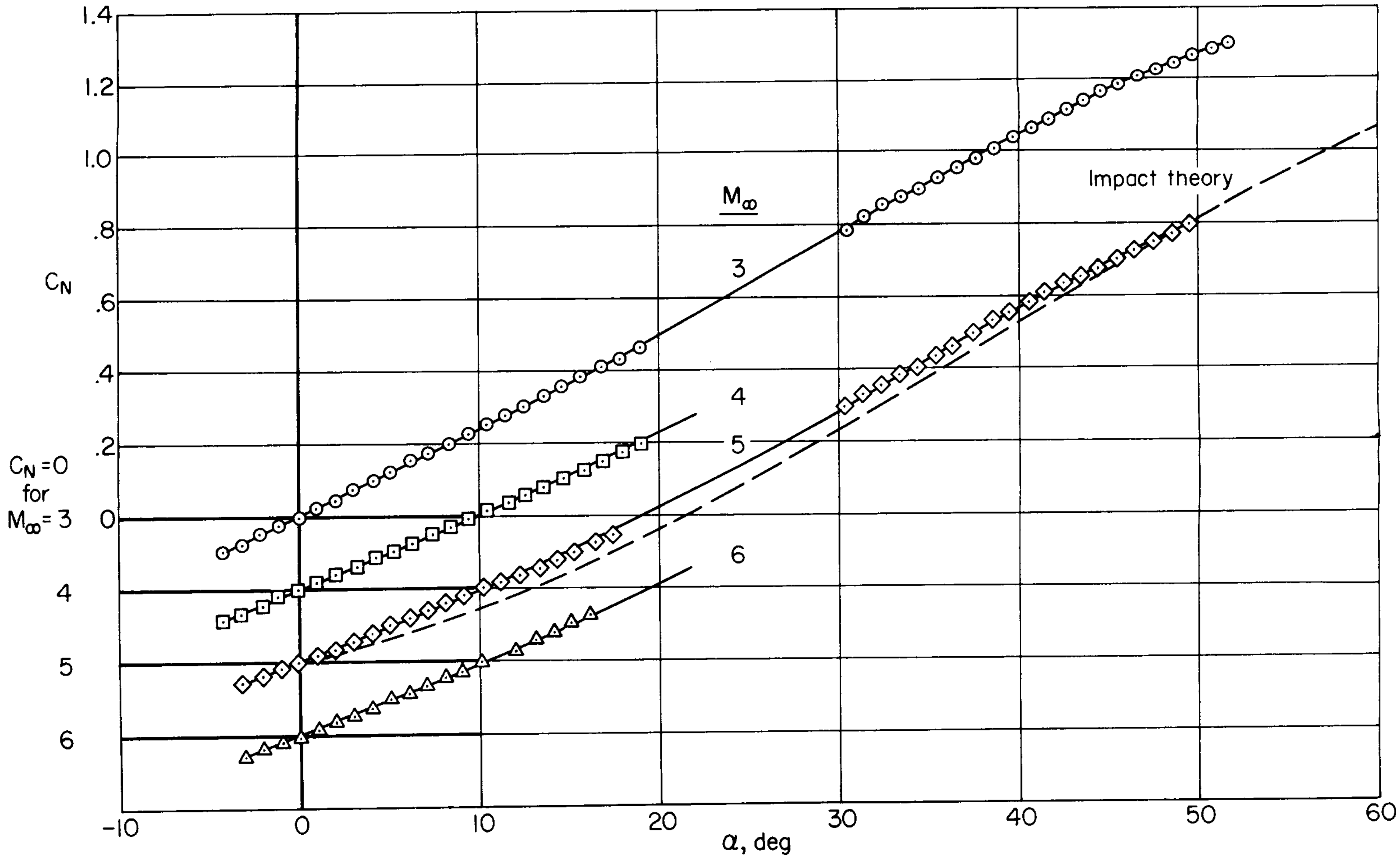

(a) Normal force

Figure 12.- Aerodynamic characteristics of model 3; M_∞ = 3 to 6.

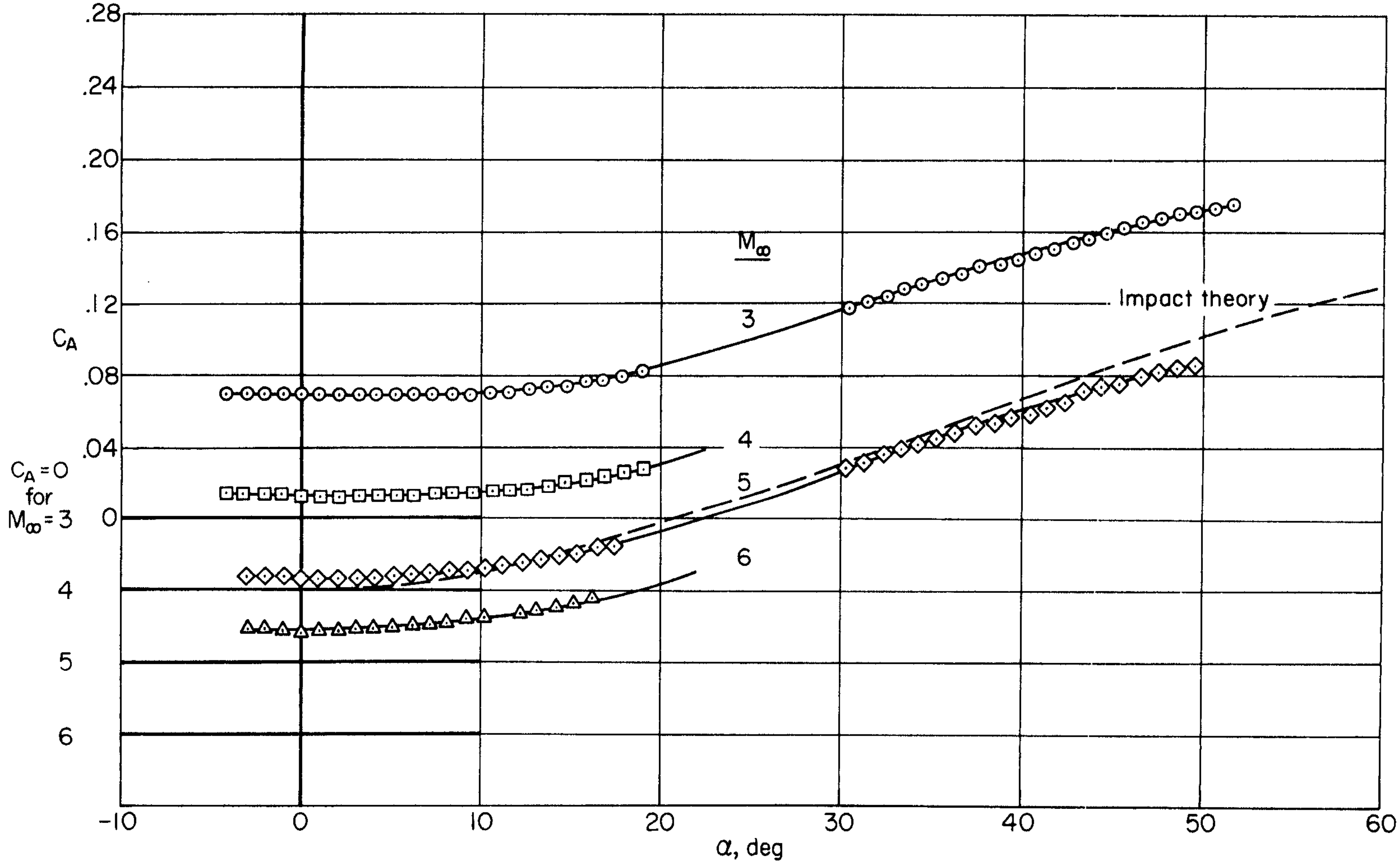

(b) Axial force

Figure 12.- Continued.

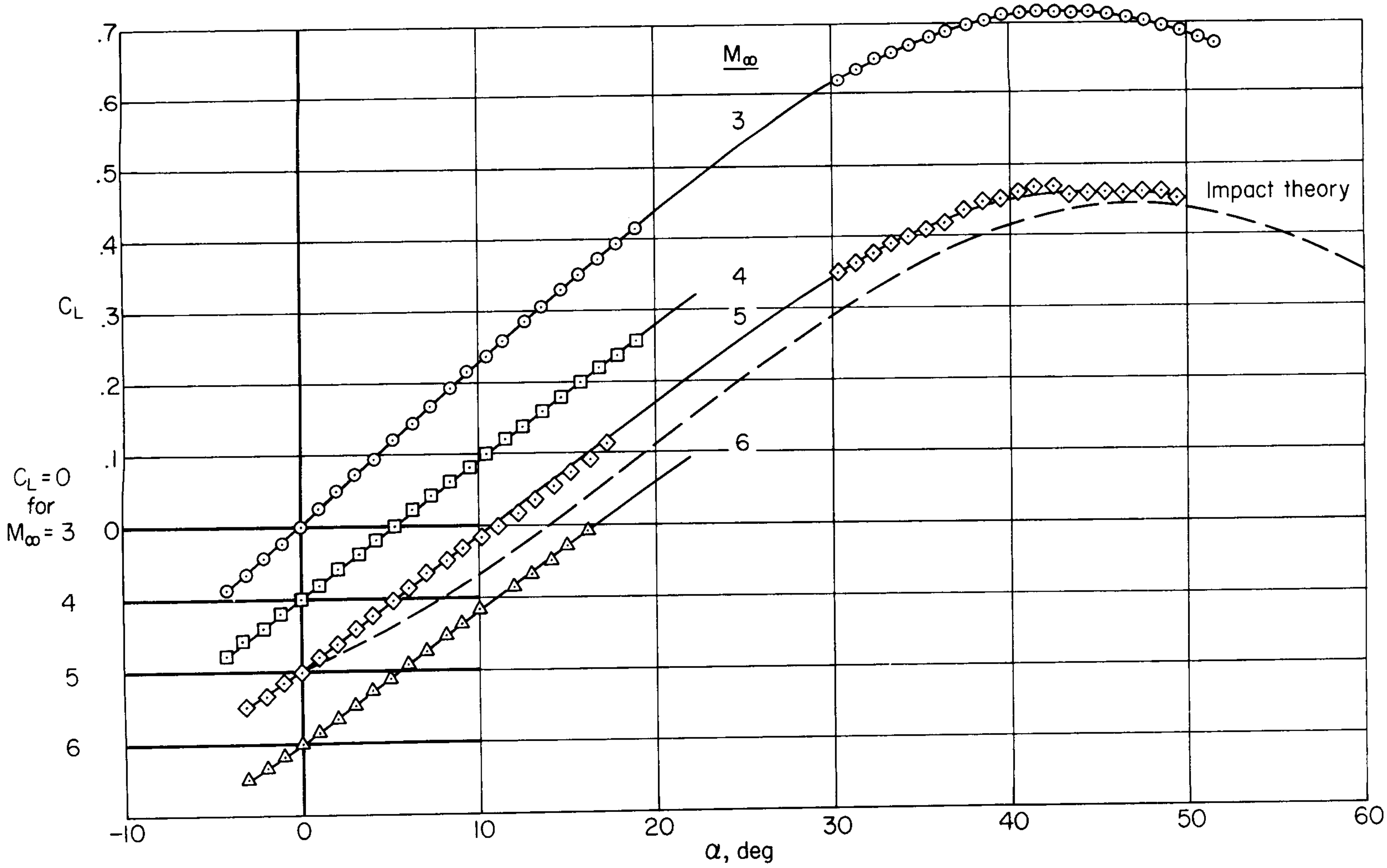

(c) Lift

Figure 12.- Continued.

A259

A
2
5
9

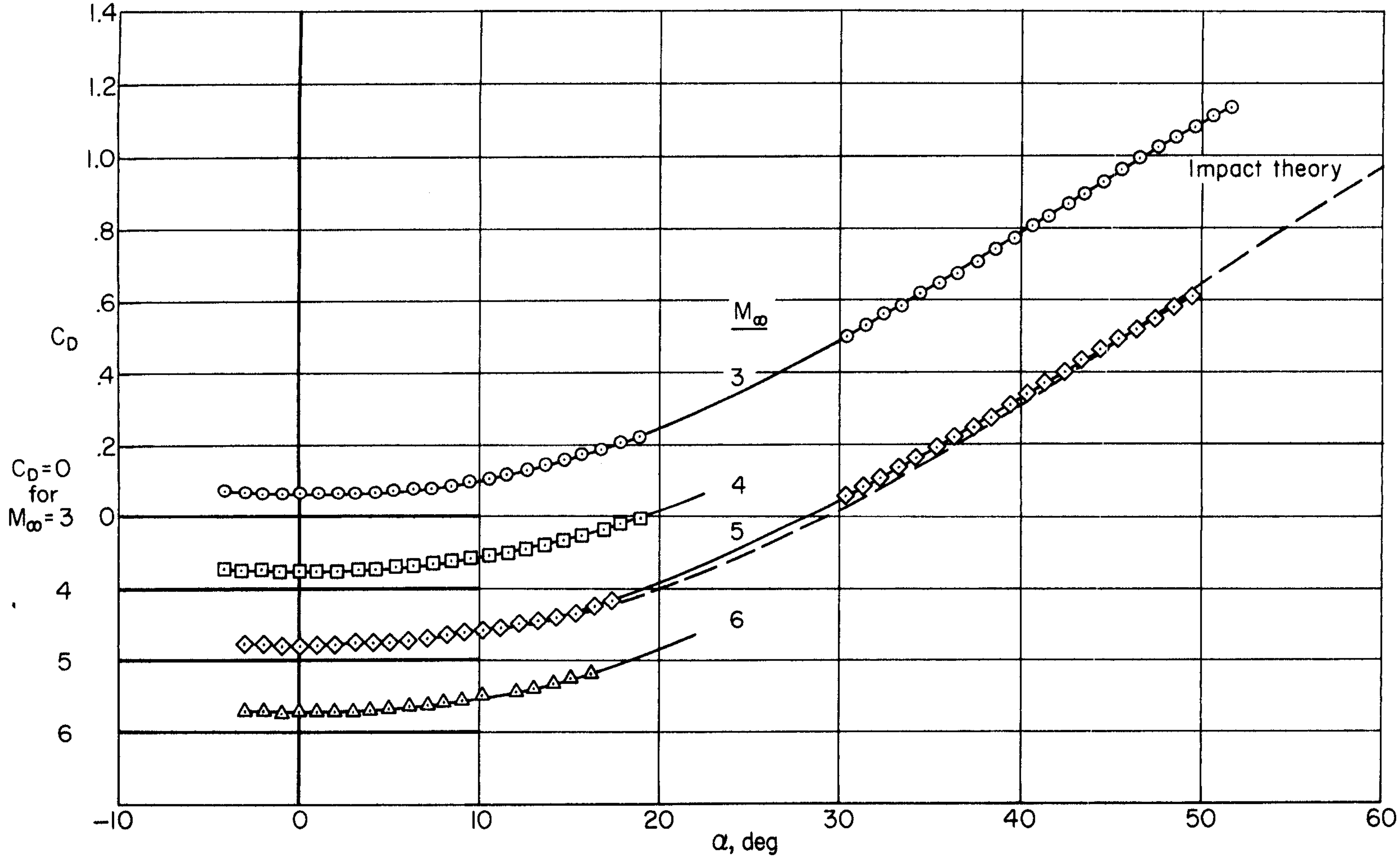

(d) Drag

Figure 12.- Continued.

[redacted]

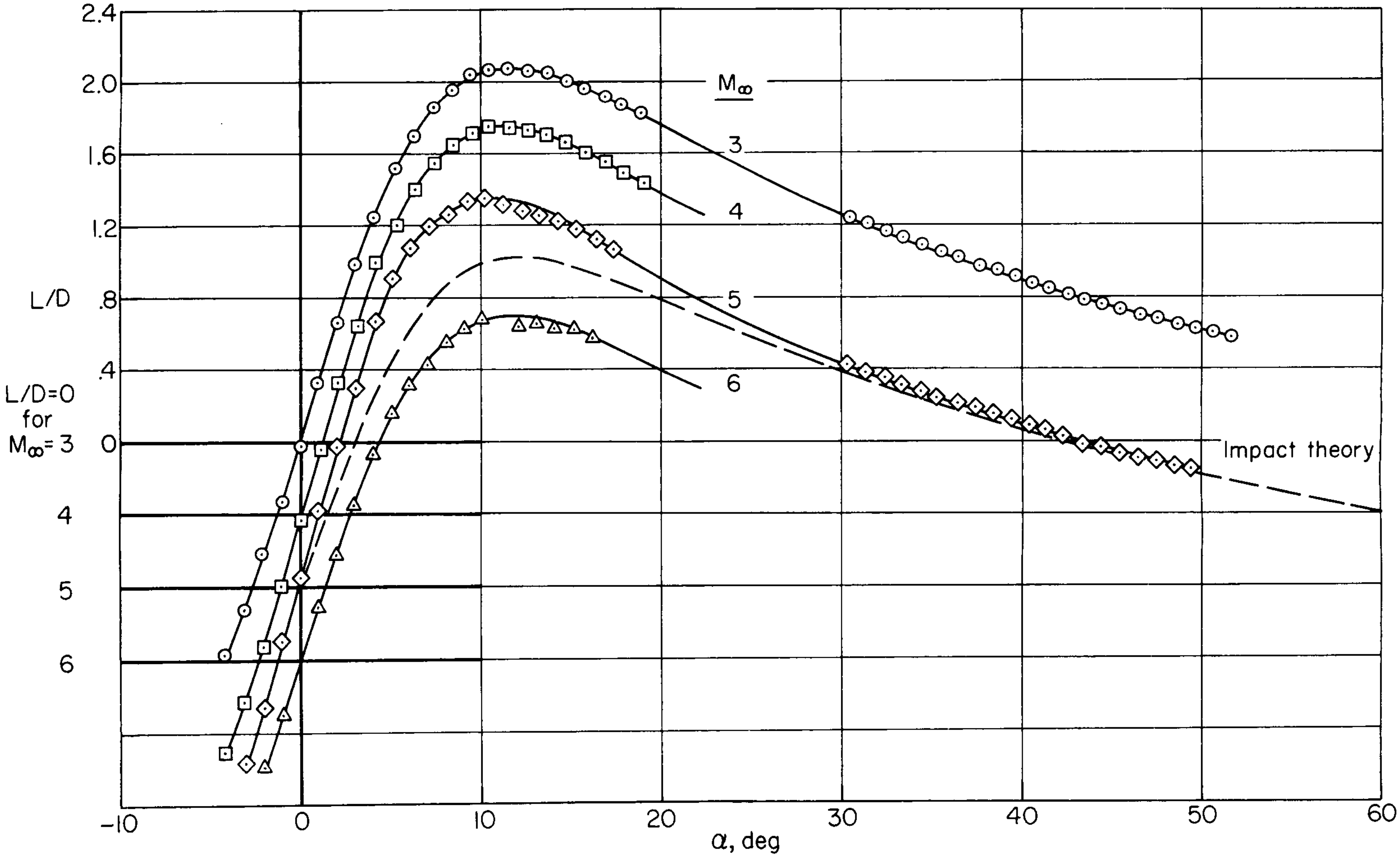

(e) Lift-drag ratio

Figure 12.- Continued.

[redacted]

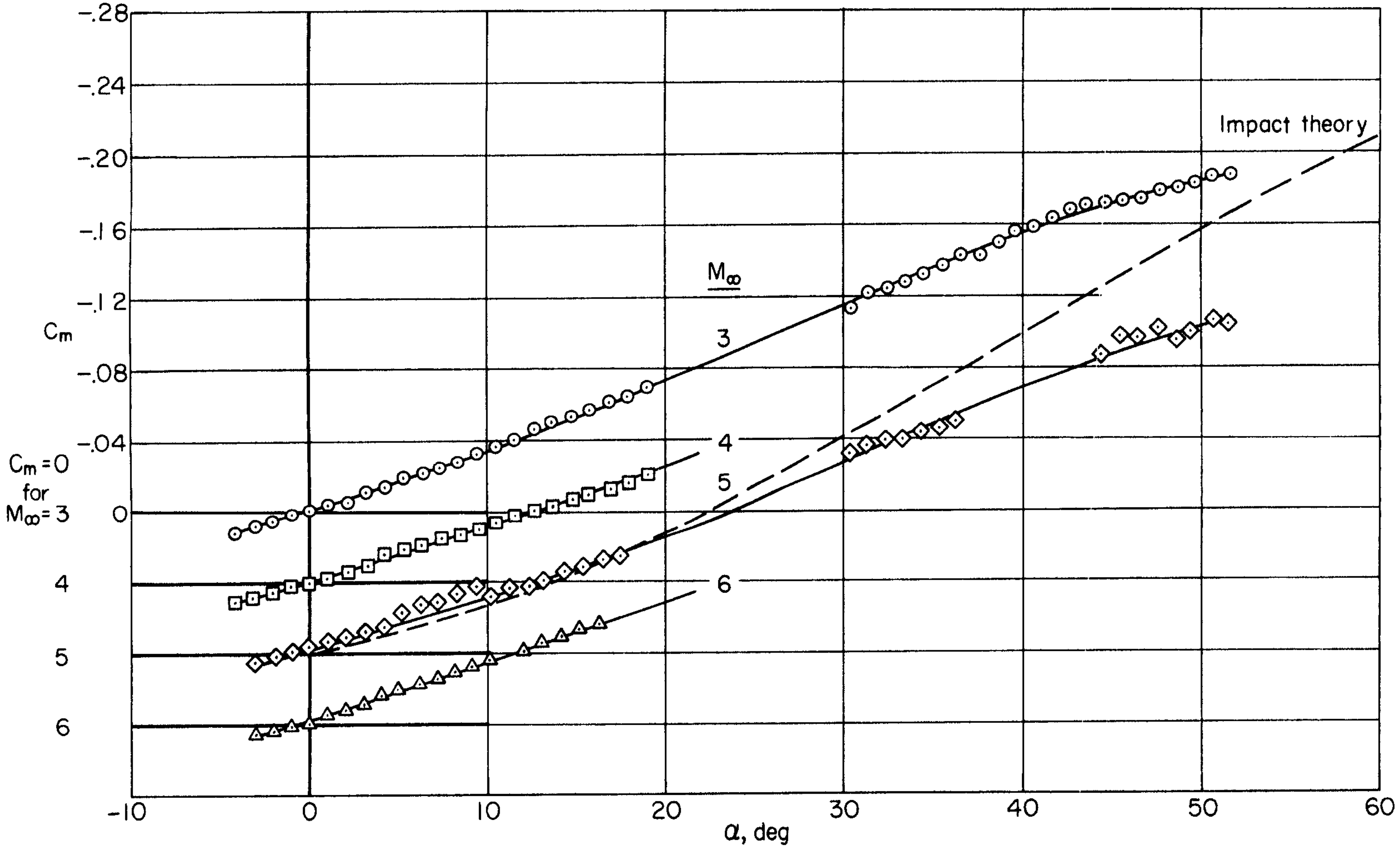

(f) Pitching moment

Figure 12.- Continued.

[redacted]

[redacted]

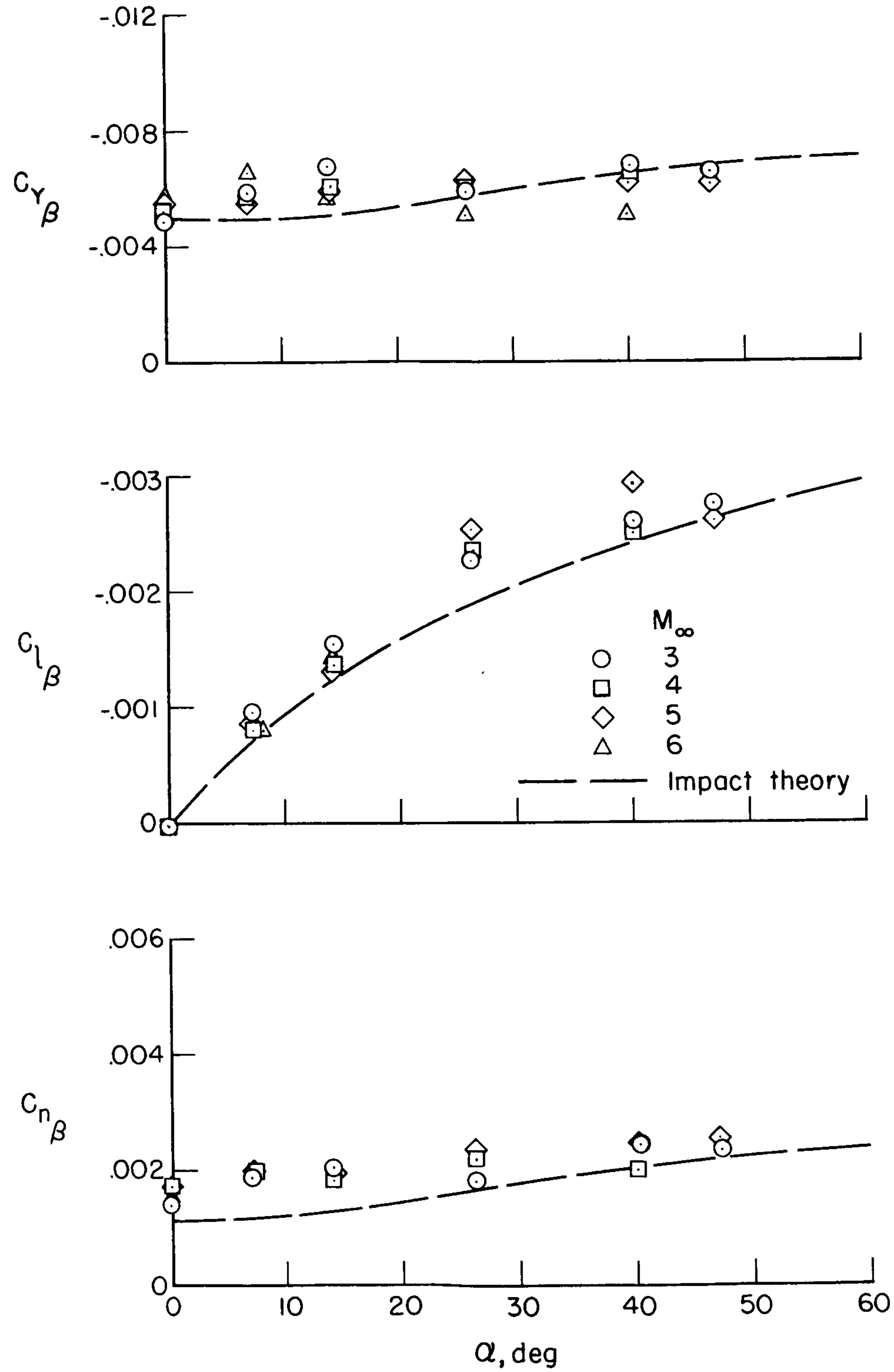

(g) Lateral stability derivatives.

Figure 12.- Concluded.

[redacted]

[redacted]

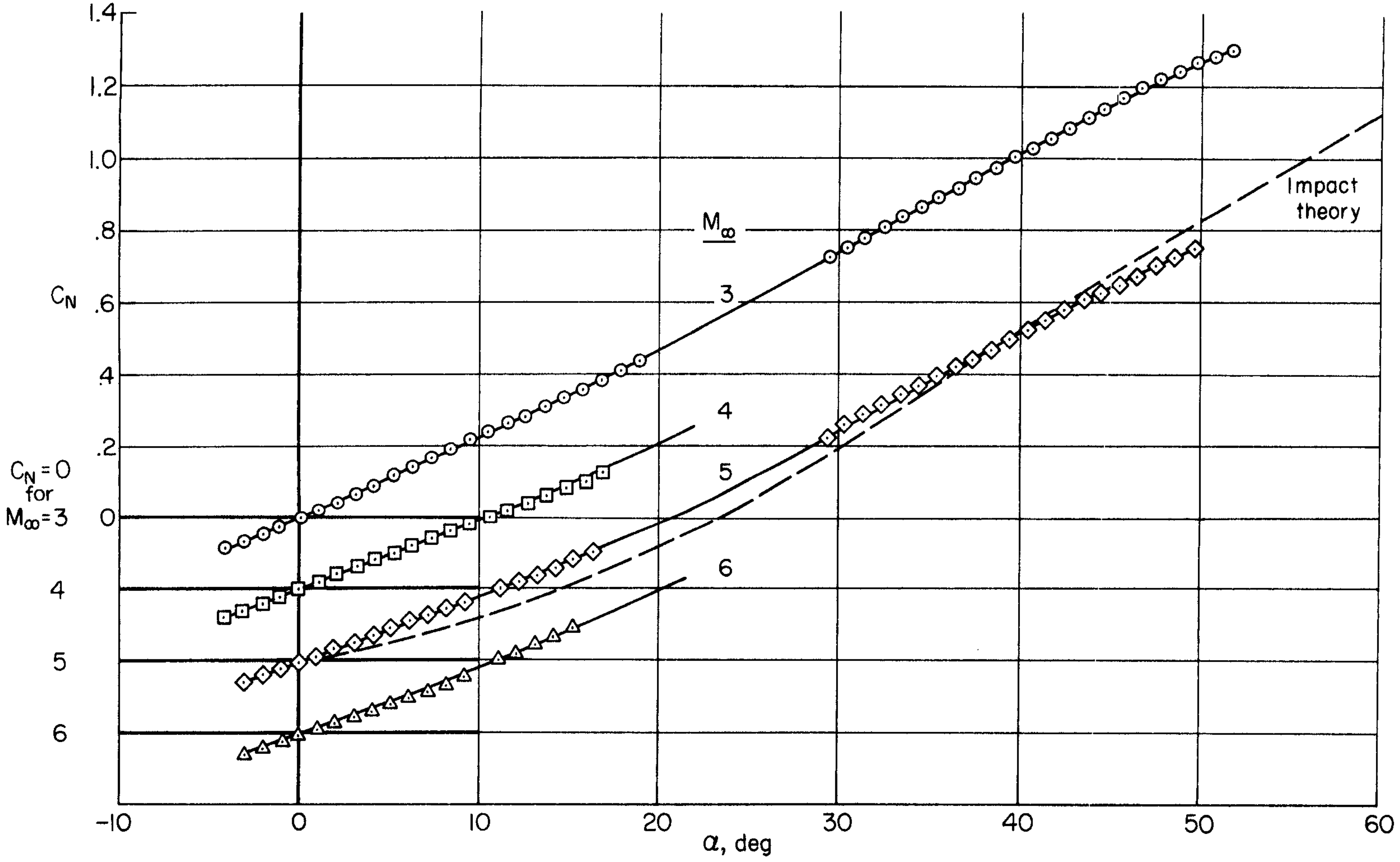

(a) Normal force

Figure 13.- Aerodynamic characteristics of model 4; M_∞ = 3 to 6.

[redacted]

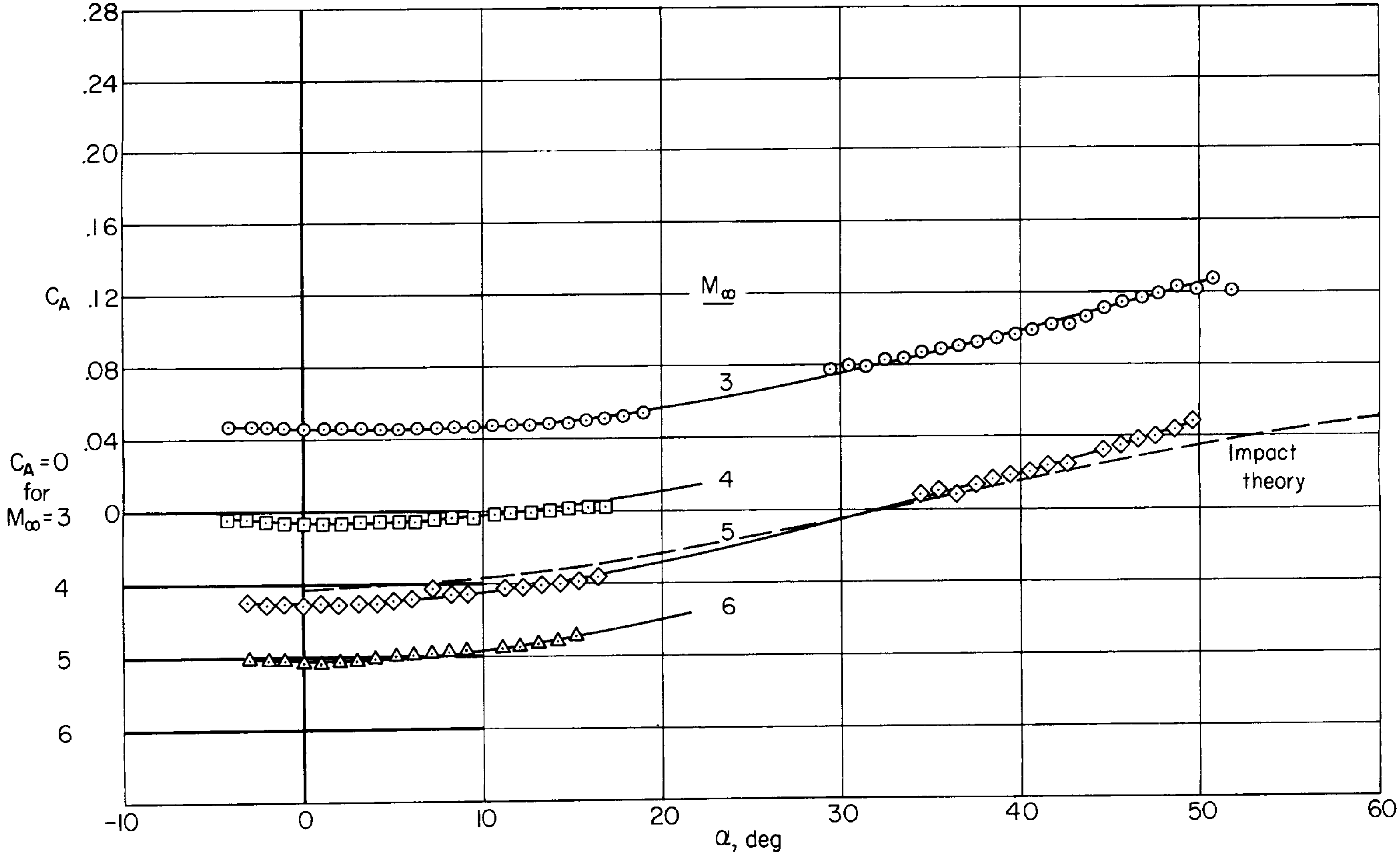

(b) Axial force

Figure 13.- Continued.

[redacted]

A
2
5
9

[redacted]

[redacted]

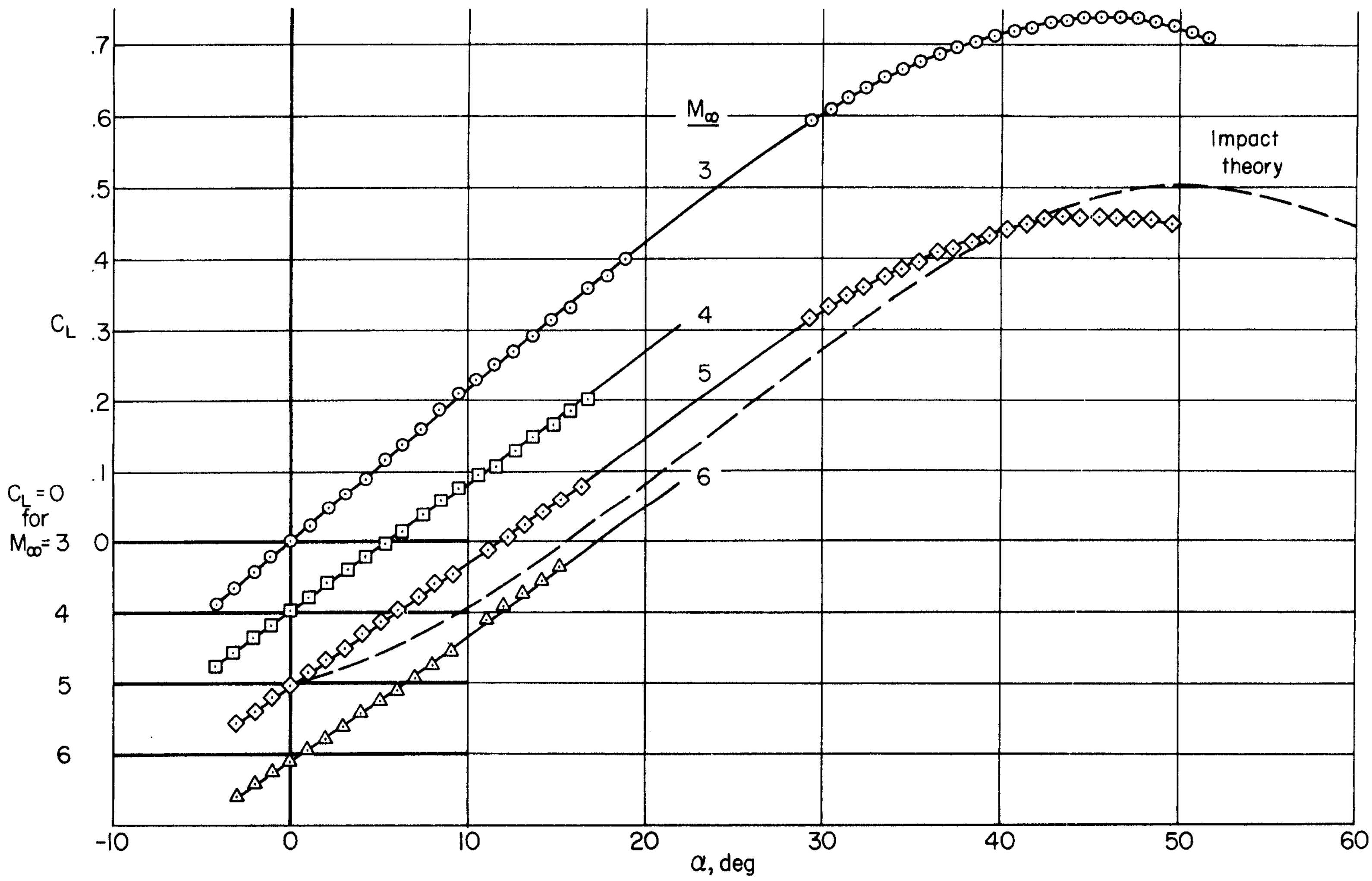

(c) Lift

Figure 13.- Continued.

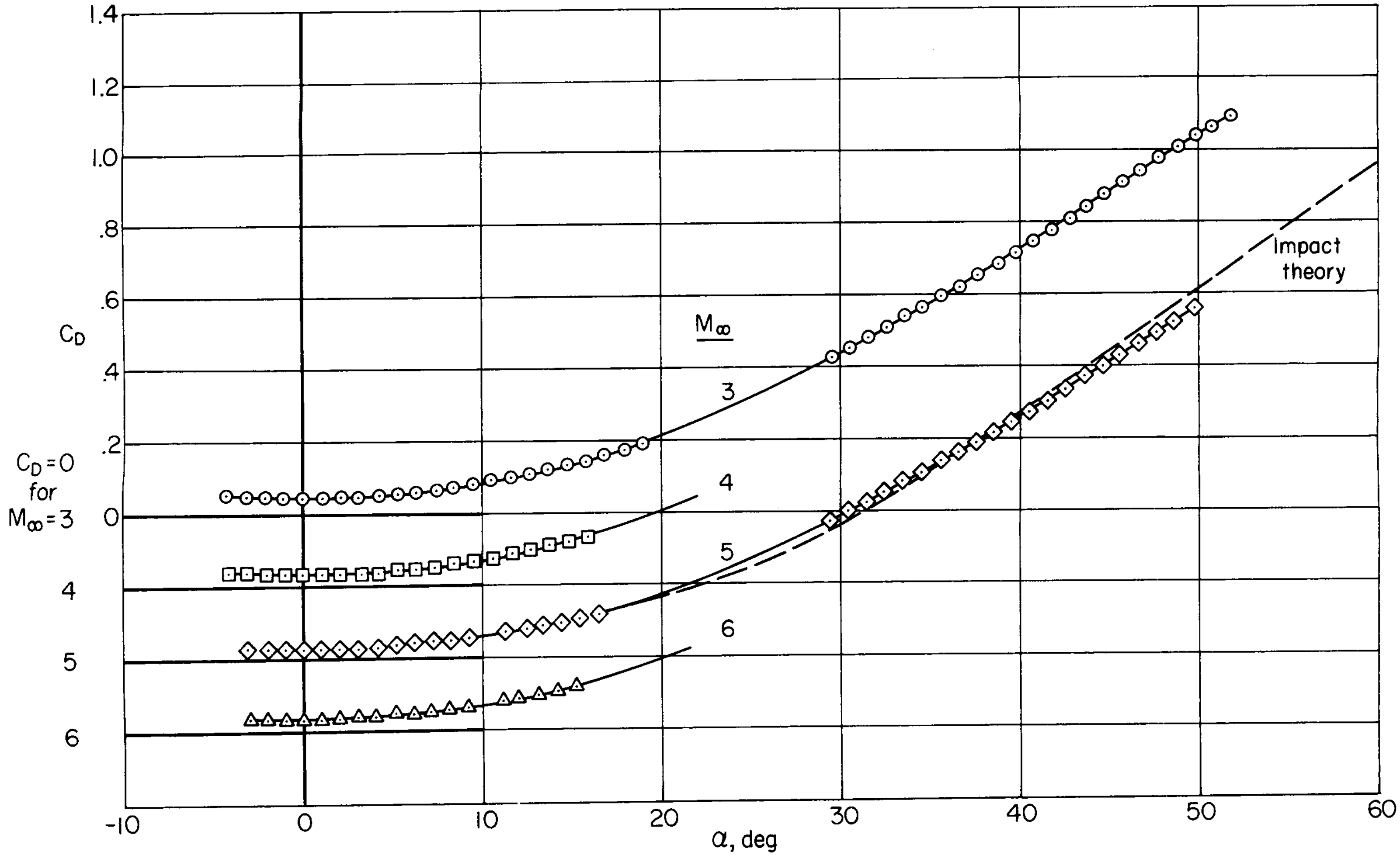

(d) Drag

Figure 13.- Continued.

[redacted]

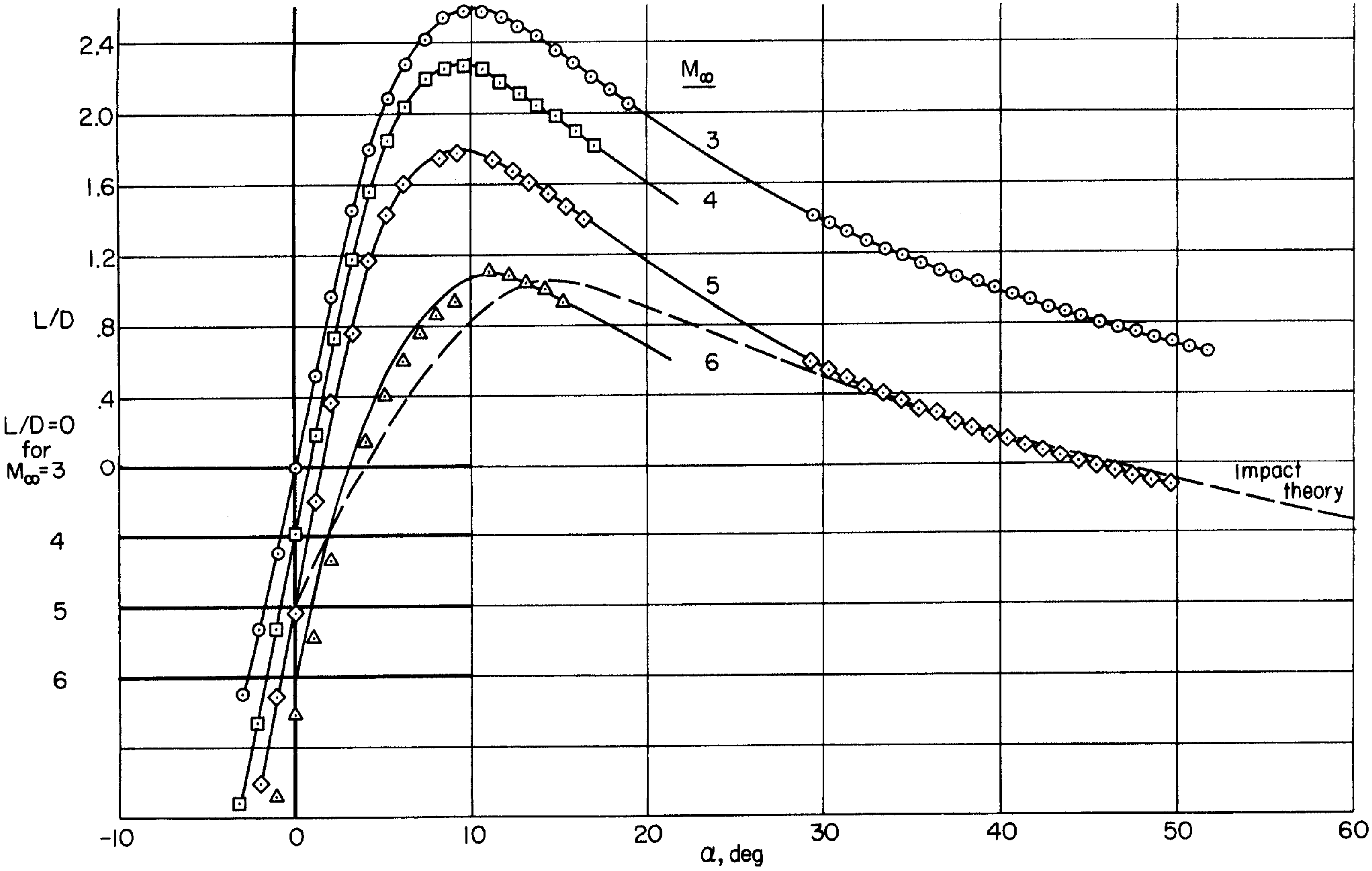

(e) Lift-drag ratio

Figure 13.- Continued.

[redacted]

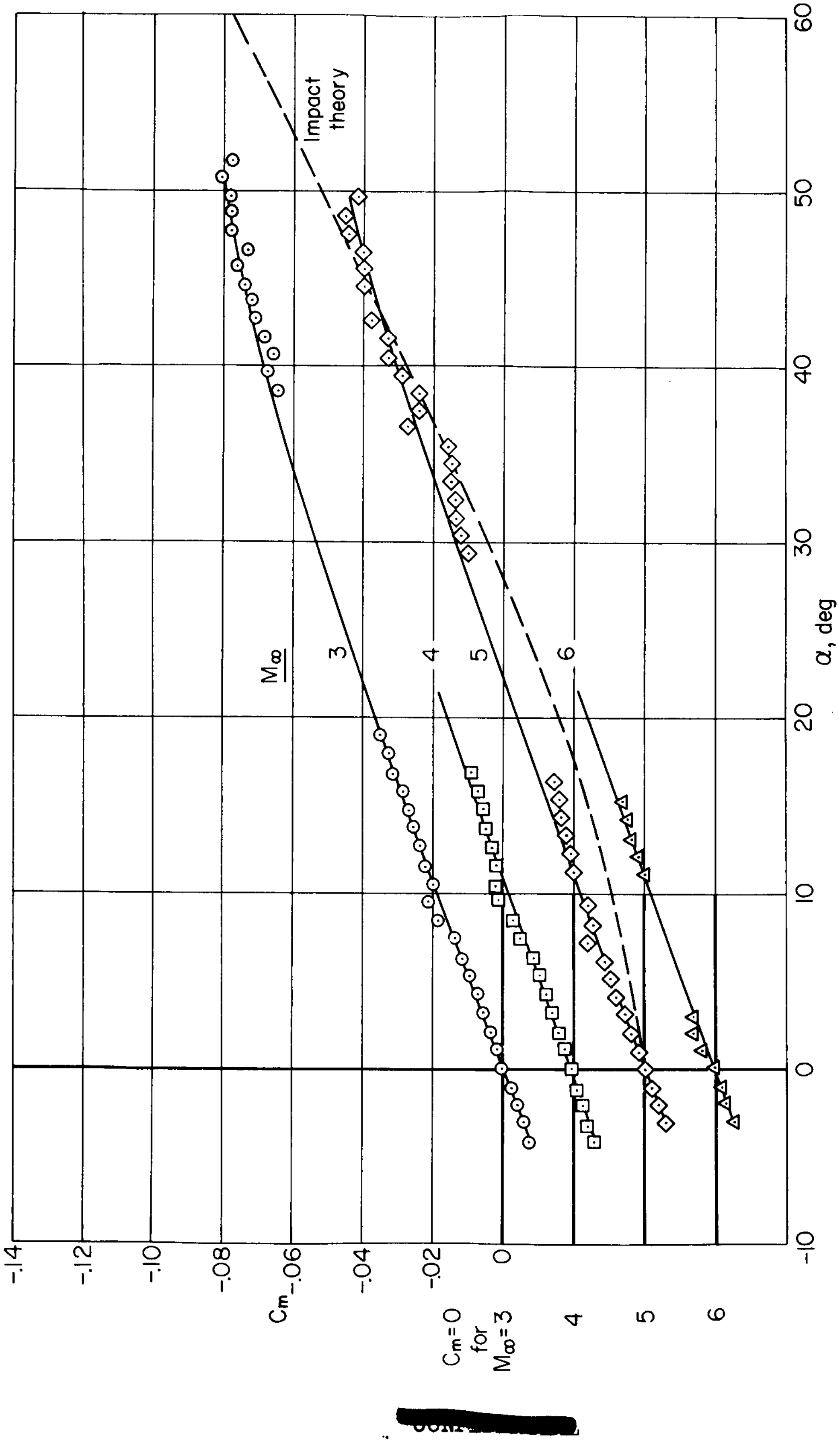

(f) Pitching moment.

Figure 13.- Continued.

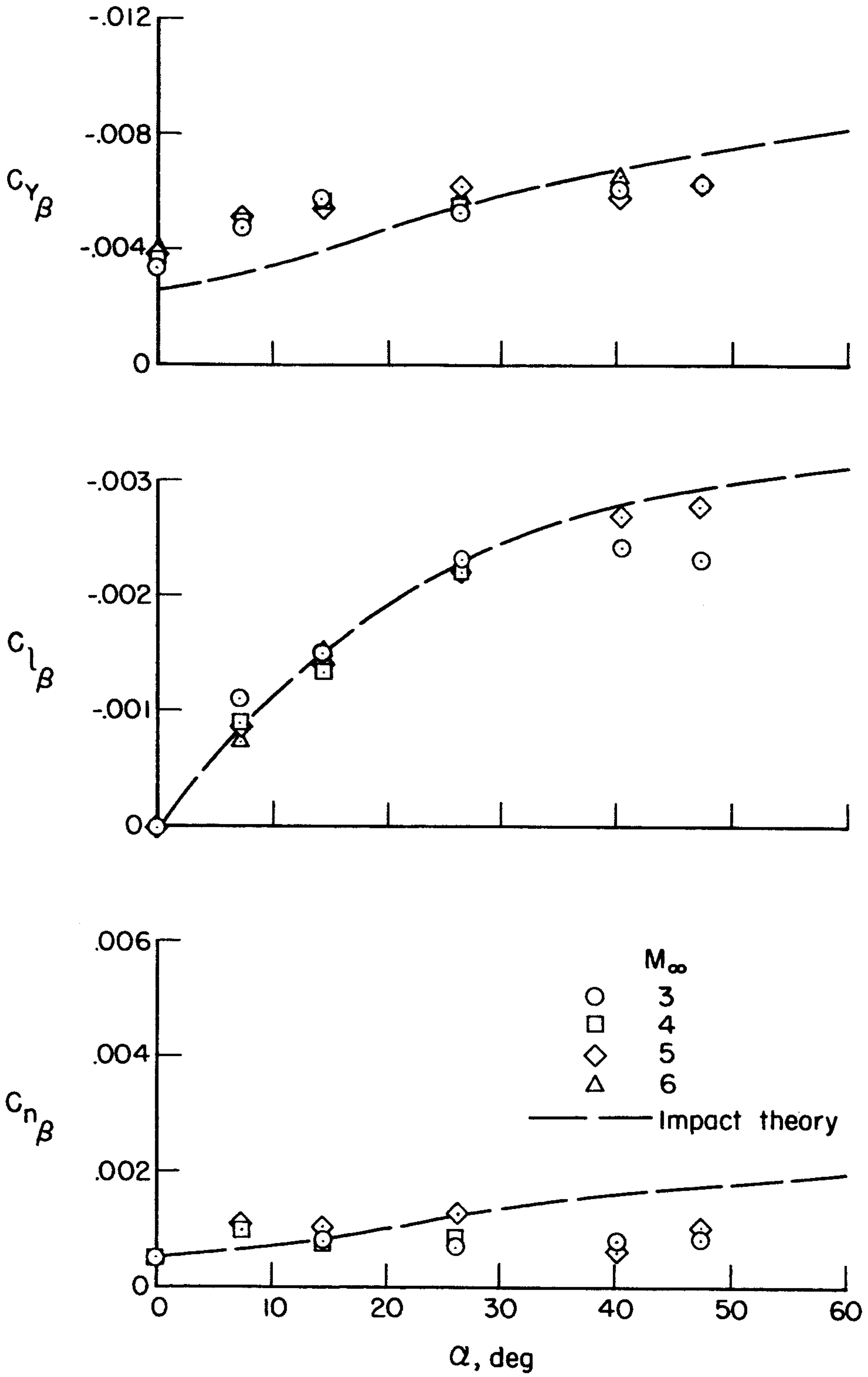

(g) Lateral stability derivatives.

Figure 13.- Concluded.

[redacted]

[redacted]

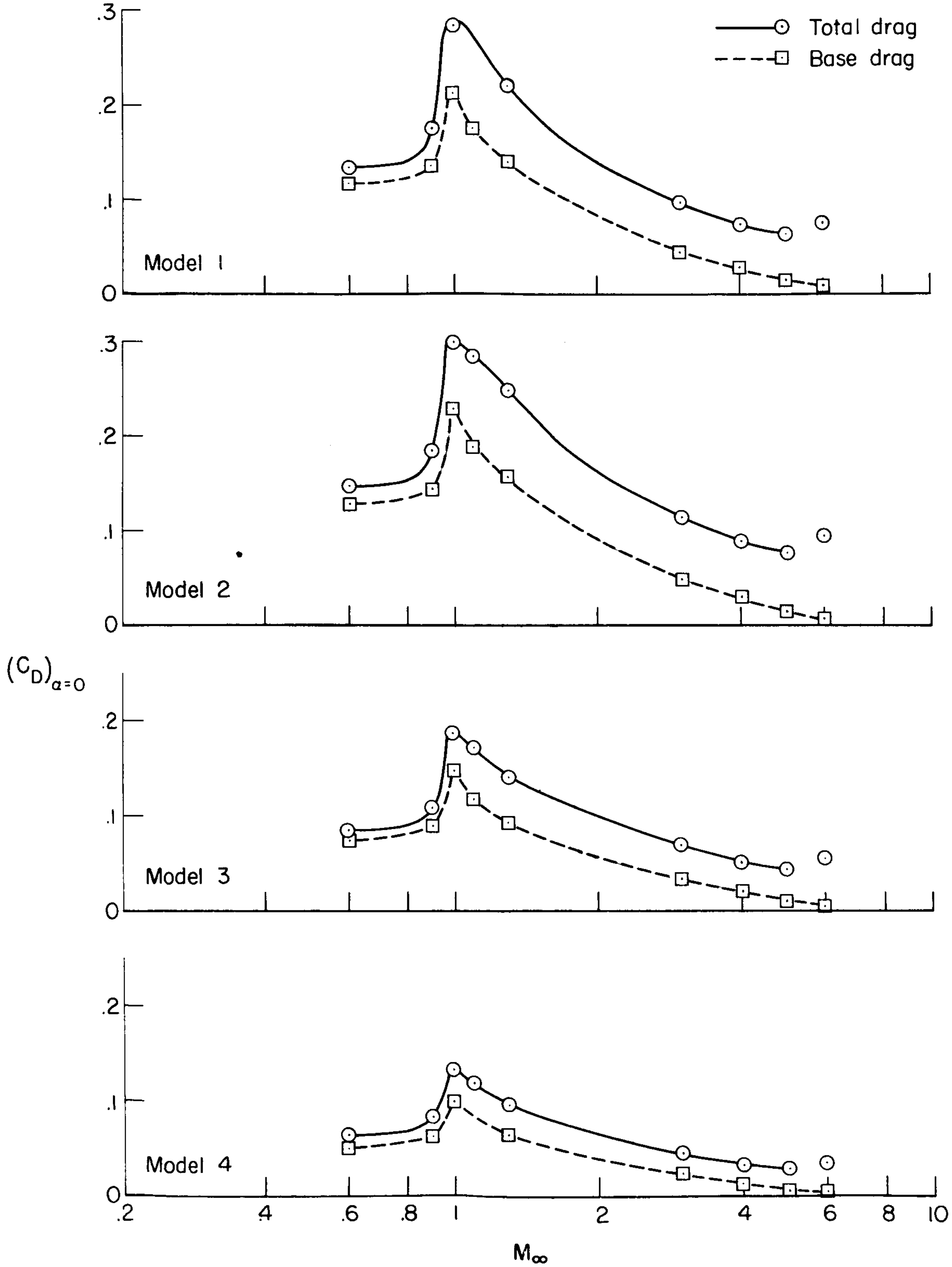

Figure 14.- Comparison of total drag and base drag at zero angle of attack.

[redacted]

A
2
5
9

[redacted]

A
2
5
9

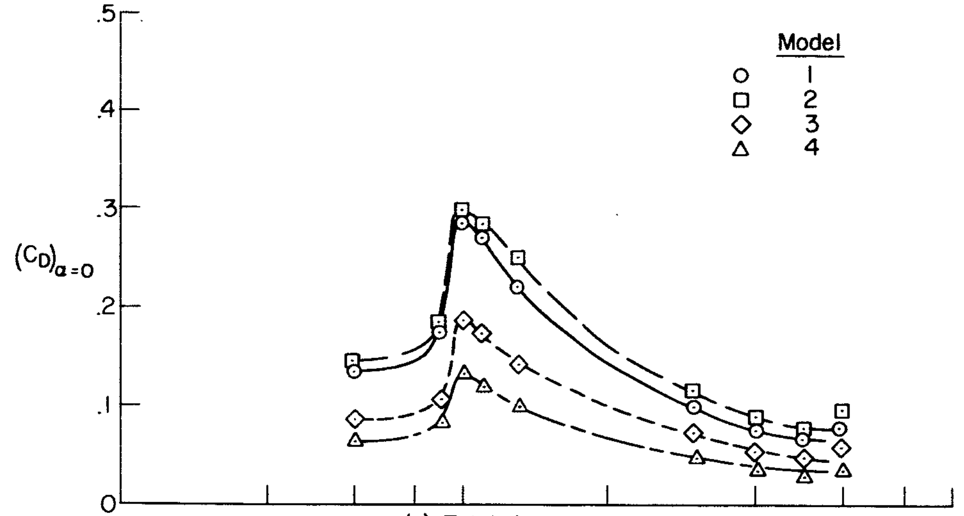

(a) Total drag.

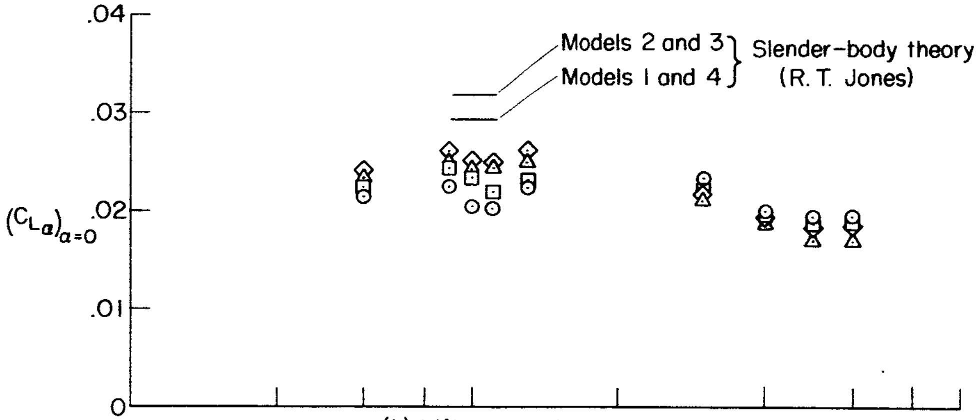

(b) Lift-curve slope.

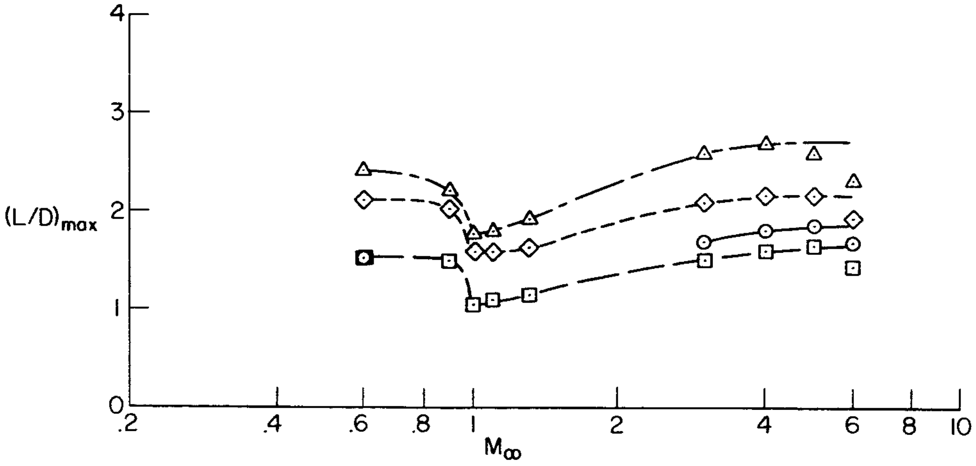

(c) Maximum lift-drag ratios.

Figure 15.- The effect of Mach number on total drag and lift-curve slope at zero lift and on maximum lift-drag ratios.

[redacted]

[redacted]

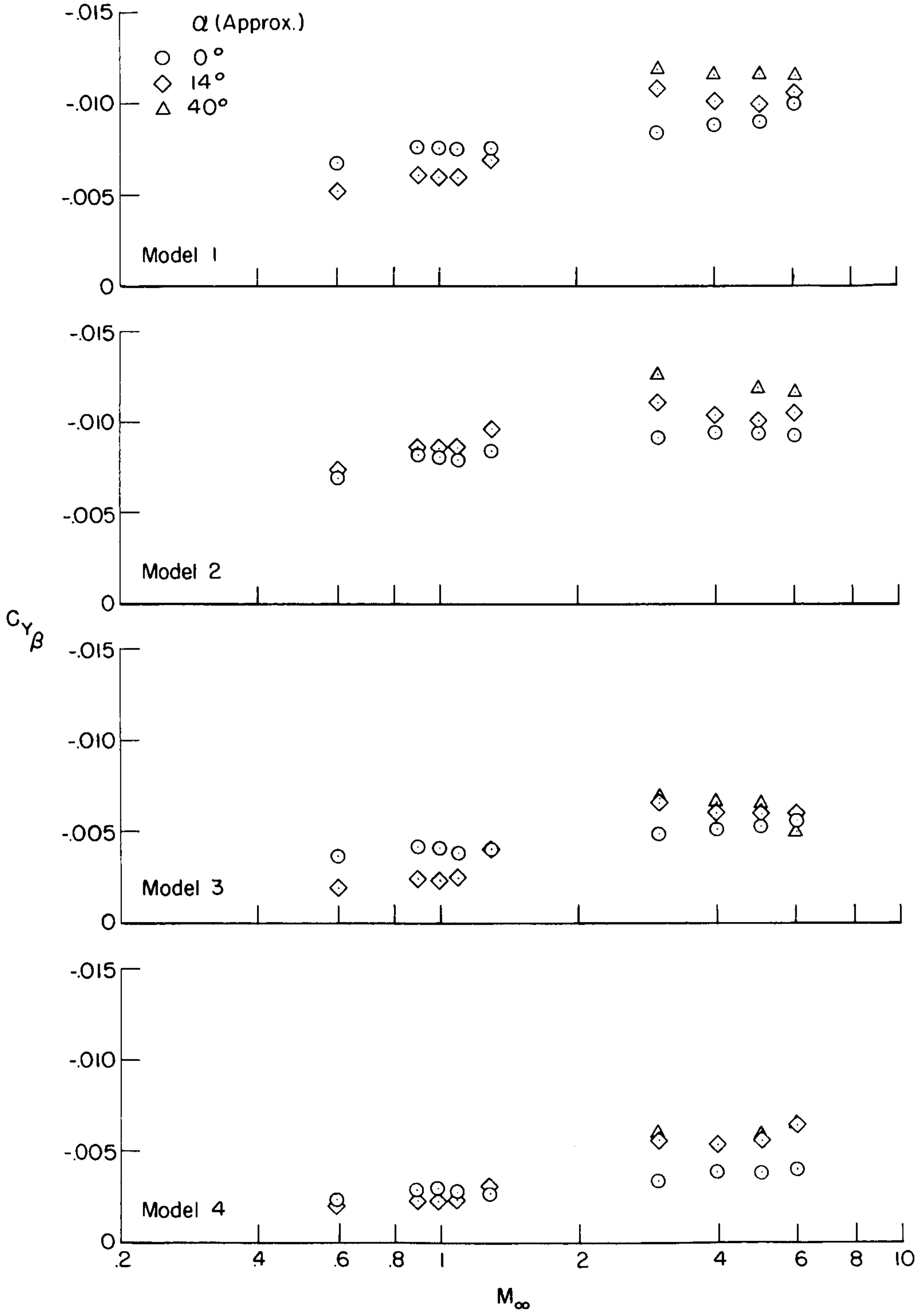

(a) C_{Y_β}

Figure 16.- The effect of Mach number on lateral stability derivatives.

[redacted]

A
2
5
9

A
2
5
9

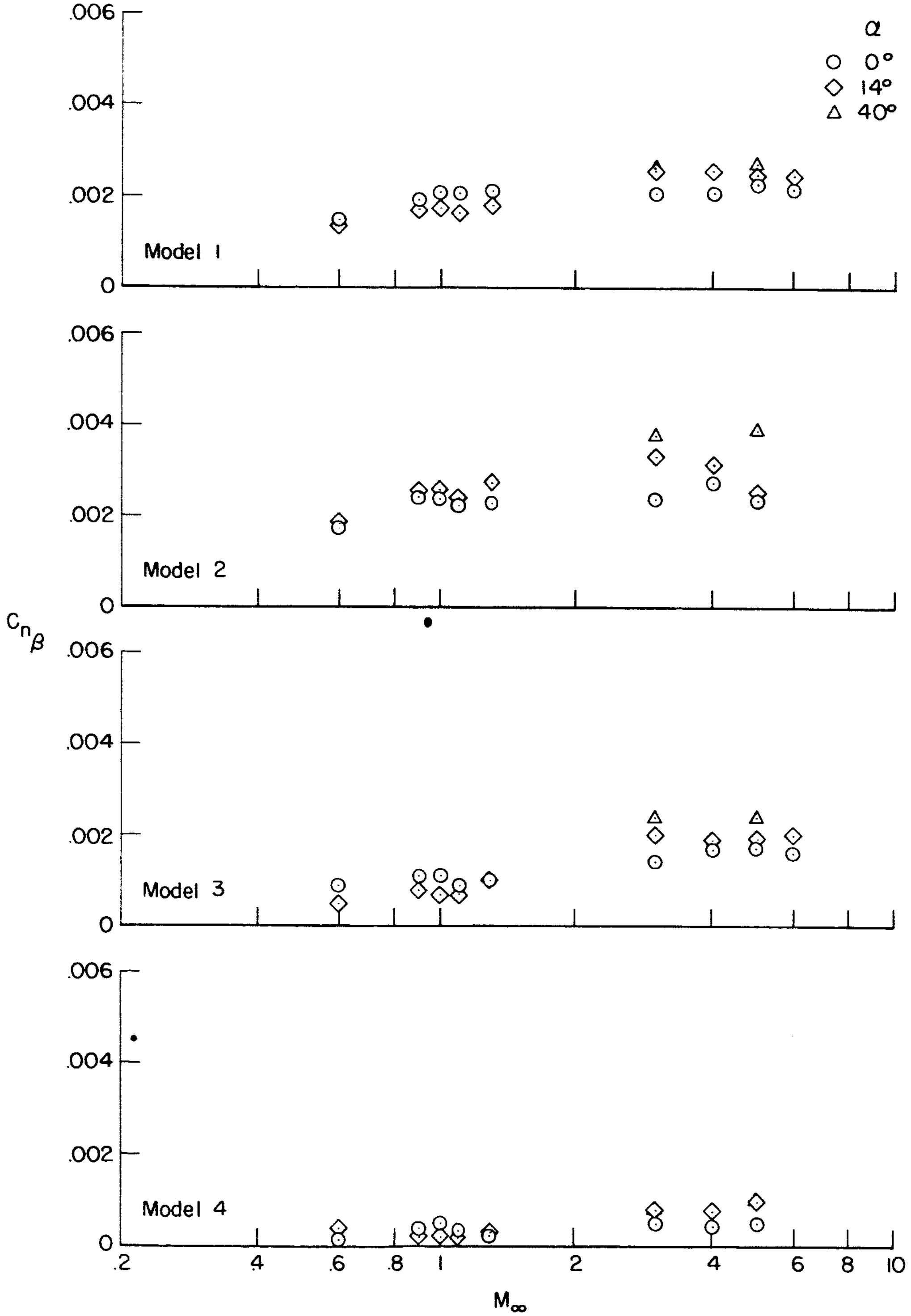

(b) C_{n_β}

Figure 16.- Continued.

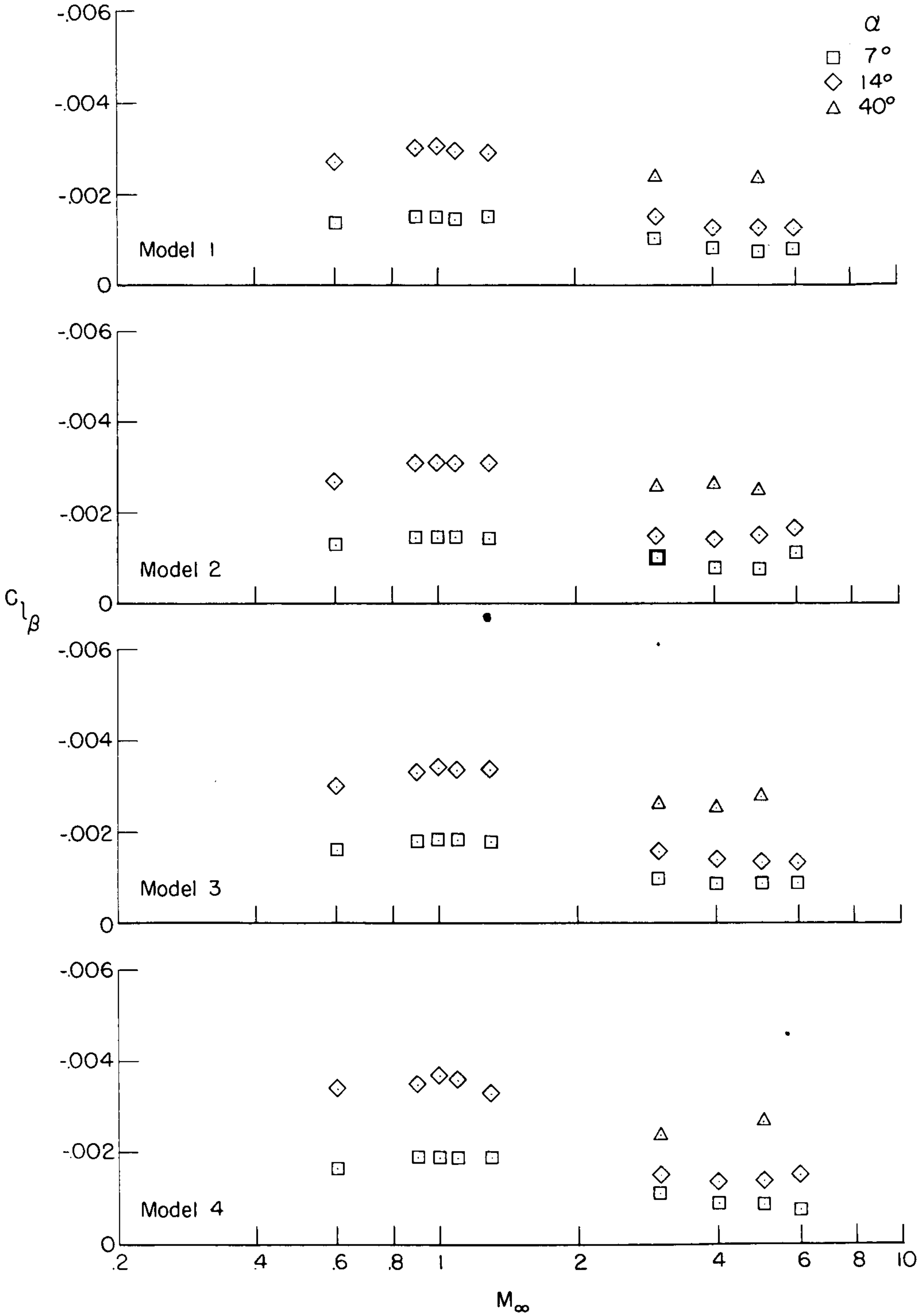

(c) C_{l_β}

Figure 16.- Concluded.

[redacted]

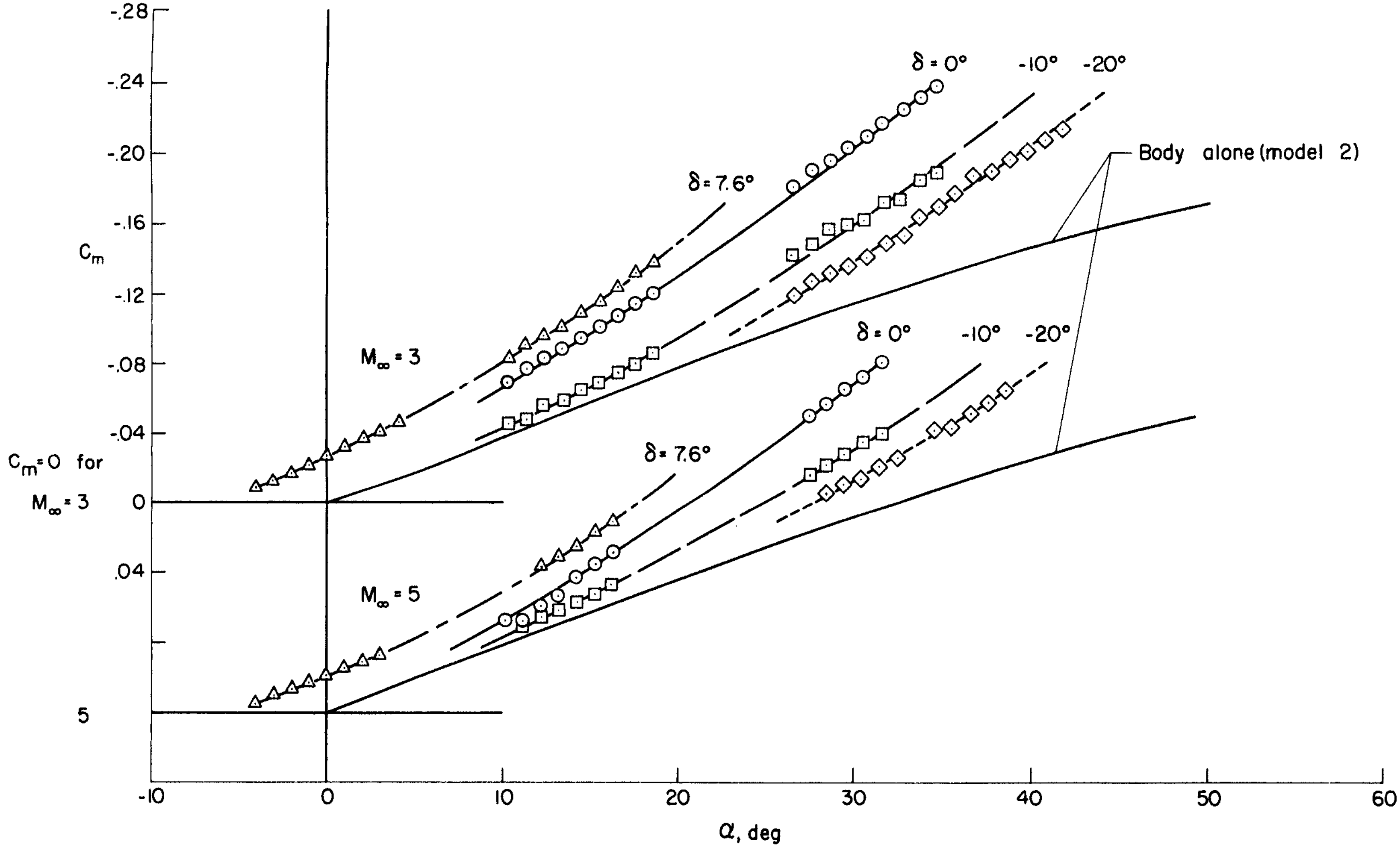

Figure 17.- Pitching-moment coefficients for model 2 with trailing-edge controls.

[redacted]

[redacted]

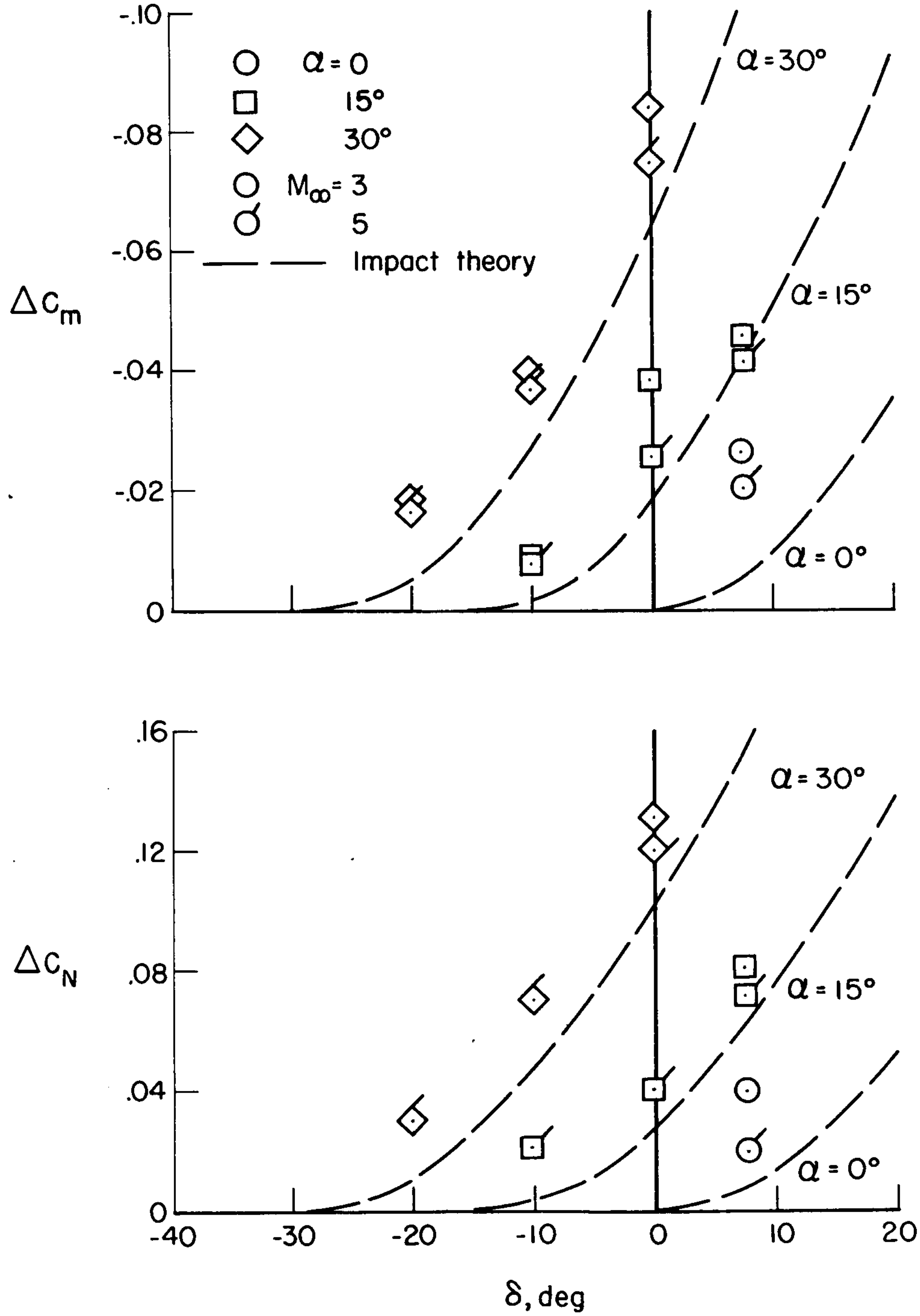

Figure 18.- Variation of incremental pitching-moment and normal-force coefficients with control deflection for model 2 with trailing-edge controls.

[redacted]

[redacted]

A259

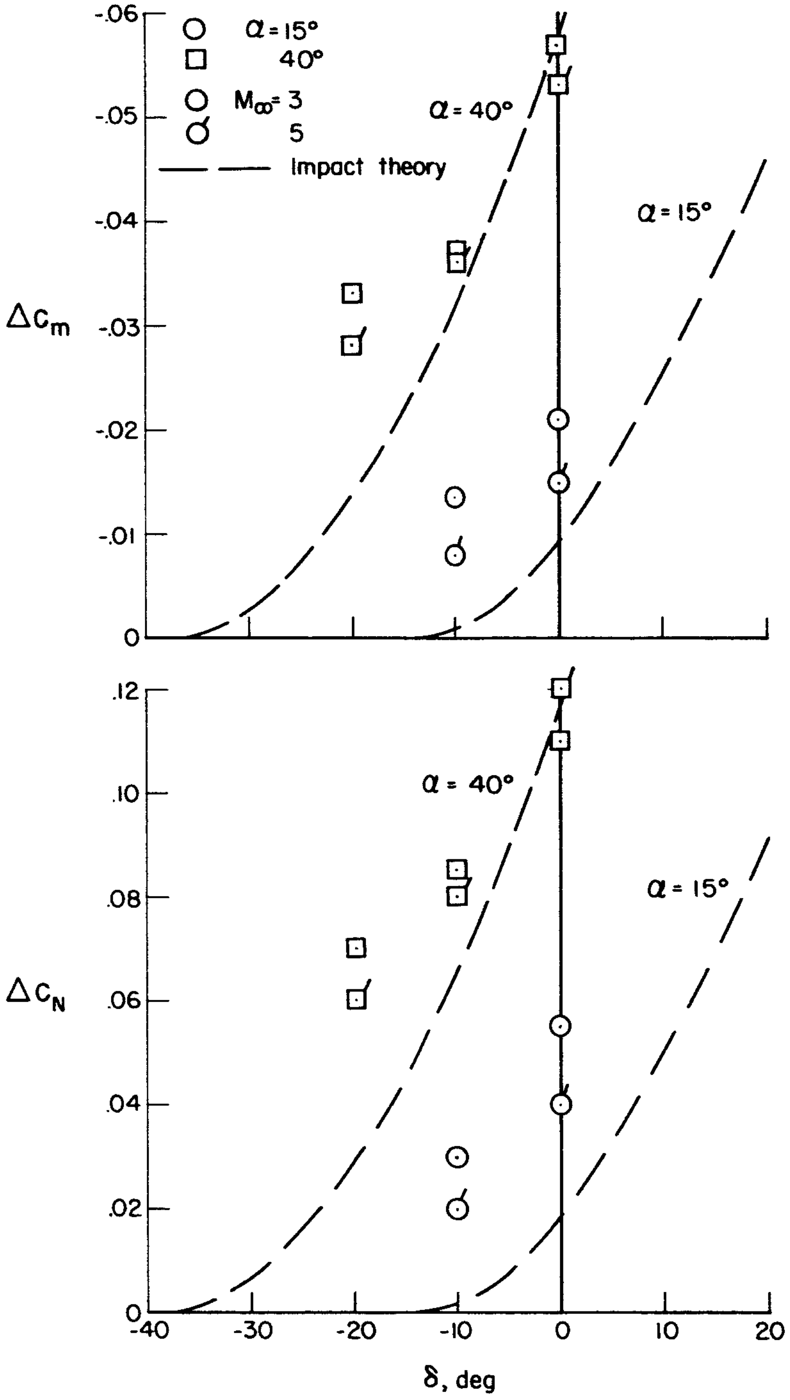

Figure 19.- Variation of incremental pitching-moment and normal-force coefficients with control deflection for model 4 with trailing-edge controls.

[redacted]

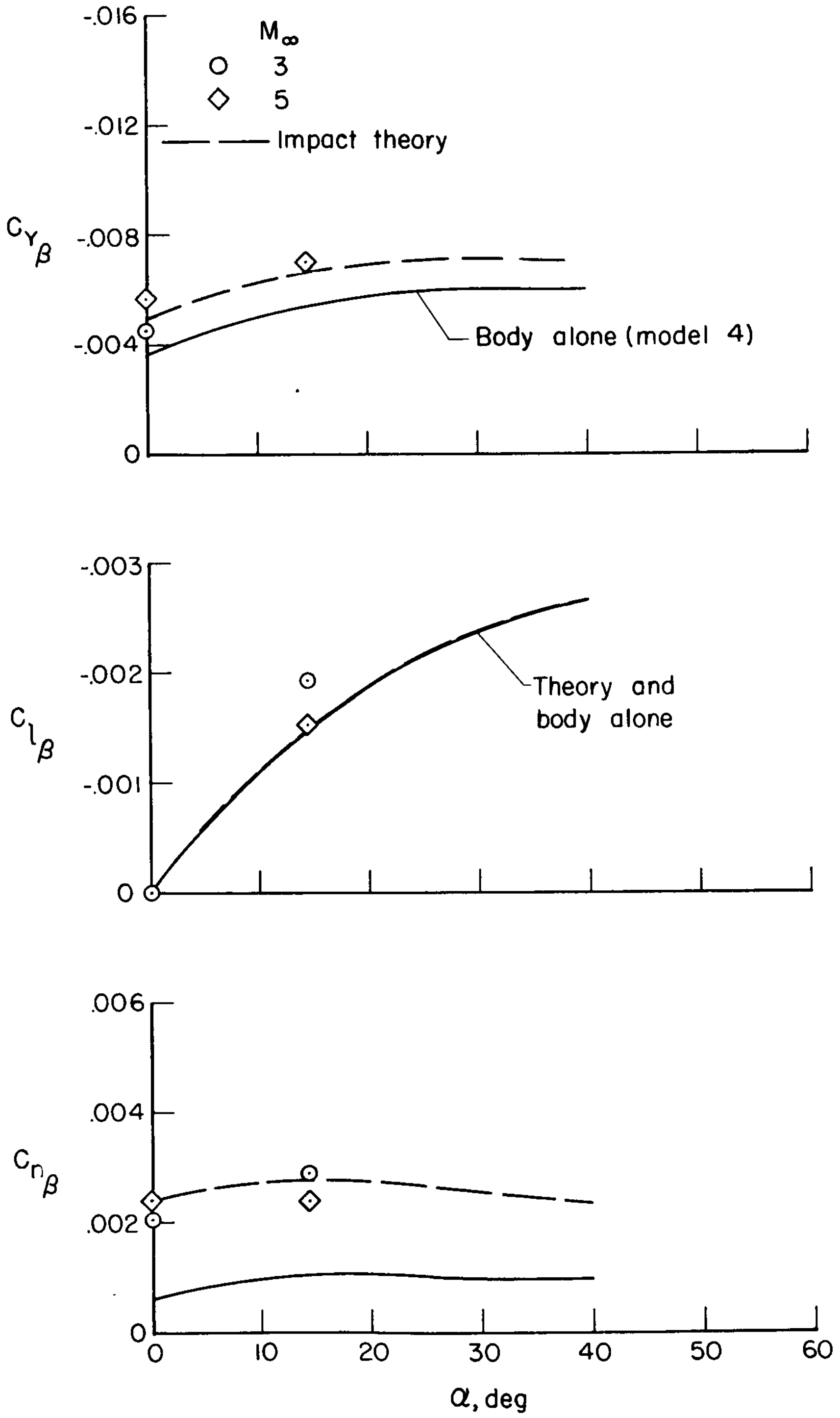

(a) Controls horizontal ($\theta = 0°$)

Figure 20.- Lateral stability derivatives for model 4 with rotavons (tip controls).

[redacted]

A
2
5
9

[redacted]

A
2
5
9

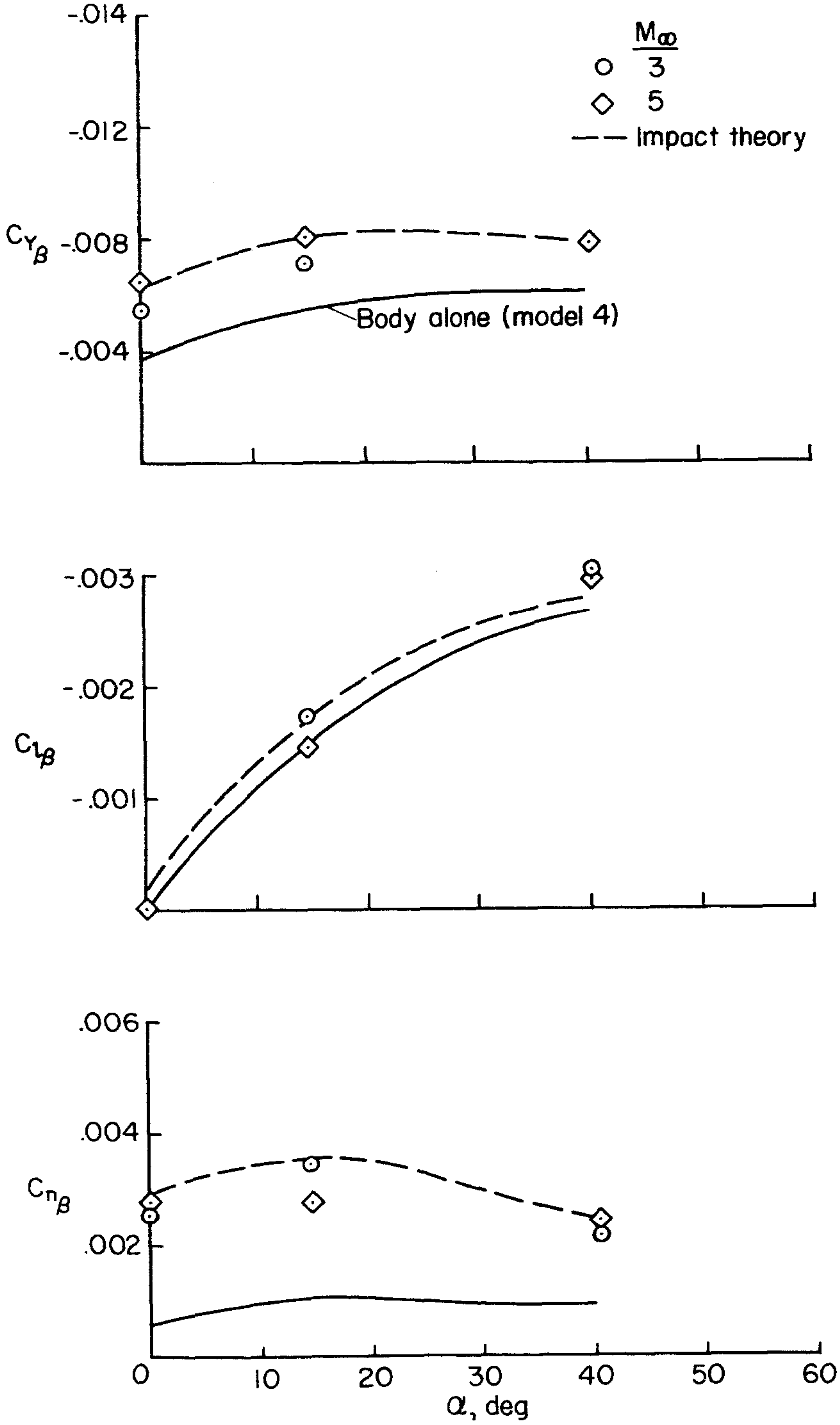

(b) Controls vertical (θ=90°)

Figure 20.- Concluded.

[redacted]

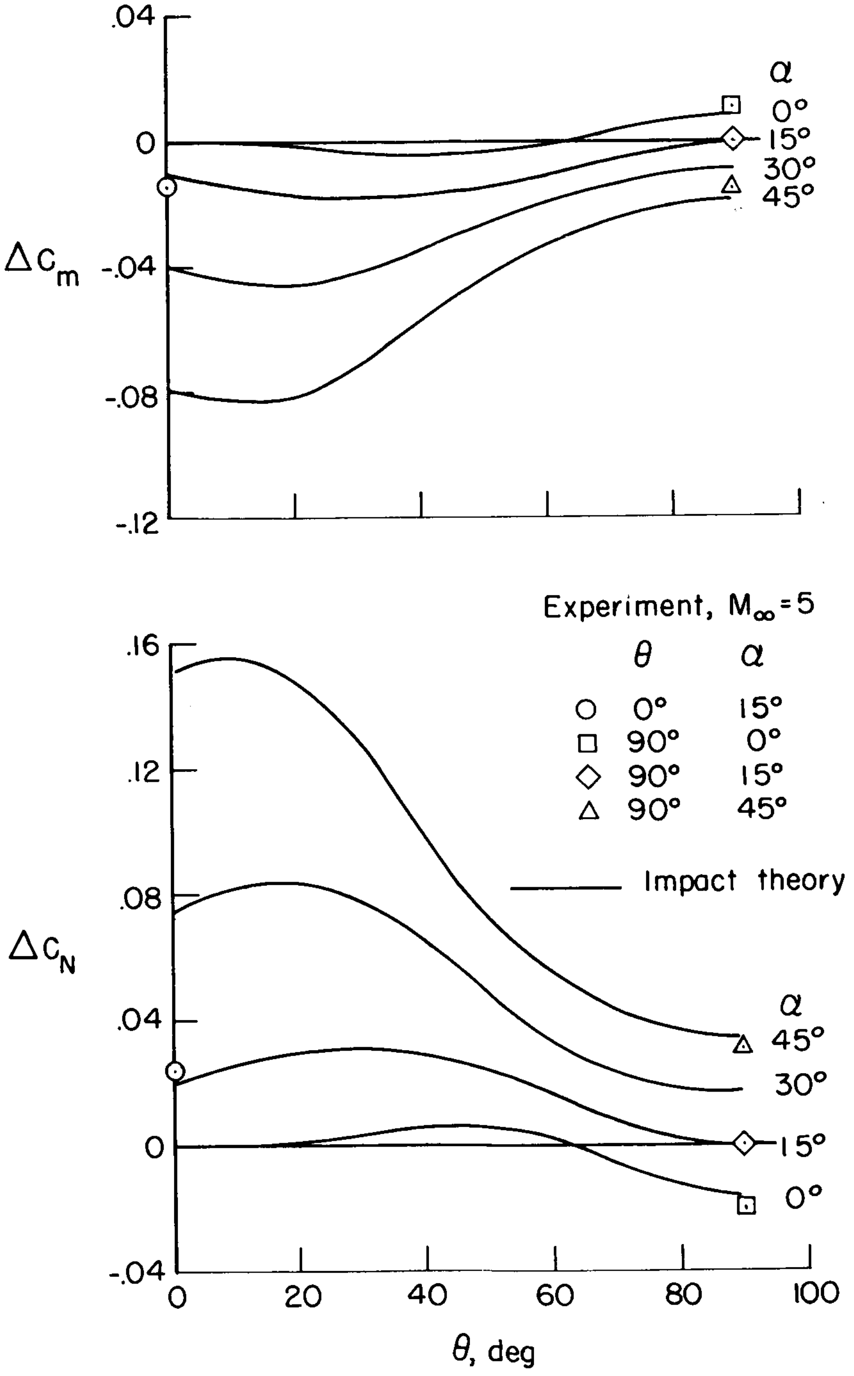

(a) Pitching moment and normal force increments.

Figure 21.- Estimated incremental quantities (impact theory) for the two rotavons used in conjunction with model 4.

[redacted]

[redacted]

A259

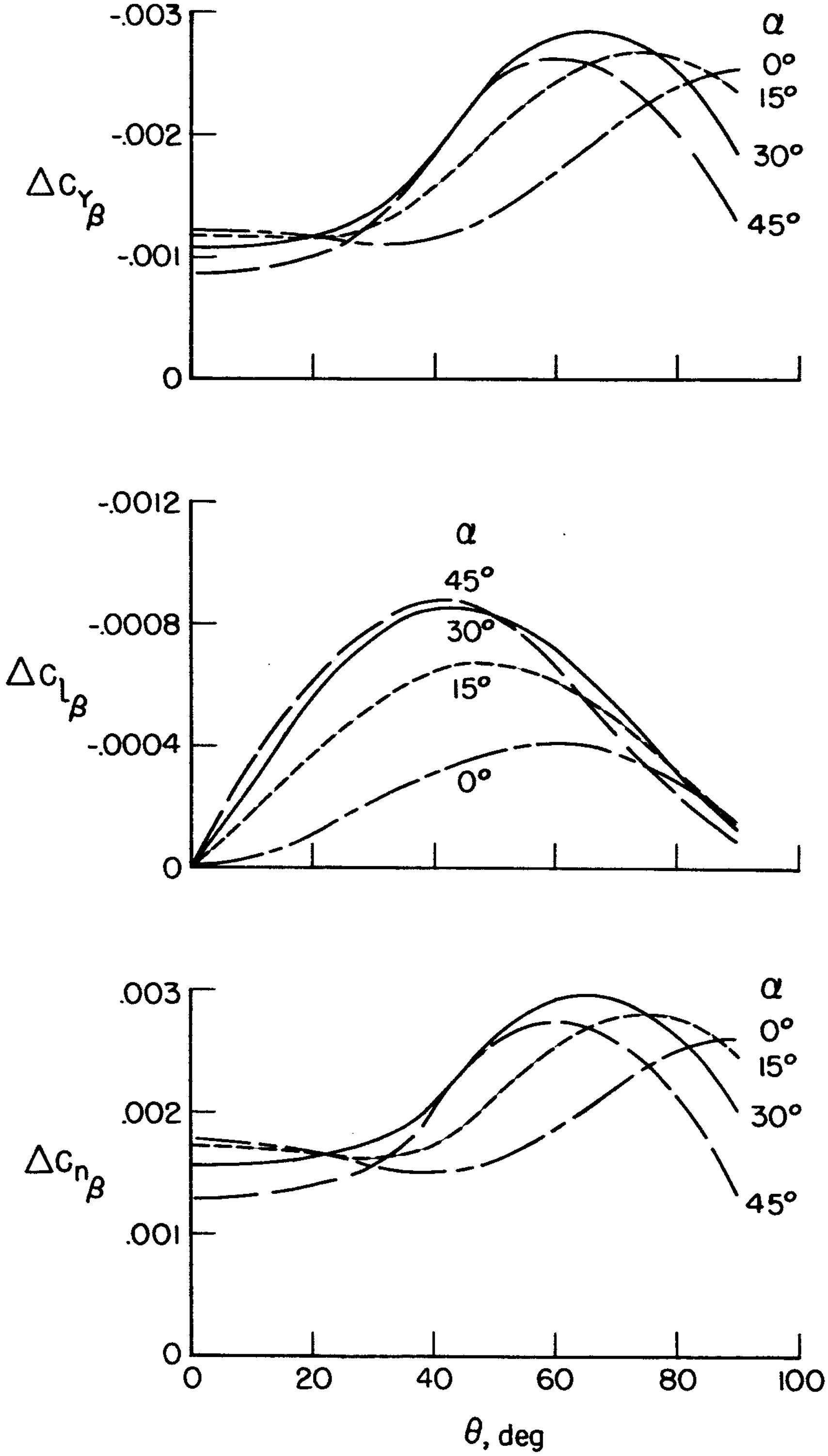

(b) Lateral stability increments (Impact theory)

Figure 21.- Concluded.

[redacted]

[redacted]

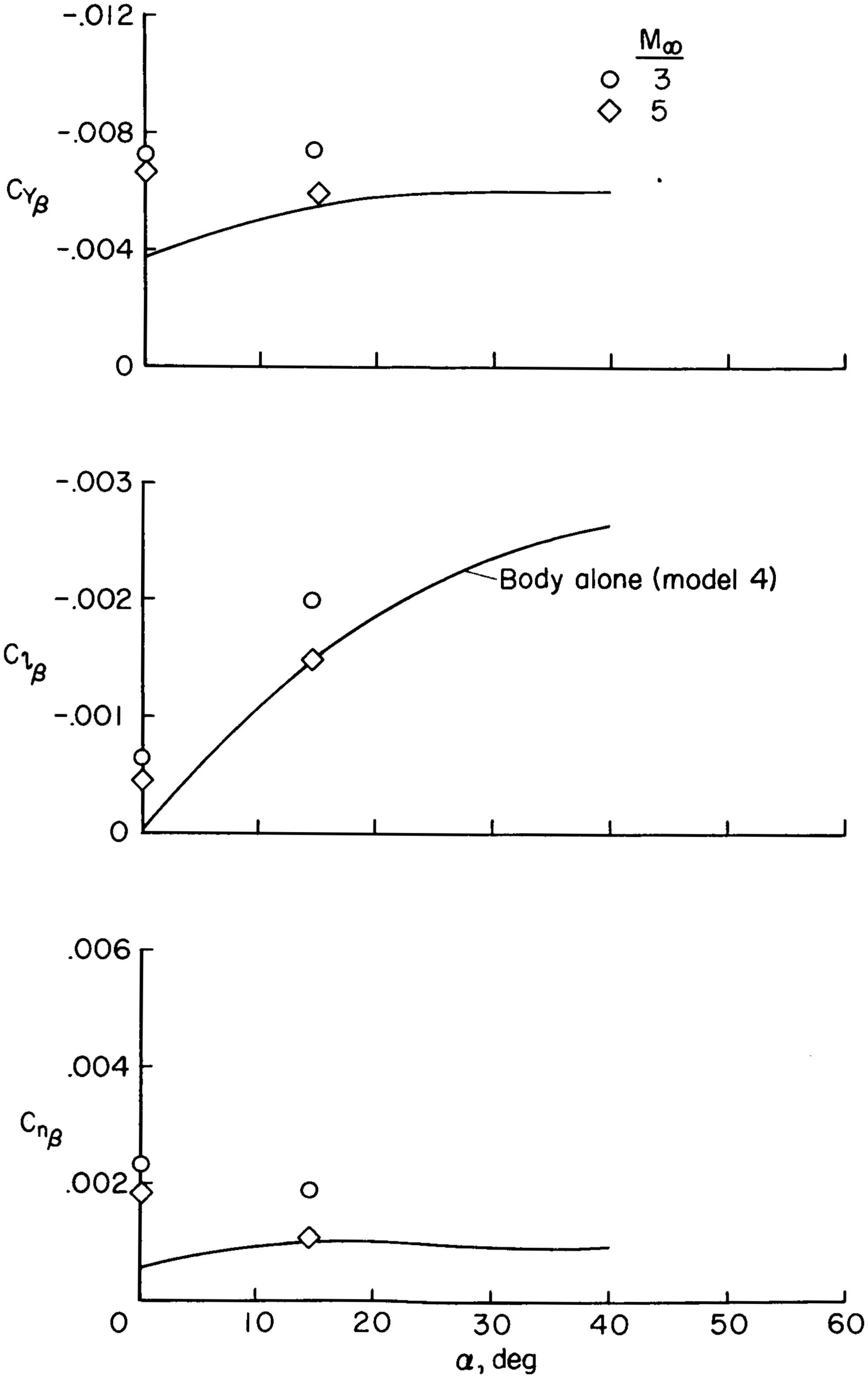

Figure 22.- Lateral stability derivatives for model 4 with vertical stabilizer (dorsal fin).

[redacted]

[redacted]

A
2
5
9

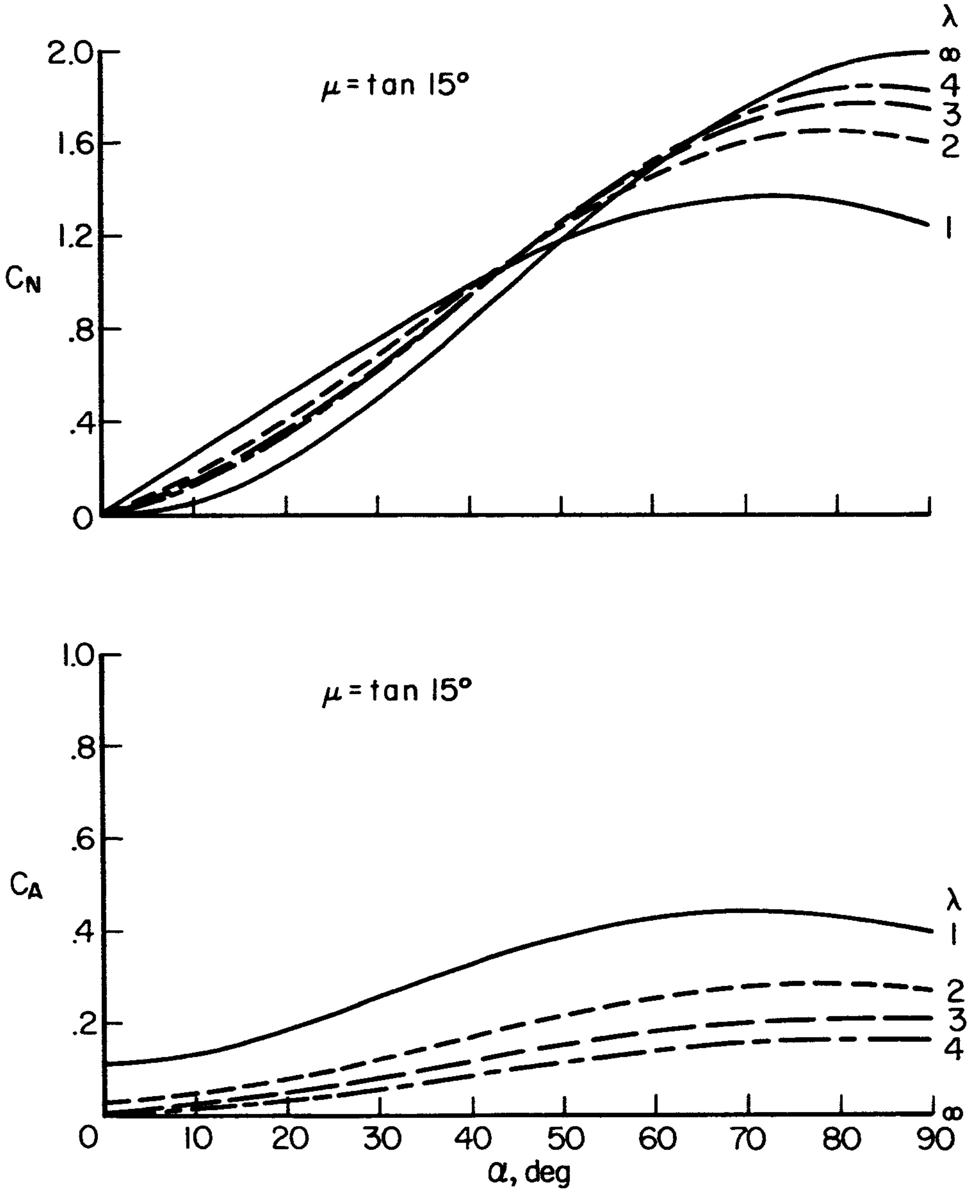

(a) Normal and axial forces.

Figure 23.- Impact calculations for sharp elliptic cones.

[redacted]

DECLASSIFIED

[redacted]

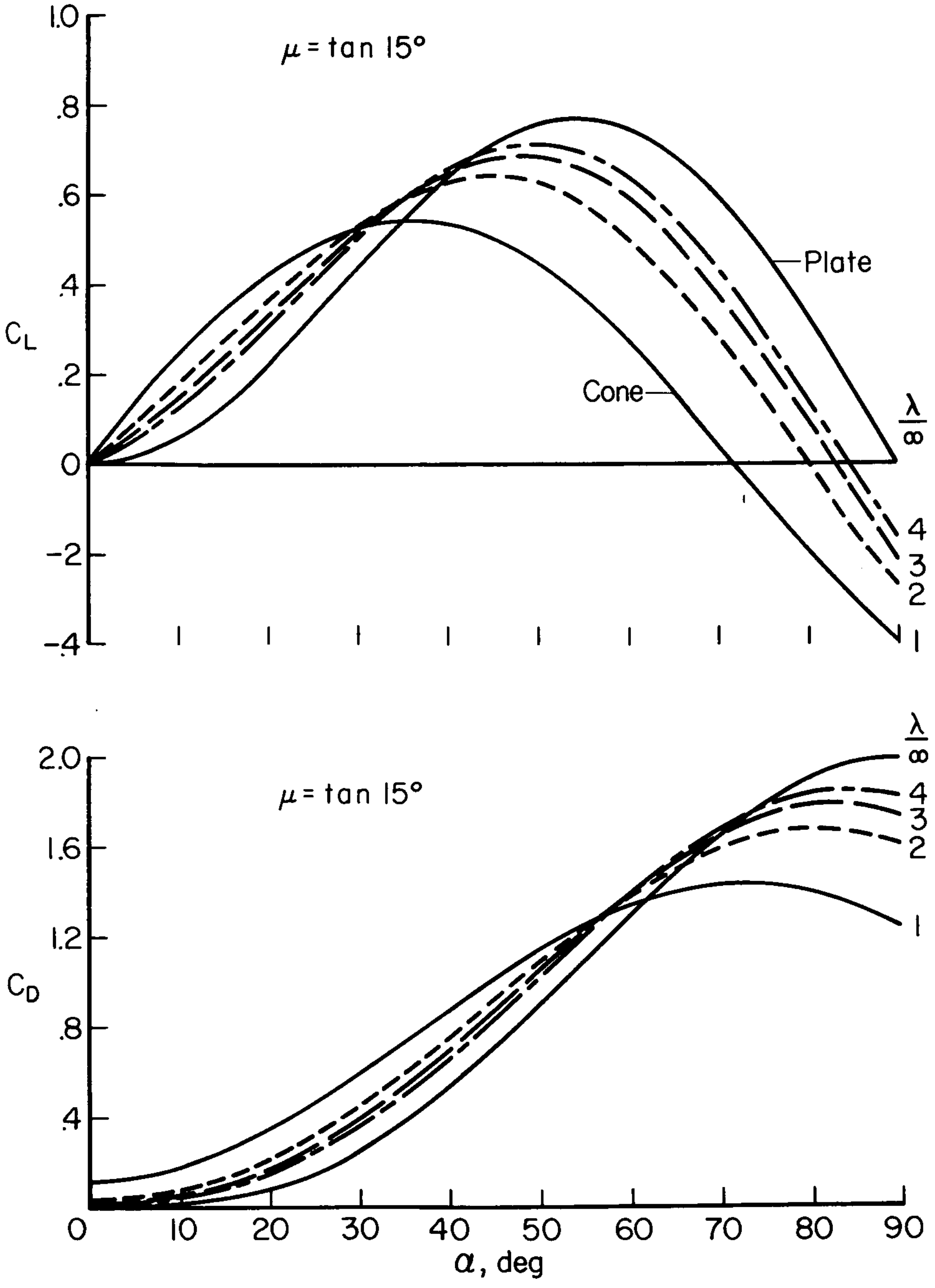

(b) Lift and drag.

Figure 23.- Continued.

A
2
5
9

[redacted]

[redacted]

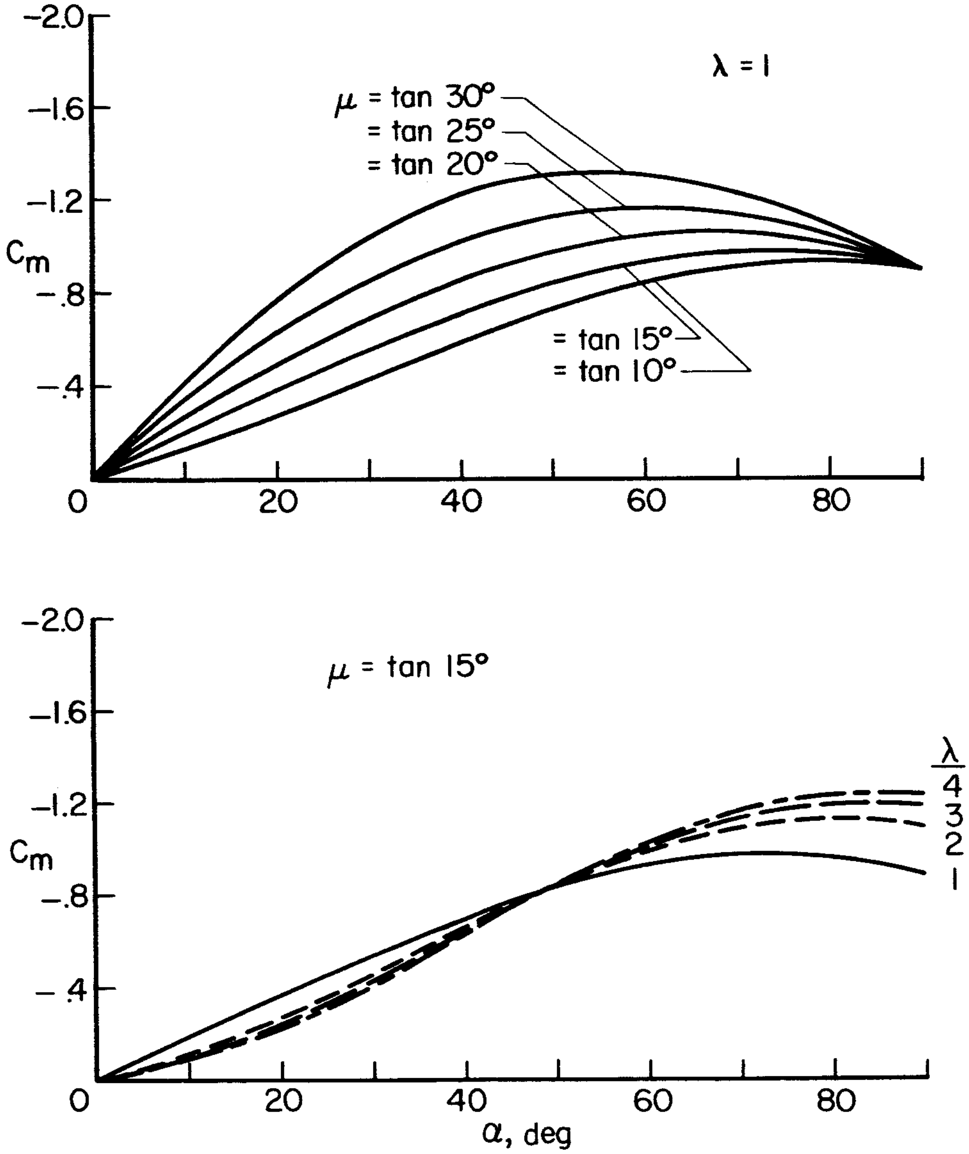

A
2
5
9

(c) Pitching moment about apex.

Figure 23.- Continued.

[redacted]

[redacted]

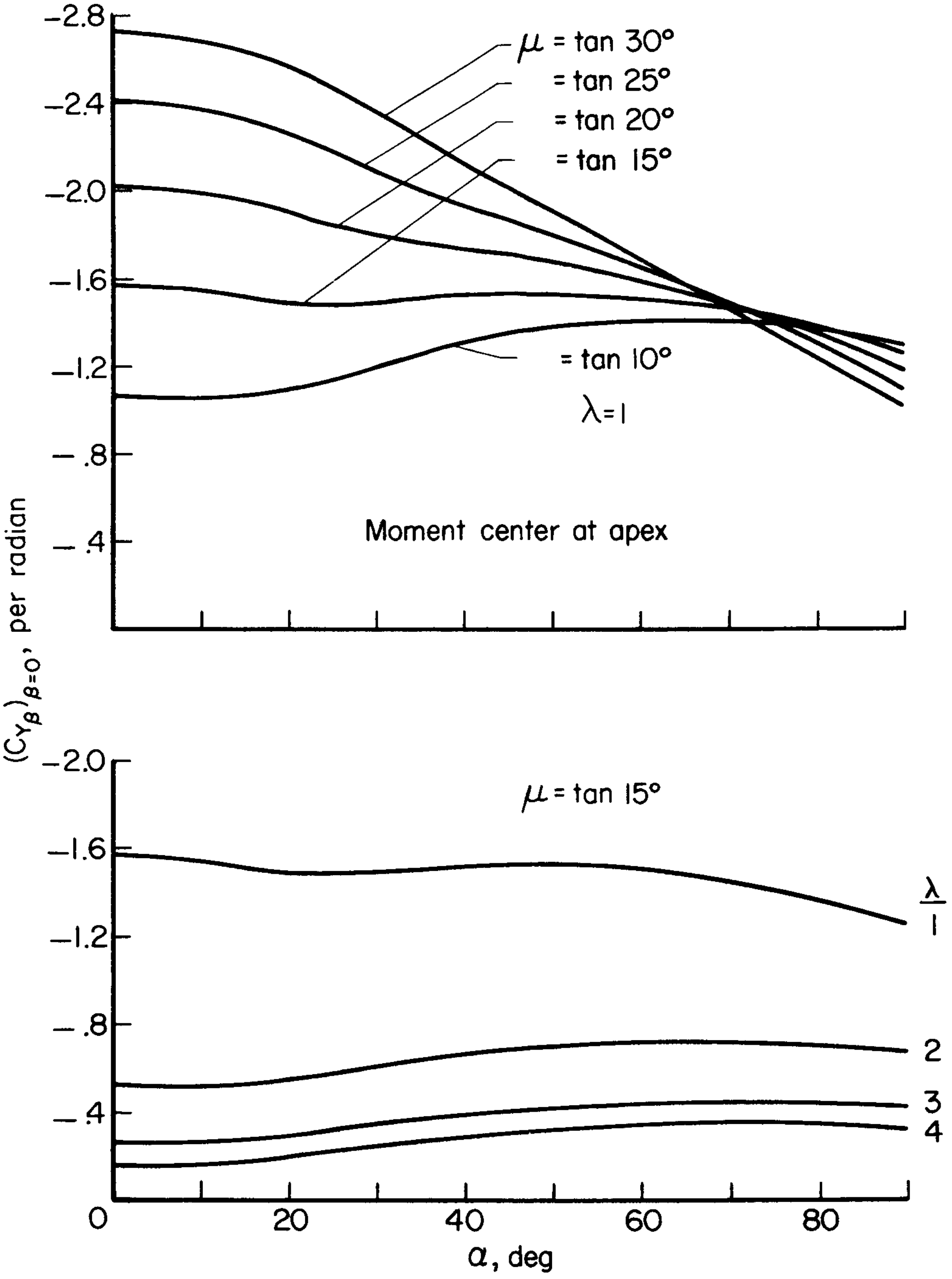

(d) $(C_{Y_\beta})_{\beta=0}$, per radian

Figure 23.- Continued.

A
2
5
9

[redacted]

[redacted]

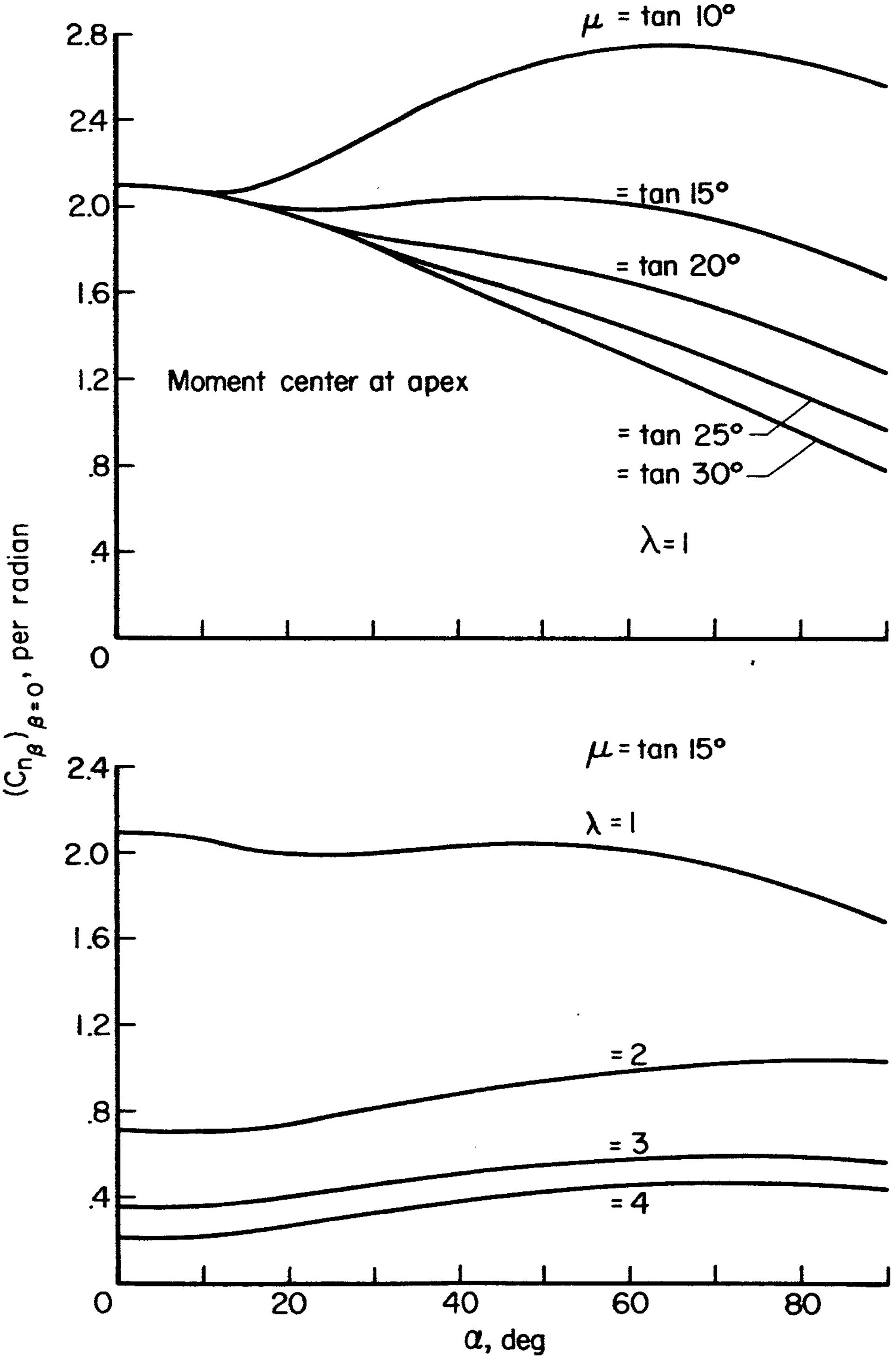

(e) $(C_{n_\beta})_{\beta=0}$, per radian

Figure 23.- Continued.

[redacted]

[redacted]

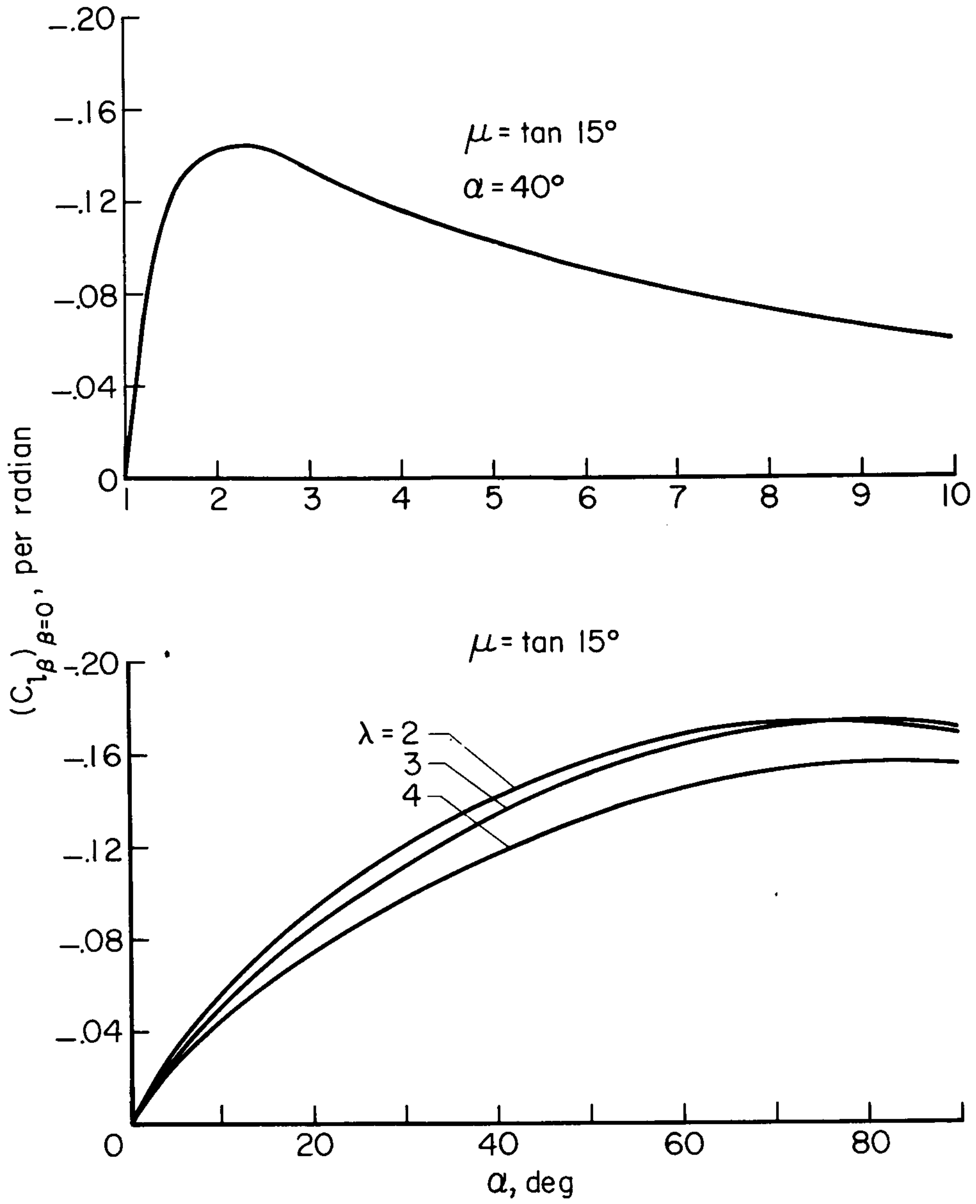

(f) $(C_{l_\beta})_{\beta=0}$, per deg

Figure 23.- Concluded.

[redacted]

[redacted]

[redacted]

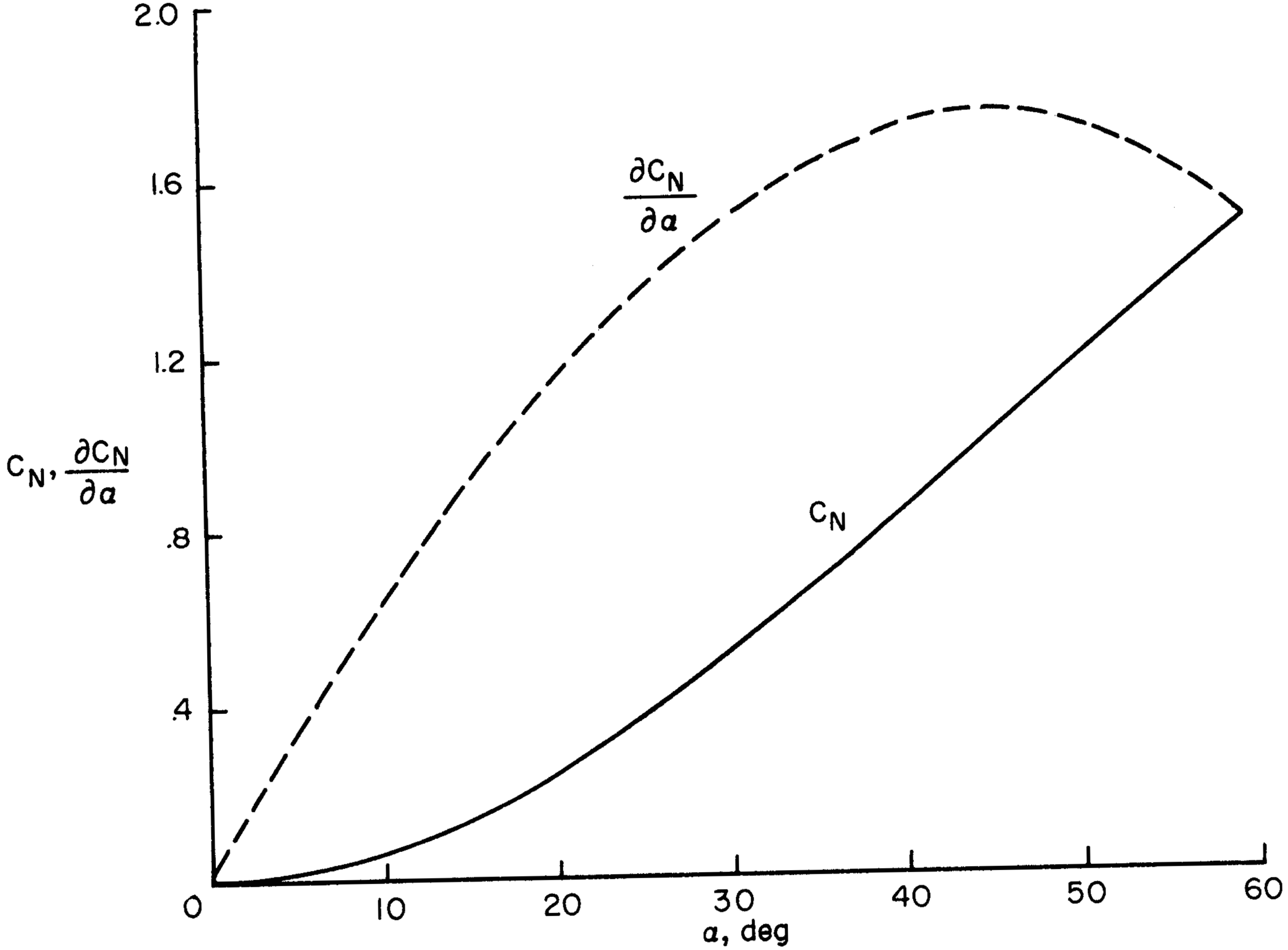

Figure 24.- Variation of C_N and $\partial C_N/\partial \alpha$ with α for a flat plate (simple Newtonian impact theory).

DECLA[redacted]IED

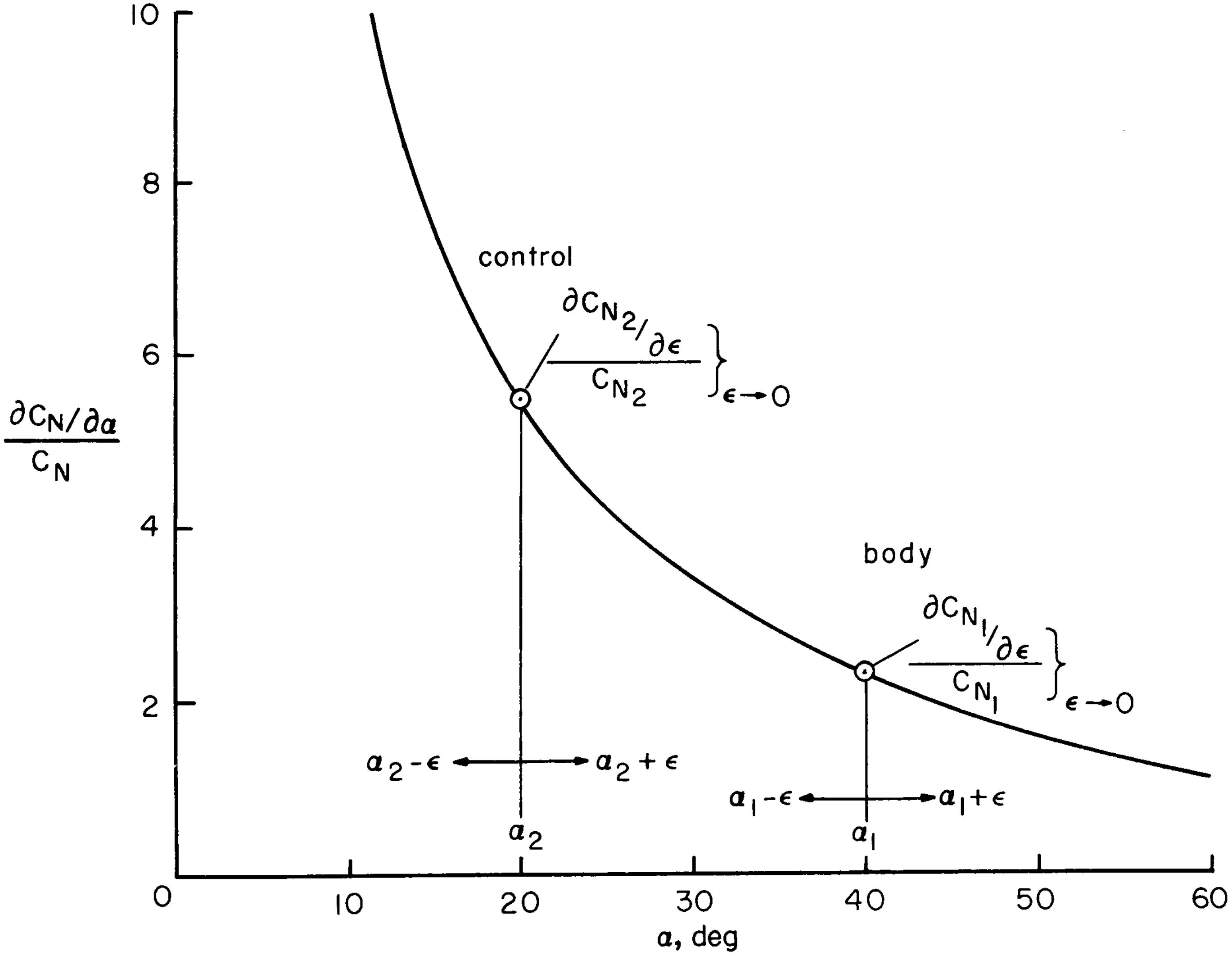

Figure 25.- Variation of $(\partial C_N/\partial \alpha)/C_N$ with α for a flat plate (simple Newtonian impact theory).

[redacted]

ERRATA

NASA TECHNICAL MEMORANDUM X-162

By John B. McDevitt and John V. Rakich
March 1960

Page 57, figure 10(b):

The ordinate scale should read 0, .05, .1, etc., instead of 0, .04, .08, etc.

Page 60, figure 10(e):

The ordinate scale should read 0, .5, 1.0, etc., instead of 0, .4, .8, etc.

THIS PAGE IS UNCLASSIFIED

NASA - Langley Field, Va.

Issued 6-1-60